N° d'ordre D. U : 2506
E D S P I C : 671

UNIVERSITE BLAISE PASCAL - CLERMONT II

ECOLE DOCTORALE
SCIENCES POUR L'INGENIEUR DE CLERMONT-FERRAND

T h è s e

Présentée par

Mahmoud Khodjet-Kesba

pour obtenir le grade de

DOCTEUR D'UNIVERSITÉ

SPECIALITE : ELECTROMAGNÉTISME

AUTOMATIC TARGET CLASSIFICATION BASED ON RADAR BACKSCATTERED ULTRA WIDEBAND SIGNALS

Soutenue publiquement le 06 Novembre 2014 devant le jury :

Mme Hélène Roussel	Président
M. Christian Brousseau	Rapporteur
M. Dong Ryeol Shin	Examinateur
M. Andrea Bianchi	Examinateur
M. Christophe Pasquier	Examinateur
Mme Claire Faure	Examinateur
M. Khalil El Khamlichi Drissi	Directeur de thèse
M. Sukhan Lee	Directeur de thèse

Blaise Pascal University

Doctoral School of Engineering Science

Sungkyunkwan University

Department of Electrical and Computer Engineering

College of Information and Communication Engineering

Doctoral Thesis

Speciality: Electromagnetism

Automatic Target Classification based on Radar Backscattered Ultra WideBand Signals

by

Mahmoud Khodjet-Kesba

Pr Khalil El Khamlichi Drissi, Supervisor
Pr Sukhan Lee, Supervisor
Pr Hélène Roussel, Rapporteur
Pr Christian Brousseau, Rapporteur
Pr Dong Ryeol Shin, Member
Pr Andrea Bianchi, Member
Dr Christophe Pasquier, Member
Dr Claire Faure, Member

November 06, 2014

Acknowledgements

The accomplishment of this thesis was made possible with the help and support of many people. First of all, I would like to thank my two advisors. Pr Khalil El Khamlichi Drissi of Blaise Pascal University, he always believed on me, helped and encouraged me through some rough periods. I admire his devotion and efficiency. Pr Sukhan Lee of Sungkyunkwan University, I thank him for his guidance, motivation and technical assistance with my research. He welcomed me and helped me to adapt in Korea, this beautiful country that I discovered and which has a special place in my heart.

I am also grateful to Claire Faure, Kamal Kerroum and Christophe pasquier for the advices, comments and stimulating discussion I received from them.

I am grateful to the rapporteurs of my defense committee: Professor Hélène Roussel of the Pierre and Marie Curie University (Paris 6) and Professor Christian Brousseau of the Rennes 1 University. I am also grateful to Professor Dong Ryeol Shin of the Sungkyunkwan University and Professor Andrea Bianchi of the Sungkyunkwan University for their highly appreciated participation in the defense committee.

I owe the utmost gratitude to my parents for their love and for their endless support in whatever I wanted to do. It is to them I dedicate this thesis.

Abstract

The objective of this thesis is the Automatic Target Classification (ATC) based on radar backscattered Ultra WideBand (UWB) signals. The classification of the targets is realized by making comparison between the deduced target properties and the different target features which are already recorded in a database. First, the study of scattering theory allows us to understand the physical meaning of the extracted features and describe them mathematically. Second, feature extraction methods are applied in order to extract signatures of the targets. A good choice of features is important to distinguish different targets. Different methods of feature extraction are compared including wavelet transform and high resolution techniques such as: Prony's method, Root-Multiple SIgnal Classification (Root-MUSIC), Estimation of Signal Parameters via Rotational Invariance Techniques (ESPRIT) and Matrix Pencil Method (MPM). Third, an efficient method of supervised classification is necessary to classify unknown targets by using the extracted features. Different methods of classification are compared: Mahalanobis Distance Classifier (MDC), Naïve Bayes (NB), k-Nearest Neighbors (k-NN) and Support Vector Machine (SVM). A useful classifier design technique should have a high rate of accuracy in the presence of noisy data coming from different aspect angles. The different algorithms are demonstrated using simulated backscattered data from canonical objects and complex target geometries modeled by perfectly conducting thin wires. A method of ATC based on the use of Matrix Pencil Method in Frequency Domain (MPMFD) for feature extraction and MDC for classification is proposed. Simulation results illustrate that features extracted with MPMFD present a plausible solution to automatic target classification. In addition, we prove that the proposed method has better ability to tolerate noise effects in radar target classification. Finally, the different algorithms are validated on experimental data and real targets.

Keywords: Backscattering, Ultra wideband radar, Feature extraction, Automatic Target Classification, Matrix Pencil Method.

Résumé

L'objectif de cette thèse est la classification automatique des cibles (ATC) en utilisant les signaux rétrodiffusés par un radar ultra large bande (UWB). La classification des cibles est réalisée en comparant les signatures des cibles et les signatures stockées dans une base de données. Premièrement, une étude sur la théorie de diffusion nous a permis de comprendre le sens physique des paramètres extraits et de les éxprimer mathématiquement. Deuxièmement, des méthodes d'extraction de paramètres sont appliquées afin de déterminer les signatures des cibles. Un bon choix des paramètres est important afin de distinguer les différentes cibles. Différentes méthodes d'extraction de paramètres sont comparées notamment : méthode de Prony, Racine-classification des signaux multiples (Root-MUSIC), l'estimation des paramètres des signaux par des techniques d'invariances rotationnels (ESPRIT), et la méthode Matrix Pencil (MPM). Troisièmement, une méthode efficace de classification supervisée est nécessaire afin de classer les cibles inconnues par l'utilisation de leurs signatures extraites. Différentes méthodes de classification sont comparées notamment : Classification par la distance de Mahalanobis (MDC), Naïve Bayes (NB), k-plus proches voisins (k-NN), Machines à Vecteurs de Support (SVM). Une bonne technique de classification doit avoir une bonne précision en présence de signaux bruités et quelques soit l'angle d'émission. Les différents algorithmes ont été validés en utilisant les simulations des données rétrodiffusées par des objets canoniques et des cibles de géométries complexes modélisées par des fils minces et parfaitement conducteurs. Une méthode de classification automatique de cibles basée sur l'utilisation de la méthode Matrix Pencil dans le domaine fréquentiel (MPMFD) pour l'extraction des paramètres et la classification par la distance de Mahalanobis est proposée. Les résultats de simulation montrent que les paramètres extraits par MPMFD présentent une solution plausible pour la classification automatique des cibles. En outre, nous avons prouvé que la méthode proposée a une bonne tolérance aux bruits lors de la classification des cibles. Enfin, les différents algorithmes sont validés sur des données expérimentales et cibles réelles.

Mots clés: Rétrodiffusion, Radar ultra large bande, Extraction de paramètres, Classification automatique de cibles, La méthode Matrix Pencil.

Contents

List of Figures **x**

List of Tables **xiii**

List of Abbreviations **xiv**

1 Introduction **1**

1.1 Overview 1

1.2 Contributions and thesis organization 4

1.3 List of publications 5

2 Electromagnetism and Scattering theory **8**

2.1 Introduction 8

2.2 Notions of electromagnetism 8

2.2.1 Maxwell's equations 8

2.2.2 Time harmonic fields 9

2.2.3 Propagation equations in unbounded media 10

2.3 Scattering theory 10

2.3.1 The radar cross section 11

2.3.2 Frequency regions 12

2.3.3 Propagation mechanisms 13

2.3.4 Singularity Expansion Method 15

2.3.5 Geometric Theory of Diffraction 17

2.3.6 Reduced complexity model 17
2.4 Field regions 19
2.4.1 Reactive near field region 19
2.4.2 Radiating near field (Fresnel) region 19
2.4.3 Far field (Fraunhofer) region 20
2.5 Theoretical analysis of the backscattered field from canonical objects 20
2.5.1 The conducting sphere 20
2.5.2 The thin wire 27
2.6 Conclusion 32
3 UWB Radar **33**
3.1 Introduction 33
3.2 Radars 33
3.2.1 Information available from a radar 34
3.2.2 The deficiencies of conventional radars 37
3.3 Historical review of UWB radar 38
3.4 Definition of UWB 40
3.5 Application of ultra-wideband sensing 43
3.6 Advantages of Ultra-Wideband Radar 46
3.7 UWB techniques 47
3.7.1 Impulse radar 47
3.7.2 Noise radar 50
3.7.3 Step frequency radar 51
3.7.4 Frequency modulated continuous wave radar 53
3.7.5 Conclusion 54
3.8 UWB radar in Automatic target classification 55

3.9 Conclusion . . . 57

4 Radar automatic target classification 59

4.1 Introduction . . . 59

4.2 Feature extraction . . . 59

4.2.1 Wavelet transform . . . 60

4.2.2 High resolution methods . . . 64

4.3 Classification methods . . . 78

4.3.1 Introduction . . . 78

4.3.2 Cross Validation . . . 78

4.3.3 The Mahalanobis Distance Classifier . . . 79

4.3.4 Naïve Bayes . . . 80

4.3.5 k-NN . . . 81

4.3.6 Support Vector Machine . . . 82

4.4 Conclusion . . . 88

5 Simulation and experimental results 89

5.1 Introduction . . . 89

5.2 Simulation results of backscattered fields from canonical objects . . . 89

5.2.1 Presentation of FEKO and the simulation parameters . . . 90

5.2.2 The signals in time domain . . . 90

5.2.3 The signals in Frequency domain . . . 92

5.3 Feature extraction results . . . 92

5.3.1 Comparison between analytical and measured CNRs . . . 92

5.3.2 Matrix Pencil Method in Time Domain . . . 98

5.3.3 Matrix Pencil Method in Frequency Domain . . . 102

5.4 Classification results . . . 104

5.5 Classification of complex objects in white Gaussian noise 108
5.5.1 Classifier Design 109
5.5.2 Simulation results 111
5.6 Experimental results 116
5.6.1 Measurement setup 116
5.6.2 Data processing and feature extractions 118
5.6.3 Classification results 121
5.7 Conclusion 125
6 Conclusions **127**
A Analytical expression of the sphere's residues **131**
Bibliography **135**

List of Figures

2.1 The RCS of a sphere as function of $k\ a$ (k is the wave number and a is the radius of the sphere) 13

2.2 Three field regions surrounding a scattering object 19

2.3 Normal plane wave incidence ($\theta = 90°$) on a conducting sphere 21

2.4 Magnitude of the backscattered field from a sphere (k is the wave number and a is the radius of the sphere) 23

2.5 Addition of specular and creeping waves 23

2.6 Complex Natural Resonances of a conducting sphere 26

2.7 Geometry of the thin wire 27

2.8 Plot of the backscattered field of a thin wire for $\theta_i = \theta_0 = 90°$ 29

2.9 Overlay plots of the normalized resonant frequencies as computed by the methods of Giri, et al., Tesche and Myers, et al., for the wire with $a/L = 0.005$ 31

3.1 The radar system diagram 34

3.2 Schematic of the calculation of the velocity 35

3.3 An air-surveillance radar 36

3.4 Target localization using three radars 36

3.5 A UWB signal is defined to have an absolute bandwidth $B \geq 500MHz$, or a fractional bandwidth greater than 0.2 42

3.6 Comparison of various radio system spectrums 42

3.7 The different UWB techniques 48

3.8 Impulse radar with sequential sampling 49

3.9 Block diagram of a noise radar 50
3.10 Step-frequency waveform 52
3.11 Block diagram of step-frequency radar 53
3.12 The principle of operation of an FMCW radar 54
3.13 Block diagram of an FMCW radar 54
3.14 Overview of the target recognition process 56
4.1 Wavelet decomposition scheme 63
4.2 Optimal separating hyperplane in a two-dimensional space 83
5.1 Example of the three canonical objects 91
5.2 Gaussian pulse time 91
5.3 The backscattered fields form the three canonical objects in the time domain 93
5.4 The backscattered fields from the three canonical objects in the frequency domain 94
5.5 The backscattered fields form thin wire (a/L = 0.005) 96
5.6 Normalized CNRs location in the s-plane with different incident angles 97
5.7 Normalized CNRs location in the s-plane with different values of SNR 98
5.8 Simulated signal compared with reconstructed signal by MPMTD . . 100
5.9 Variation of positive imaginary part of the poles with sliding time . . 101
5.10 Simulated signal compared with reconstructed signal by MPMFD . . 103
5.11 k-NN classification accuracy of wavelets 105
5.12 Classification accuracy of wavelets for MDC, k-NN, NB and SVM . . 107
5.13 The 4 target geometries 111
5.14 Simulated signal compared with reconstructed signal by MPMFD . . 114
5.15 The Mahalanobis distance of the object 1 with an aspect angle of 45° from the 4 targets 115

5.16 Comparison between the total classification accuracy when using only E_θ or both E_θ and E_φ 115

5.17 UWB P400 MRM 116

5.18 Radar system 116

5.19 Transmitted waveform 117

5.20 The indoor environment 118

5.21 Raw signal received by the radar 119

5.22 Signatures of the three targets after removing the environment 120

5.23 Normalized signatures of the three targets 122

5.24 Measured signal compared with reconstructed signal by MPMFD . . 123

5.25 The first three singular values for one angle 124

5.26 The first three singular values for all angles 124

List of Tables

2.1 Frequency dependence parameters for canonical scattering geometries 18

5.1 Features extracted by MPMTD from a thin wire (l = 3m), a sphere (r = 0.3 m), and a cylinder (l= 0.6 m, r= 0.2 m) (poles$\times$ 10^9) 99

5.2 Features extracted by MPMFD from a thin wire (l = 3m), a sphere (r = 0.3 m), and a cylinder (l= 0.6 m, r= 0.2 m) (poles$\times$ 10^8) 104

5.3 Classification accuracy of each object (%) 108

5.4 Dimensions of the four targets 112

5.5 Classification accuracy of each object (%) 113

5.6 Classification accuracy of each target (%) 125

List of Abbreviations

ADC	Analog to Digital Converter
ATC	Automatic Target Classification
CNRs	Complex natural resonances
coif	Coiflet
CWT	Continuous Wavelet Transform
DARPA	US Defense Advanced Research Projects Agency
db	Daubechies
DSP	Digital Signal Processor
DWT	Discrete Wavelet Transform
ESPRIT	Estimation of Signal Parameters via Rotational Invariance Techniques
FCC	Federal Communication Commission
FEKO	FEldberechnung bei Krpern mit beliebiger Oberflche (German: Field computations involving bodies of arbitrary shape)
FEM	Finite Element Method
FFT	Fast Fourier Transform
FMCW	Frequency Modulated Continuous Wave
FPGA	Field Programmable Gate Array
GPR	Ground Penetrating Radar
HDTV	High Definition Television
HPF	High-Pass Filter

IFFT	Inverse Fast Fourier Transform
k-NN	k-Nearest Neighbors
LPF	Low-Pass Filter
LS	Least-Squares
MDC	Mahalanobis Distance Classifier
MLFMM	Multilevel Fast Multipole Method
MoM	Method of Moments
MPM	Matrix Pencil Method
MRM	Monostatic Radar Module
NB	Naive Bayes
PANs	Personal Area Networks
PO	Physical Optics
PRI	Pulse Repetition Interval
RFID	Radio Frequency Identification
Root-MUSIC	Root-MUltiple SIgnal Classification
SEM	Singularity Expansion Method
SNR	Signal-to-Noise Ratio
SVM	Support Vector Machine
TLS	Total Least Squares
UMTS	Universal Mobile Telecommunications System
USB	Universal Serial Bus
UTD	Uniform Theory of Defraction
UWB	Ultra Wideband

1

Introduction

1.1 Overview

The work done in this thesis is in the framework of a co-degree program between Pascal Institute in Blaise Pascal University (France) and Intelligent Systems Research Institute in SungKyunKwan University (Republic of Korea) under the project entitled Cognitive Personal Transport Service Robot sponsored by the Gyeonggi-province International Collaboration Research Project. The project has the following research objectives to accomplish:

- To develop original technologies, as well as designing and demonstrating a prototype, for the Cognitive Personal Transport Service Robot capable of autonomous and/or semi-autonomous individual robotic and environmentally friendly call taxi service in towns, campuses, and tourist attractions where the driving environments such as roads, traffic signs, moving traffics, pedestrians, trees, animals, etc have to be recognized.

- To explore enabling technologies for extending the devloped Cognitive Personal Transport Service Robot into a public ride-share system. The key technolo-

gies to be developed include: Autonomous navigation, Sociable multi-modal human-vehicle interaction and Platforms for software, hardware and network for a cognitive personal transport robot based ride share system.

Autonomous navigation of vehicles is a complex problem that has attracted the attention of the research community and related companies. Systems capable of performing efficient and robust autonomous navigation are of interest in many robotic applications such as automatic industry, personal transportation, assistances to disabled or elder people, surveillance, etc. In order to perform navigation, the vehicle needs to interact with the environment, and for this purpose different types of sensors can be used for extracting the meaningful information and then making a decision for safe and unmanned navigation. From all of them, vision systems are the most used because they provide very rich information. However, the visual systems can become vulnerable when weather is severe and visibility is low (fogs, night, etc) or when target is well protected and hidden such as deeply beneath the foliage. In this case, using electromagnetic waves can be a good solution for target identification.

In the last fifteen years, the interest in Ultra Wideband (UWB) systems has grown rapidly. One of several applications of the UWB is radar automatic target classification in autonomous vehicles. UWB radar uses very short duration pulses resulting in very wideband in frequency domain. The UWB technique has the advantage to be used for localization, target identification, and communication between vehicles. In this thesis, we propose to use UWB radar in order to automatically classify an unknown target. In Automatic Target Classification (ATC), the two main steps are feature extraction and classification. The identification of the target is realized by making comparison between the deduced target properties and the different target features which are already recorded in a database.

A good choice of features is important to distinguish different targets. The best handling of the feature extraction consists of understanding the physical behavior of a radar system in its environment. Based on this understanding, features must then be mathematically described depending on the given requirements. When the target is illuminated by ultra-wideband signals, the scattered transient response in the time domain is composed from two successive parts [1]. First, an impulsive part, corresponding to the early time response, comes from the direct reflection of the incident wave on the object surface. Next, during the late time, the oscillating part arises from resonance phenomena of the target. In the case where targets are perfect conductors, resonances occur outside the object and correspond to surface creeping waves.

Currently, there exist several techniques based on the analysis of the late time impulse response in order to extract Complex natural resonances (CNRs) such as: the E-pulse approach [2], the Tufts and Kumaresan method [3] , and the high resolution methods like Matrix Pencil Method [4]. The late time part of the signal depends, at least theoretically, on the target geometry and its physical properties. Thus, it is independent of the aspect and polarization of the excitation source [5]. However, the automatic determination of the late time is not an easy task [6]. CNRs can be extracted in the frequency domain by using the Cauchy method. In [7], this method is applied to compute the natural poles of an object in the frequency domain; however, in real time applications, this method is inconvenient.

In this thesis, we propose an approach of feature extraction in frequency domain by using Matrix Pencil Method. The proposed method takes into account not only the magnitude of the signal in frequency domain but also its phase. Therefore, all the physical characteristics of the target are taken into account. The physical and geometrical characteristics of the considered object and the incident waveform impact clearly the signatures of the treated targets and contribute efficiently to the

classification of the objects. The separation between the early time and the late time is not necessary by applying the proposed method. Moreover, we propose a powerful method for UWB radar automatic target classification in white Gaussian noise and different aspect angles between the radar and the target. The proposed method is validated on complex objects by simulations and experiments.

1.2 Contributions and thesis organization

The remainder of this dissertation is organized as follows:

- **Chapter 2** presents the different models of scattering. In particular, it presents Singularity Expansion Method (SEM), Geometric Theory of Diffraction (GTD) and its reduced complexity model. The chapter concludes by giving the theoretical analysis of the backscattered fields from canonical objects.

- **Chapter 3** provides an overview of radars and the deficiencies of conventional radars. Next, it gives the history, definition, application and advantages of UWB radars. This chapter summarizes temporal and frequency techniques used to obtain a UWB spectrum. Finally, it gives an overview of the UWB radar in ATC.

- **Chapter 4** presents the methods used for feature extraction including wavelet transform and high resolution techniques. Next, it presents the methods used for classification which include Mahalanobis Distance Classifier (MDC), Naïve Bayes (NB), k-Nearest Neighbors (k-NN) and Support Vector Machine (SVM). This chapter explains the cross validation method which is applied in order to evaluate and compare the different methods of classification.

- **Chapter 5** gives the simulation and experiment results. The chapter proposes a powerful method for UWB radar automatic target classification in white

Gaussian noise and different aspect angles between the radar and the target.

- **Chapter 6** provides the conclusion. It summarizes the main achievements of this thesis and outlines future research directions.

The main contributions can be summarized as follows:

- Comparison of different methods of feature extraction in time domain and in frequency domain.
- Proposition of a feature extraction method, called Matrix Pencil Method in Frequency Domain (MPMFD), based on the extraction of parameters in frequency domain.
- Comparison of different methods of classification including: MDC, NB, k-NN and SVM.
- Proposition of a powerful method for UWB radar ATC in white Gaussian noise and different aspect angles between the radar and the target.

1.3 List of publications

This research work resulted in the following publications:

1. Journal papers:

- **M. Khodjet-Kesba**, K. El Khamlichi Drissi, S. Lee, K. Kerroum, C. Faure and C. Pasquier, Comparison of Matrix Pencil Extracted Features in Time Domain And in Frequency Domain for Radar Target Classification, *International Journal of Antennas and Propagation*, vol. 2014, Article ID 930581, 9 pages, 2014.

2. International conferences:

- **M. Khodjet-kesba**, K. Chahine, k. El khamlichi drissi, and K. Kerroum, Comparison of Ultra-wideband Radar Target Classification Methods Based on Complex Natural Resonances, *PIERS*, March 2012, Kuala Lumpur, Malaysia.

- **M. Khodjet-Kesba**, K. El Khamlichi Drissi, K. Kerroum, C. Faure and C. Pasquier, The choice by cross validation technique of features extraction method for UWB radar target classification, *PIERS*, august 2012, Moscow, Russia.

- **M. Khodjet-Kesba**, K. El Khamlichi Drissi, S. Lee, K. Kerroum, C. Faure and C. Pasquier, Robust UWB Radar Target Classification in White Gaussian Noise based on Matrix Pencil Method in Frequency Domain and Mahalanobis Distance, *International radar conference*, 2014, Lille, France.

- **M. Khodjet-Kesba**, K. El Khamlichi Drissi, S. Lee, K. Kerroum, C. Faure and C. Pasquier, Caractérisation Efficiente d'objets Diffractants Dans Le Domaine Fréquentiel, *CEM 2014*, Clermont Ferrand, France.

- S. Lalléchère, S. Girard, **M. Khodjet-Kesba**, I. El Baba, A. Catrain, K. Drissi, P. Bonnet, F. Paladian, Confrontation de mesures numériques et expérimentales pour la caractérisation de cibles en environnements libre et confiné, *CEM 2014*, Clermont Ferrand, France.

3. National conferences:

- **M. Khodjet-Kesba**, K. El Khamlichi Drissi, S. Lee, K. Kerroum, C. Faure and C. Pasquier, Nouvelles approches d'identification d'obstacles en utilisant un Radar UWB, 15eme Journée Scientifique de l'école doctorale Sciences Pour l'Ingénieur. Clermont-Ferrand, 2011.

2

Electromagnetism and Scattering theory

2.1 Introduction

In this chapter we present some notions in electromagnetism. Next, we present the scattering theory where we show the different models of scattering. In particular, Singularity Expansion Method (SEM) , Geometric Theory of Diffraction (GTD) and its reduced complexity model are presented. Then, we talk about the three field regions surrounding a scattering object. Finally, theoretical analysis of the backscattered fields from canonical objects is presented.

2.2 Notions of electromagnetism

2.2.1 Maxwell's equations

James Clark Maxwell (1831-1879) published a complete form of equations that govern the behavior of the electromagnetic phenomenon, it involves the behavior of two vector fields: the electric field $\vec{E}$, and the magnetic induction $\vec{B}$.

The basic Maxwell equations in derivative form are given in time domain as:

$$r\vec{o}t(\vec{E}) = -\frac{\partial \vec{B}}{\partial t} \tag{2.1}$$

$$div(\vec{B}) = 0 \tag{2.2}$$

$$r\vec{o}t(\vec{B}) = \mu(\vec{J} + \epsilon\frac{\partial\vec{E}}{\partial t}) \tag{2.3}$$

$$div(\vec{E}) = \frac{\rho}{\epsilon} \tag{2.4}$$

$\vec{J}$ is the electric current density and ρ is the electric charge density. ϵ is the electric permittivity, and μ is the magnetic permeability. The electric permittivity is related to its relative permittivity ϵ_r and the permittivity of the vacuum by the relation: $\epsilon = \epsilon_0\epsilon_r$. In the same way, the magnetic permeability is related to its relative permeability and the permeability of the vacuum by the relation: $\mu = \mu_0\mu_r$. Further discussion about the physical significance of each of these equations may be found in [8, 9].

The constitutive relations describe the interaction between the fields and the medium of propagation. For a linear, homogenous and isotropic medium these are of the form:

$$\vec{D} = \epsilon\vec{E} \tag{2.5}$$

$$\vec{B} = \mu\vec{H} \tag{2.6}$$

2.2.2 Time harmonic fields

We usually use the Maxwell's equations in their harmonic form, by considering that fields and sources have sinusoidal dependence on time. Then, we can write the electric field as:

$$\vec{E}(\vec{r}, t) = \vec{E}(\vec{r})e^{j\omega t} \tag{2.7}$$

and Maxwell's equations (2.1) and (2.3) become:

$$r\vec{o}t(\vec{E}) = -j\omega\vec{B} \tag{2.8}$$

$$r\vec{o}t(\vec{H}) = \vec{J} + j\omega\vec{D} \tag{2.9}$$

2.2.3 Propagation equations in unbounded media

We suppose that all sources are putted in the infinite, so they don't appear in the equations. In an unbounded, linear, homogenous and isotropic media, the Maxwell's equations allow to deduce the propagation equations in time domain of the electromagnetic fields $\vec{E}$ and $\vec{H}$:

$$\Delta\vec{E} - \frac{1}{\nu^2}\frac{\partial^2\vec{E}}{\partial t^2} = 0 \tag{2.10}$$

$$\Delta\vec{H} - \frac{1}{\nu^2}\frac{\partial^2\vec{H}}{\partial t^2} = 0 \tag{2.11}$$

where Δ is the Laplacian. The propagation speed of the wave in infinite media is:

$$\nu = \frac{1}{\sqrt{\epsilon\mu}} \tag{2.12}$$

We seek solutions of fields that vary in time under the sinusoidal form. The general form of the elementary solution is:

$$\vec{E_0}\ e^{j(\omega t - \vec{k}\vec{r})} \tag{2.13}$$

$\vec{E_0}$ is a constant vector, $\vec{k}$ is the wave vector. This solution represents a plane wave because all points of a wave plan perpendicular to the vector of propagation $\vec{k}$ have the same vibratory behavior.

The wave number k is defined as follows:

$$k = \frac{2\pi}{\lambda} \tag{2.14}$$

where λ is the wavelength.

2.3 Scattering theory

Scattering is defined as the redirection of radiation out of the original direction of propagation, usually due to interactions of the wave with the target. When the

scattering field is radiated in the backward direction to the incident wave, it is called backscattered field.

Different models have been proposed for scattering using either resonances or scattering centers. Baum [10], proposed a mathematical model in time domain called Singularity Expansion Method (SEM) which is based on Complex Natural Resonances (CNRs), where a portion of scattered fields in time domain, called late time, is expressed as series of damped exponentials. As an alternative to resonance-based processing, Geometric Theory of Diffraction (GTD) model is commonly used in frequency domain to describe the characteristics of the scattering centers [11]. GTD assumes that the target backscatter is issued from a series of discrete scattering centers.

In this section, we firstly introduce the notion of Radar Cross Section (RCS). Next, we present frequency regions. Then, the interactions between wave and target are analyzed by giving basic propagation mechanisms. Next, we present the SEM. After that, we talk about the GTD model. Finally, we present a reduced complexity model in frequency domain.

2.3.1 The radar cross section

Any object illuminated by an electromagnetic wave disperses incident energy in all directions. This spatial distribution of energy is called scattering, and the object itself is called a scatterer. The energy scattered back to the source of the wave is called backscattering and constitutes the radar echo of the object. The radar cross section is used to quantify the intensity of the echo.

The RCS of an object, σ, is defined as an equivalent area intercepting the amount of power that, when scattered isotropically, produces at the receiver a power density

that is equal to the power density scattered by the actual target. This is given by:

$$\sigma = \lim_{r \to \infty} \left[4\pi r^2 \frac{|E^s|^2}{|E^i|^2} \right] \tag{2.15}$$

where

- E^i is the electric field strength of the incident wave impinging on the target, $(V.m^{-1})$
- E^s is the electric field strength of the scattered wave at the radar, $(V.m^{-1})$
- r is the distance from the target to the radar.

As the name suggests, the RCS has dimensions of area: metre-squared (m^2).

2.3.2 Frequency regions

The radiation characteristics of a target depend strongly on the frequency of the incident wave. There are three frequency regions where the RCS of the target is very different. These regions are defined according to the ratio between the major dimension D of the target and the wavelength λ of the incident signal.

Rayleigh region $D << \lambda$

At these wavelengths, the phase variation of the incident wave is small along the target. Therefore, the current induced on the surface of the target has approximately a constant phase and amplitude, regardless of the shape of the target. In this region, the RCS varies as $\frac{1}{\lambda^4}$ and the target is called electrically small.

Mie region (Resonance region) $D \approx \lambda$

At these wavelengths, the phase variation of the current on the body of the target is significant. All parts of the target contribute to the scattering pattern. The RCS oscillates as a function of the wavelength λ. This region is called resonance region.

Optical region $D >> \lambda$

In this frequency region, the RCS can be independent of λ and the target is called electrically large.

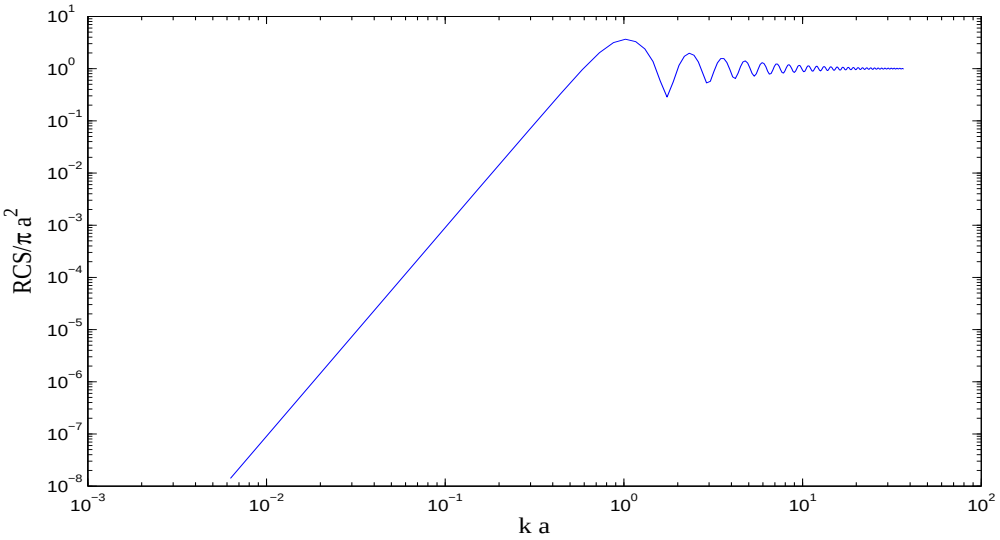

FIGURE 2.1: The RCS of a sphere as function of $k\ a$ (k is the wave number and a is the radius of the sphere)

The RCS of a sphere illustrates these three frequency regions (Figure 2.1). For $k\ a < 0.5$, where a is the radius of the sphere and k the wave number, the curve is nearly linear, it is the Rayleigh region. For $k\ a > 0.5$, it begins to oscillate, this is the resonance region. The oscillation is progressively damped for larger values of $k\ a$. For $k\ a \geq 10$, the curve is constant and equal to πa^2, it is the optical region.

2.3.3 Propagation mechanisms

Many targets have complex geometries and must be modeled as a set of discrete scattering points and mechanisms. There are seven basic scattering mechanisms [12]. All depend in varying degree on the target aspect angle as seen from the observation point. Some of these seven mechanisms are dominant whereas others are weak.

Reentrant structures

Reentrant Structures can be the cavities in a target, such as intake ducts, exhaust ducts, and cockpits on airplanes. Metallic cavities produce strong scattering fields, because any wave that enters into the cavities, will have internal reflections and will go out.

Specular scatterers

Specular reflections result from surfaces that are perpendicular to the incident wave's line-of-sight. The generated fields are significant when the angle-of-incidence is normal but fall off quickly as the angle varies from 90°.

Traveling wave fields

A surface travelling wave can be induced when the angle of incidence is small (the line-of-sight is nearly parallel to the target). The surface wave will travel along the surface of the target and can be reflected back toward the front by any discontinuity at the rear. Travelling wave fields can be nearly as large as specular fields.

Diffraction

Tips, edges, and corners diffract the incident wave but the fields are less significant than specular reflections. In the case where the other sources of fields don't exist, the intensity of the diffracted fields can be significant.

Surface discontinuities

Discontinuities such as gaps and rivets can reflect energy. The isolation and characterization of the effects of surface discontinuities is not easy because these effects tend to be small.

Creeping waves

Creeping waves are generated by surface waves that follow the curvature of the target and are launched back toward the observation point. The intensity of the creeping waves is very small in comparison to the specular fields.

Interaction waves

Interaction waves result when the incident signal is reflected back toward the observation point after bouncing off two or more target surfaces. The generated fields are relatively strong.

2.3.4 Singularity Expansion Method

When a target is illuminated by wideband signals, the scattered transient response in the time domain is composed from two successive parts. First, an impulsive part, corresponding to the early time response, comes from the direct reflection of the incident wave on the object surface. Next, during the late time, the oscillating part arises from resonance phenomena of the target. The resonances can be separated into internal and external modes [13]. The internal resonances are caused by the internal waves that experience multiple internal reflections, whereas the external resonances are caused by the surface creeping waves. In the case where targets are perfect conductors, resonances occur outside the object and correspond only to external modes.

The singularity expansion method introduced by Baum has been applied to express electromagnetic response in an expansion of complex resonances of the system. In general, the signal model of the observed late time of an electromagnetic scattered response from an object can be written as:

$$y(t) = x(t) + n(t) \approx \sum_{m=1}^{M} R_m e^{S_m t} + n(t) \qquad 0 \leq t \leq T, \tag{2.16}$$

where:

- $y(t)$: denotes the time domain response,
- $n(t)$: denotes the noise in the system,
- $x(t)$: denotes the noiseless signal,
- R_m: are residues or complex amplitudes,
- $S_m = \alpha_m + j\omega_m$,
- α_m: are damping factors,
- ω_m: are angular frequencies ($\omega_m = 2\pi f_m$ with f_m the natural frequency),
- M is the total number of modes of the series.

After sampling, the time variable, t is replaced by kT_s, where T_s is the sampling period. The original continuous time sequence can be rewritten as:

$$y(kT_s) = x(kT_s) + n(kT_s) \approx \sum_{m=1}^{M} R_m z_k^m + n(kT_s) \quad for\ k = 0, \ldots, N-1 \tag{2.17}$$

$$z_m = e^{(\alpha_m + j\omega_m)T_s} \qquad for\ m = 1, 2, \ldots, M \tag{2.18}$$

We apply the Laplace transform of $x(t)$ to obtain the transfer function $H(s)$:

$$H(s) \approx \sum_{m=1}^{M} \frac{R_m}{s - S_m} \tag{2.19}$$

where $s = \sigma + j\omega$ is the complex variable in the Laplace plane.

2.3.5 Geometric Theory of Diffraction

The GTD was introduced by Keller [11] as an extension to geometrical optics to include edge, vertex diffracted rays and perfectly conducting wedge. The GTD predicts that at high frequency, the backscattered field appears to originate from a set of discrete scattering centers and follows a $(j\frac{f}{f_c})^{\alpha}$ frequency dependence where α depends upon the target geometry. The backscattered field can be approximated by:

$$E(f) = \sum_{m=1}^{M} A_m (j\frac{f}{f_c})^{\alpha_m} \; e^{j2\pi f t_m} \tag{2.20}$$

where:

- M is the number of scattering-centres,
- A_m is a complex amplitude associated with the reflectivity of the mth scattering-centre,
- f is the frequency,
- f_c is the reference frequency, it is used for normalization,
- t_m is the time delay between the observer and the mth scattering-centre,
- α_m is the frequency dependence parameter of the mth scattering-centre.

For simple targets, the frequency dependence of canonical scattering geometries is given in table 2.1 [14]. The scattering center analysis task is to determine the model parameters $\{A_m, t_m, \alpha_m\}_{m=1}^{M}$ that characterize the M individual scattering centers.

2.3.6 Reduced complexity model

In order to estimate the parameters of the scatterers from a set of radar data, the scattering model chosen must be suitable for being used by rather simple mathematical techniques. For this reason, a reduced complexity model has been proposed.

Table 2.1: Frequency dependence parameters for canonical scattering geometries

Value of α	Scattering geometries
-1	corner diffraction
$-\frac{1}{2}$	edge diffraction
0	point scatterer; doubly curved surface reflection; straight edge specular
$\frac{1}{2}$	singly curved surface reflection
1	flat plate at broadside; dihedral

In frequency domain, the scattered fields $E_\nu(\omega, r)$ can be expressed as [15]:

$$E_\nu(\omega, r) = \sum_{m=1}^{\infty} A_{\nu m}(\omega, r) exp(j\omega t_m) \tag{2.21}$$

where ν is any scattering field component of an orthogonal coordinate system (polarization), ω is the angular frequency, $A_{\nu m}(\omega, r)$ is the complex and frequency-dependent amplitude of the mth scattering center depending on the scattering mechanism, r is the far-field position and t_m is the time delay between the observer and the mth scattering center. The time dependence $exp(j\omega t)$ and the ν are dropped for convenience throughout. The following approximation is used [16]:

$$A_m(\omega, r) \approx a_m(r) e^{\gamma_m \omega} \tag{2.22}$$

where $a_m(r)$ is the amplitude, and γ_n is the phase which provides an approximate match between $A_m(\omega, r)$ and the exponential model. The approximation (2.22) can only be met over a relatively narrow bandwidth. After using (2.22) into (2.21) and the sampling procedure, the frequency response $Y(k\omega_s)$, which is the ratio between the received and emitted fields, will be expressed as:

$$\begin{aligned} Y(k\omega_s) &\approx \sum_{m=1}^{M} \hat{a}_m(r) e^{(\gamma_m k\omega_s + jk\omega_s t_m)} + n(k\omega_s) \\ &\approx \sum_{m=1}^{M} \hat{a}_m(r) x_m + n(k\omega_s) \\ k &= 0, \ldots, N-1 \end{aligned} \tag{2.23}$$

where ω_s is the angular frequency sampling, N is the number of frequency samples, M is the number of measurable wavefronts, $\hat{a}_m(r)$ is the complex amplitude, $n(k\omega_s)$ is the additive noise, and:

$$x_m = e^{(\gamma_m k\omega_s + jk\omega_s t_m)} \tag{2.24}$$

2.4 Field regions

There are three regions surrounding an antenna or a scattering object as shown in figure 2.2, the field structure is different in each region. There are various criteria to identify these regions.

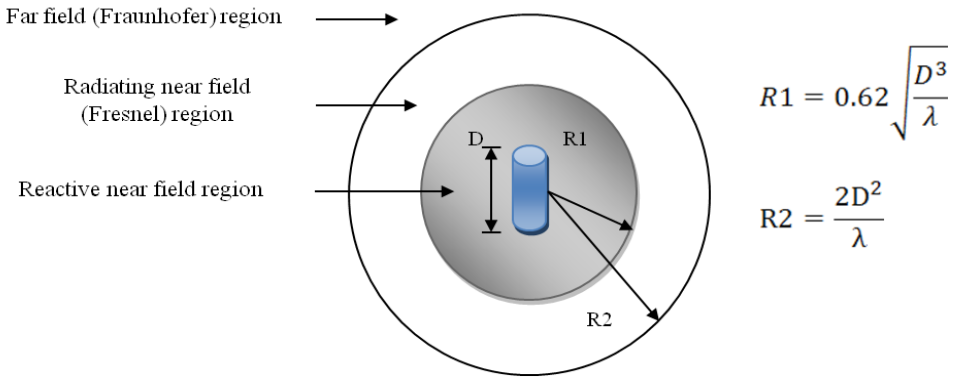

FIGURE 2.2: Three field regions surrounding a scattering object

2.4.1 Reactive near field region

This region surrounds immediately the scattering object. The outer boundary of this region is commonly taken to exist at a distance $R < 0.62\sqrt{\frac{D^3}{\lambda}}$ from the object surface, where λ is the wavelength and D is the largest dimension of the object.

2.4.2 Radiating near field (Fresnel) region

This region is between the reactive near field region and the far field region wherein radiation fields predominate and wherein the angular field distribution is dependent

upon the distance from the object. If the dimension of the object is not large compared to the wavelength, this region may not exist. The inner boundary is taken to be the distance $R \geq 0.62\sqrt{\frac{D^3}{\lambda}}$ and the outer boundary the distance $R < \frac{2D^2}{\lambda}$.

2.4.3 Far field (Fraunhofer) region

In this region, the angular field distribution is essentially independent of the distance from the object. The far field region is commonly taken to exist at distances greater than $\frac{2D^2}{\lambda}$ from the object (D must be large compared to the wavelength).

2.5 Theoretical analysis of the backscattered field from canonical objects

2.5.1 The conducting sphere

Because of its symmetry, the perfectly conducting sphere is the simplest of all three dimensional scatterers, it is often used as a reference scatterer to measure the scattering properties (such as the RCS) of other targets. Let us assume that the electric field of a plane wave is polarized in the x direction and it is traveling along the z axis as shown in figure 2.3.

The electric field of the incident wave can then be expressed as:

$$E^i = E_0 e^{jkz} e_x = E_0 e^{jkrcos\theta} e_x \tag{2.25}$$

where E_0 is the amplitude of the plane wave E^i, k is the wave number, and e_x is the unit vector in the direction of the coordinate axe x.

The component of the equation (2.25) can be transformed in spherical components to:

$$E^i = E^i_r e_r + E^i_\theta e_\theta + E^i_\phi e_\phi \tag{2.26}$$

where:

$$E^i_r = E^i_x \; sin\theta \; cos\phi = E_0 \; sin\theta \; cos\phi \; e^{jkrcos\theta} \tag{2.27}$$

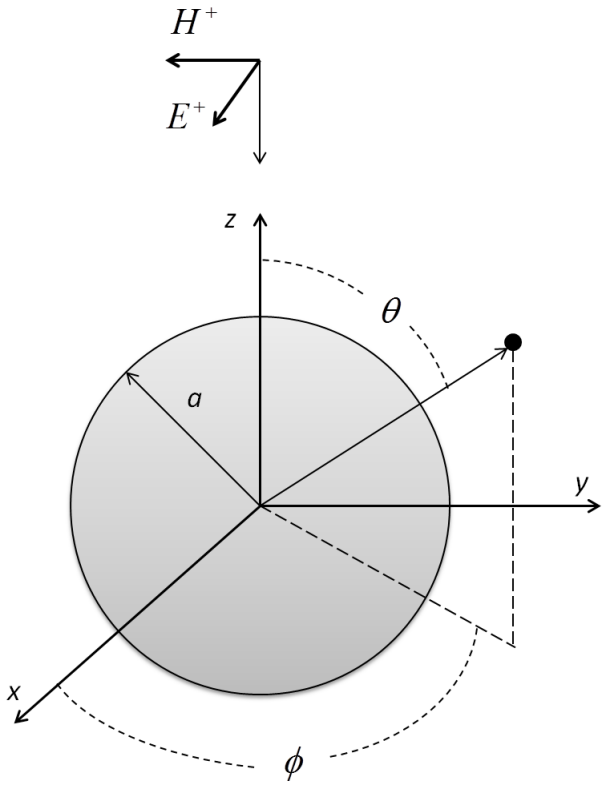

FIGURE 2.3: Normal plane wave incidence ($\theta = 90°$) on a conducting sphere

$$E_\theta^i = E_x^i \; cos\theta \; cos\phi = E_0 \; cos\theta \; cos\phi \; e^{jkrcos\theta} \tag{2.28}$$

$$E_\phi^i = -E_x^i \; sin\phi = -E_0 \; sin\phi \; e^{jkrcos\theta} \tag{2.29}$$

Scattering by a conducting sphere

The exact solution for the scattering by a conducting sphere is known as the Mie series [17].

In far field observations, the backscattered field from a sphere is [18]:

$$E_\theta^s = E_0 \frac{e^{-jkr}}{2kr} \sum_{n=1}^{\infty} \frac{(-1)^n (2n+1)}{\hat{H}_n^{(2)'}(ka)\hat{H}_n^{(2)}(ka)} \tag{2.30}$$

- a: radius of the sphere,

- r: distance from the sphere to the point of observation, and:

$$\hat{H}_n^{(2)}(x) = xh_n^{(2)}(x) = \sqrt{\frac{\pi x}{2}} H_{n+\frac{1}{2}}^{(2)}(x) \tag{2.31}$$

where:

- $h_n^{(2)}(x)$: are spherical Hankel functions of second order,
- $H_n^{(2)}(x)$: are regular cylindrical Hankel functions of second order.

Finally, we can write:

$$\begin{aligned} H_n^{(2)'}(x) &= \frac{1}{2}\sqrt{\frac{\pi}{2x}} H_{n+\frac{1}{2}}^{(2)}(x) + \sqrt{\frac{\pi x}{2}} H_{n+\frac{1}{2}}^{(2)'}(x) \\ &= \frac{1}{2}\sqrt{\frac{\pi}{2x}} H_{n+\frac{1}{2}}^{(2)}(x) + \frac{1}{2}\sqrt{\frac{\pi x}{2}} \left[H_{n-\frac{1}{2}}^{(2)}(x) - H_{n+\frac{3}{2}}^{(2)}(x) \right] \end{aligned} \tag{2.32}$$

The figure 2.4, shows the magnitude of $\frac{E_\theta^s}{E_0}$ without $\frac{e^{-jkr}}{r}$ as a function of the electrical size of the sphere: ka. The amplitude rises quickly from a value of zero to a peak near $ka = 1$ and then executes a series of decaying undulations as the sphere becomes electrically larger. The undulations are due to the fact that there is a region where specular reflected waves combine with backscattered creeping waves both constructively and destructively as shown in figure 2.5. The undulations become weaker with increasing ka because the creeping wave loses more energy the longer the electrical path traveled around the shadowed side.

The monostatic RCS of the sphere can be expressed using (2.30) by:

$$\sigma = \lim_{r\to\infty} \left[4\pi r^2 \frac{|E^s|^2}{|E^i|^2} \right] = \frac{\pi}{k^2} \left| \sum_{n=1}^{\infty} \frac{(-1)^n (2n+1)}{\hat{H}_n^{(2)'}(ka) \hat{H}_n^{(2)}(ka)} \right|^2 \tag{2.33}$$

where E^i is the incident field.

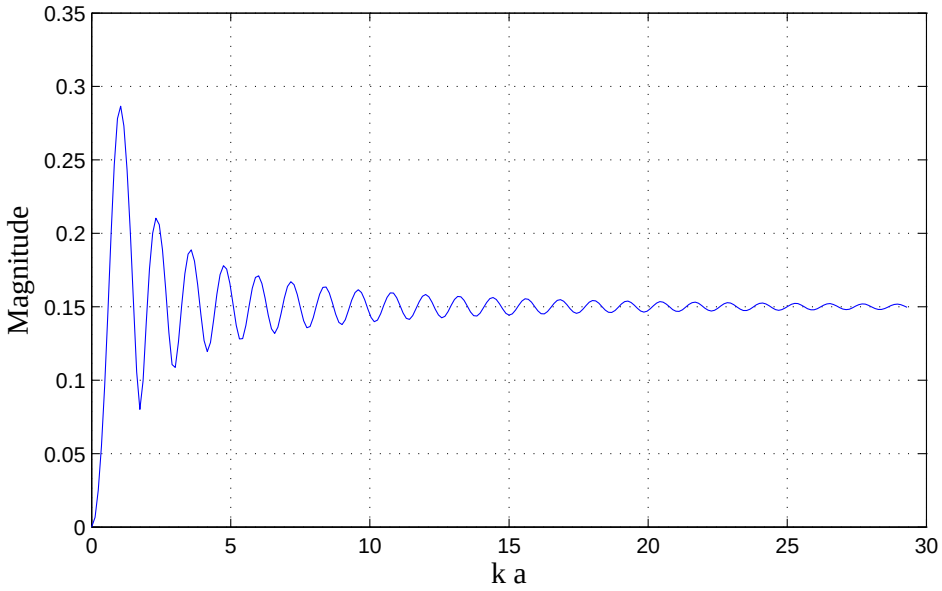

FIGURE 2.4: Magnitude of the backscattered field from a sphere (k is the wave number and a is the radius of the sphere)

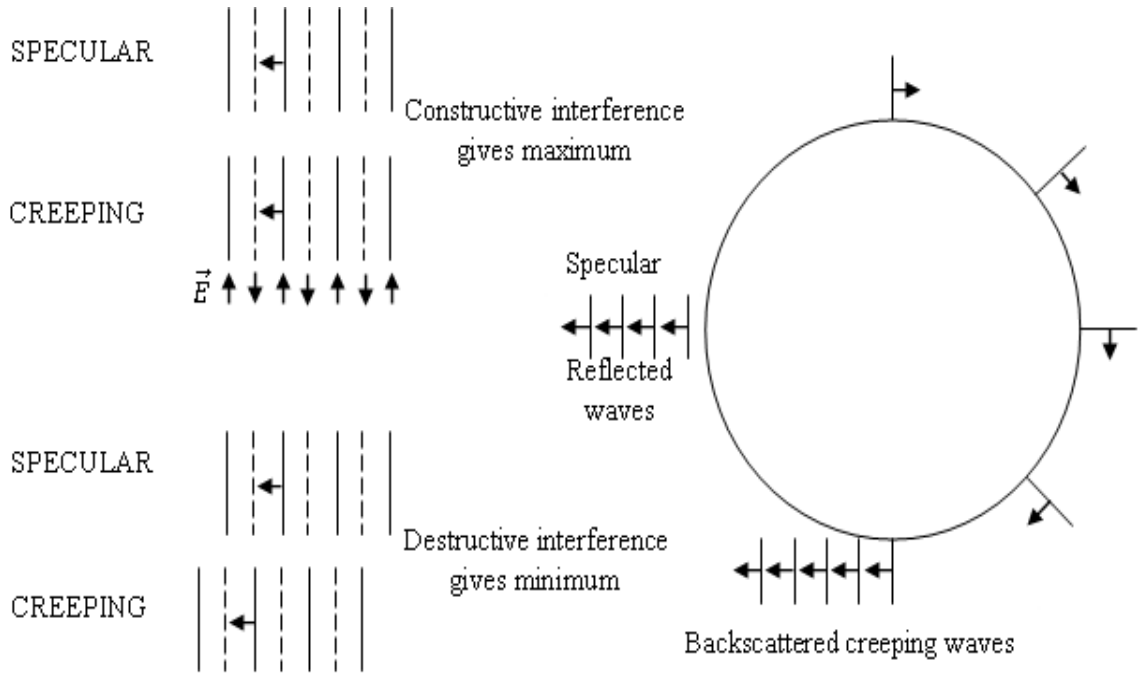

FIGURE 2.5: Addition of specular and creeping waves

For very small values of the electrical size ka, the first term of (2.33) ($n = 1$) is sufficient to accurately represent the RCS. Doing this we can approximate (2.33) by:

$$\sigma \approx \frac{\pi}{k^2}\left|\frac{3}{\hat{H}_1^{(2)'}(ka)\hat{H}_1^{(2)}(ka)}\right|^2 \tag{2.34}$$

Since:

$$\hat{H}_1^{(2)}(ka) \approx j\frac{1}{ka} \tag{2.35}$$

$$\hat{H}_1^{(2)'}(ka) \approx -j\frac{1}{(ka)^2} \tag{2.36}$$

(2.33) reduces to:

$$\sigma \approx \frac{9\pi}{k^2}(ka)^6 \tag{2.37}$$

which is representative of the Rayleigh region scattering.

For very large values of the electrical size ka, we can approximate the spherical Hankel function and its derivative in (2.33) by:

$$\hat{H}_n^{(2)}(ka) \approx \frac{e^{-j\left[ka(sin(\alpha)-\alpha\ cos(\alpha))-\frac{\pi}{4}\right]}}{\sqrt{sin(\alpha)}} \tag{2.38}$$

$$\hat{H}_n^{(2)'}(ka) \approx \sqrt{sin(\alpha)}e^{-j\left[ka(sin(\alpha)-\alpha\ cos(\alpha))+\frac{\pi}{4}\right]} \tag{2.39}$$

$$cos(\alpha) = \frac{n+\frac{1}{2}}{ka} \tag{2.40}$$

Thus (2.33) reduces for very large values of the radius a to:

$$\sigma = \frac{\pi}{k^2}\left|\sum_{n=1}^{\infty}\frac{(-1)^n(2n+1)}{\hat{H}_n^{(2)'}(ka)\hat{H}_n^{(2)}(ka)}\right|^2 \approx \pi a^2 \tag{2.41}$$

which is representative of the optical region scattering.

The CNRs of the sphere can be extracted theoretically by determining the poles of the equation (2.30). To find the poles, we should develop the Hankel functions in sum of series [19].

We develop the Hankel functions in sum of series in order to find the analytical expressions of the poles and residues. By putting: $z = ka$, we can write [20]:

$$\begin{aligned}\hat{H}_n^{(2)}(z) = zh_n^{(2)}(z) &= j^{n+1}e^{-jz}\sum_{\beta=0}^{n}\left(n+\frac{1}{2},\beta\right)(2jz)^{-\beta} \\ &= j^{n+1}e^{-jz}\sum_{\beta=0}^{n}\frac{(n+\beta)!}{\beta!\Gamma(n-\beta+1)}(2jz)^{-\beta} \\ &= j^{n+1}e^{-jz}\sum_{\beta=0}^{n}\frac{(n+\beta)!}{\beta!(n-\beta)!}(2jz)^{-\beta}\end{aligned} \tag{2.42}$$

We put $\zeta = jz$, hence:

$$\begin{aligned}\hat{H}_n^{(2)}(\zeta) &= j^{n+1}e^{-\zeta}\sum_{\beta=0}^{n}\frac{(n+\beta)!}{\beta!(n-\beta)!}(2\zeta)^{-\beta} \\ &= j^{n+1}e^{-\zeta}\left(\frac{f_n(\zeta)}{\zeta^n}\right)\end{aligned} \tag{2.43}$$

where:

$$f_n(\zeta) = \sum_{\beta=0}^{n}\frac{(n+\beta)!}{\beta!(n-\beta)!}\frac{1}{2^\beta}\zeta^{n-\beta} \tag{2.44}$$

And:

$$\begin{aligned}\hat{H}_n^{(2)'}(\zeta) &= -j^{n+2}e^{-\zeta}\sum_{\beta=0}^{n}\frac{(n+\beta)!}{\beta!(n-\beta)!}(2\zeta)^{-\beta} + j^{n+2}e^{-\zeta}\sum_{\beta=0}^{n}\frac{(n+\beta)!}{\beta!(n-\beta)!}\frac{1}{2^\beta}(-\beta)\zeta^{-\beta-1} \\ &= -j^{n+2}e^{-\zeta}\sum_{\beta=0}^{n}\frac{(n+\beta)!}{\beta!(n-\beta)!}\frac{1}{2^\beta}(1+\frac{\beta}{\zeta})\zeta^{-\beta} = j^n\frac{e^{-\zeta}}{\zeta}\frac{g_n(\zeta)}{\zeta^n}\end{aligned} \tag{2.45}$$

where:

$$g_n(\zeta) = \sum_{\beta=0}^{n} \frac{(n+\beta)!}{\beta!(n-\beta)!} \frac{1}{2^\beta} (\beta + \zeta)\zeta^{n-\beta} \tag{2.46}$$

The roots ζ_i of $f_n(\zeta)$ and $g_n(\zeta)$ are the poles of the backscattered field from a sphere. There are n roots for each $f_n(\zeta)$ function and $n+1$ roots for each $g_n(\zeta)$ function.

Figure 2.6 shows a doubly infinite set of natural resonance frequencies for $n = 43$ which correspond to the zeros of the hankel function of second order and its derivative. The zeros of $f_n(\zeta)$ are represented by red circles, and the zeros of $g_n(\zeta)$ are represented by blue circles.

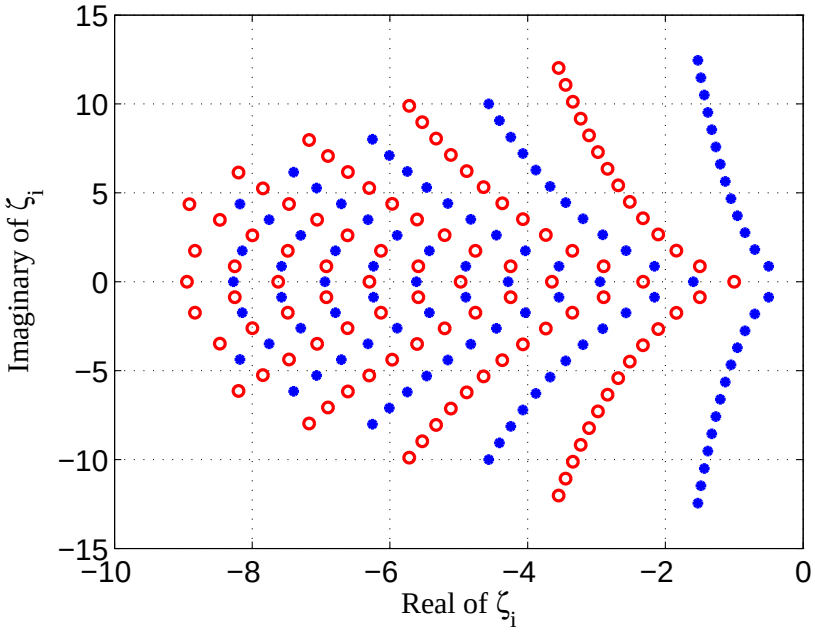

FIGURE 2.6: Complex Natural Resonances of a conducting sphere

In the appendix A, we show how to obtain the analytical expression of residues that are related to the poles.

2.5.2 The thin wire

The scattering field by a thin wire can be analytically determined by a variety of methods which allow computing the complex natural frequencies [21].

Scattering by a thin wire

The scattering geometry under consideration is shown in figure 2.7. The conducting thin wire has radius a and length L, and it is located in free space. The scattered field is produced by the incident field at angle θ_i and can occur at an arbitrary observation angle θ_0.

An approximation of the scattered field is given by [22]:

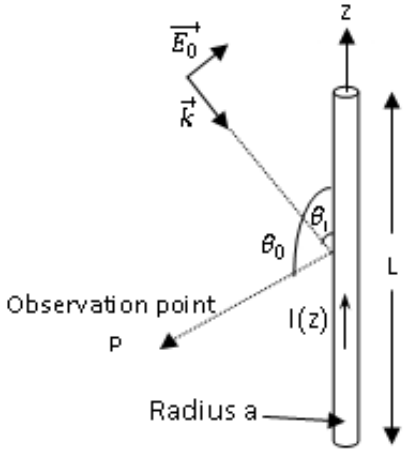

FIGURE 2.7: Geometry of the thin wire

$$r_0 E_\theta^{sca} = -\frac{E_0}{\Omega_0}\frac{sin\theta_0}{sin\theta_i}\frac{1}{sinkL}\int_0^L [(coskz - e^{jkzcos\theta_i})sinkL - (coskL - e^{jkLcos\theta_i})sinkz]e^{jkzcos\theta_0}dz \tag{2.47}$$

where k is the wave number, r_0 is the distance from the thin wire to the observation point, and $\Omega_0 = 2ln(L/a)$ is a factor used to describe the wire thikness.

We evaluate the integral analytically, we put:

$$\int_0^L f(z)dz = \frac{1}{sinkL}\int_0^L [(coskz - e^{jkzcos\theta_i})sinkL - (coskL - e^{jkLcos\theta_i})sinkz]e^{jkzcos\theta_0}dz \tag{2.48}$$

Then:

$$\int_0^L f(z)dz = \int_0^L \left[\frac{sink(L-z) + e^{jkLcos\theta_i}sinkz}{sinkL}e^{jkzcos\theta_0} - e^{jkz(cos\theta_0+cos\theta_i)}\right]dz \tag{2.49}$$

By putting $m = jkL$, and doing some transformations we obtain:

$$\int_0^L f(z)dz = \int_0^L \frac{sh(m(1-\frac{z}{L}))e^{m\frac{z}{L}}cos\theta_0}{sh(m)}dz + \int_L^0 \frac{e^{mcos\theta_i}sh(m\frac{z}{L})e^{m\frac{z}{L}}cos\theta_0}{sh(m)}dz - \int_0^L e^{m\frac{z}{L}(cos\theta_0+cos\theta_i)}dz \tag{2.50}$$

After evaluating the three integrals we find:

$$\begin{aligned}\int_0^L f(z)dz &= \frac{L}{m}\left[\frac{(\frac{ch(m)}{sh(m)} + cos\theta_0)}{sin^2(\theta_0)} - \frac{e^{mcos\theta_0}}{sh(m)sin^2(\theta_0)}\right] \\ &+ \frac{L}{m}\left[(\frac{ch(m)}{sh(m)} - cos\theta_0)\frac{e^{m(cos\theta_0+cos\theta_i)}}{sin^2(\theta_0)} - \frac{e^{mcos\theta_i}}{sh(m)sin^2(\theta_0)}\right] \\ &+ \frac{L}{m}\left[\frac{1}{cos\theta_0+cos\theta_i} - \frac{e^{m(cos\theta_0+cos\theta_i)}}{cos\theta_0+cos\theta_i}\right]\end{aligned} \tag{2.51}$$

$$\begin{aligned}\Longrightarrow \int_0^L f(z)dz &= \frac{L}{m}(1 - e^{m(cos\theta_0+cos\theta_i)})(\frac{1}{cos\theta_0+cos\theta_i} + \frac{cos_{\theta_0}}{sin^2(\theta_0)}) \\ &+ \frac{L}{m\ sh(m)sin^2(\theta_0)}(-e^{mcos\theta_0} - e^{mcos\theta_i} \\ &+ ch(m) + ch(m)e^{m(cos\theta_0+cos\theta_i)})\end{aligned} \tag{2.52}$$

Figure 2.8, shows an example of the backscattered field calculated using this approximate method, and a comparison with the more accurate numerical results using

the moment method. Consider the case of a thin wire scatterer with a length/radius ratio $L/a = 400$. For this calculation the incident field is normal ($\theta_i = 90°$), and the backscattered field is calculated ($\theta_0 = 90°$). In this figure, $log(|r_0 E|)$ is plotted for both methods. As can be noted, the agreement between the two solutions is not too bad away from the resonant frequencies of the wire. Near these frequencies, however, the lack of radiation resistance in the approximate model cause rather large errors. Nevertheless, the general trends in the data remain consistent for a wide range of frequencies.

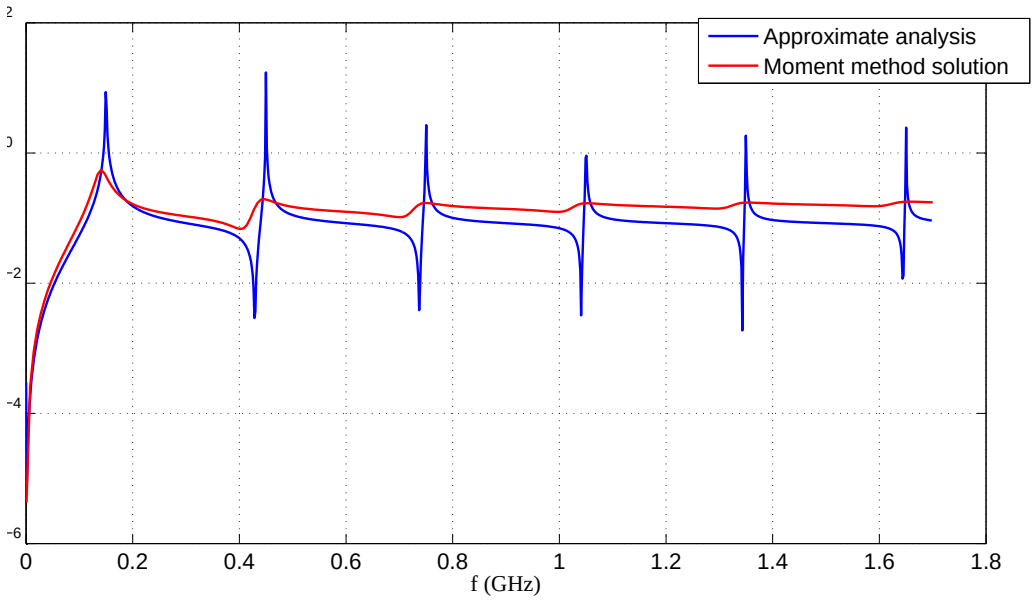

FIGURE 2.8: Plot of the backscattered field of a thin wire for $\theta_i = \theta_0 = 90°$

Methods for Determining the Wire Resonant Frequencies

The natural resonances of the wire can be determined by two methods: using the approximate solutions or using the integral equation solutions.

Approximate solutions Due to the relative difficulty in obtaining the resonances of the wire, several different approximations have been developed in the literature.

Lee and Leung [23] and Weinstein [24] use a Weiner-Hopf method, while Hoorfar and Chang [24] an infinite wire solution for the current, with additional reflected traveling current waves at the ends of the wire. Bouwkamp [25] and Marin and Liu [26] both use the asymptotic antenna theory of Hallen to obtain the resonances.

The equation below shows the expression given by Lee and Leung for the complex natural resonance frequencies in [23]:

$$s_n = \sigma_n + j\omega_n = \frac{jn\pi c}{L}\left[1 + \frac{1 - j\frac{2}{\pi}ln(2n\pi)}{4n\ ln(\frac{1.781\ an\pi}{L})}\right] \quad n = 1, 2, 3, \cdots \tag{2.53}$$

The accuracy of all these approximate methods deteriorates as the wire becomes thicker.

Solutions Based on the Integral Equation Solution The Pocklington equation describes the current flowing on the wire for a scattering problem. This current may be determined numerically by using the method of moments, as described by Harrington [27]. This procedure results in a system impedance matrix equation that contains information about all of the resonances of the wire. By generalizing this integral equation solution to complex frequencies, the natural frequencies are determined by searching for the zeros of the determinant of the system matrix. Tesche in [28] describes the initial calculation of the natural resonances of the wire structure through the use of Newton's method in the complex s-plane. This amounted to an iterative search for the zeros of the system determinant in the s-plane. As an alternative to the Newton search method for finding the wire resonances from the integral equation solution, a contour integration method proposed by Baum [29] can be used. Giri and his co-authors in [30] used this contour integration method to determine the frequencies in the s-plane.

The most recent contribution to the set of complex resonant frequencies based on an integral equation for the wire is described in [31]. This analysis method results

in a characteristic equation involving a complex propagation constant k, from which the roots may be determined iteratively. The equation is shown below:

$$F(k) = (k_n^2 - k^2)\{2L\left[ln\frac{2L}{a} - \int_0^L \frac{dy}{y}(1 - e^{jky}cos(k_n y))\right] + \frac{i}{k + k_n}\left[e^{j(k+k_n)L} - 1\right] + \frac{i}{k - k_n}\left[e^{j(k-k_n)L} - 1\right]\} - (k_n^2 + k^2)\frac{2}{k_n}\int_0^L \frac{e^{jky}}{y} sin(k_n y)dy \tag{2.54}$$

The complex resonant frequencies s_n are then found by numerically searching for the roots to the equation:

$$F(\frac{s_n}{jc}) = 0 \quad for\ n = 1, 2, 3, \cdots \tag{2.55}$$

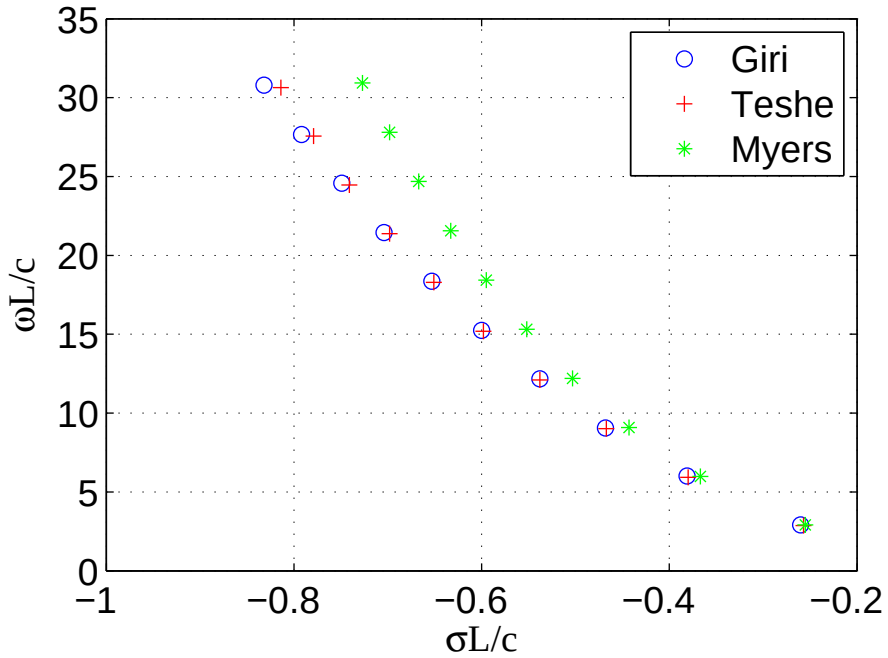

FIGURE 2.9: Overlay plots of the normalized resonant frequencies as computed by the methods of Giri, et al., Tesche and Myers, et al., for the wire with $a/L = 0.005$

Figure 2.9 shows a comparison of the first 10 normalized complex resonant frequencies $(\sigma + j\omega)L/c$ in layer 1, as computed by the methods of Giri [30], Tesche [28]

and Myers [31], for the specific case of a wire with $a/L = 0.005$. Because the results of [30] and [28] are both based on the same integral equation solution (but with a different method of searching) the resonant frequencies are very close.

2.6 Conclusion

In this chapter, background information has been provided on the electromagnetic theory. Next, the scattering theory has been presented which pointed the different models proposed for scattering. In particular, SEM which is used in time domain and GTD and its reduced complexity model which are used in frequency domain are presented. Finally theoretical analysis of the backscattered field from canonical objects has been presented. To have many CNRs or many scattering centers, the use of wide band frequency is necessary. In the next chapter, the UWB radar is presented in detail.

3

UWB Radar

3.1 Introduction

This chapter provides an overview of radars and the deficiencies of conventional radars. Next, we talk about the history, definition, application and advantages of Ultra WideBand (UWB) radars. Temporal and frequency techniques used to obtain a UWB spectrum are summarized in this chapter. Finally, we present an overview of the UWB radar in Automatic target classification (ATC).

3.2 Radars

Radar is an acronym for Radio Detection And Ranging, and as the name implies, radio energy is used to determine the attributes of a target. In its simplest form, a radar system consists of three subsystems (Figure 3.1): a transmitter, a receiver, and an antenna system. The transmitter generates an electrical signal that is radiated by the antenna system. If the signal is incident on a target, such as an airplane, vehicle, or an animal, it will be partially reflected back to the radar system. After amplification by the receiver and with the aid of proper signal processing, a decision

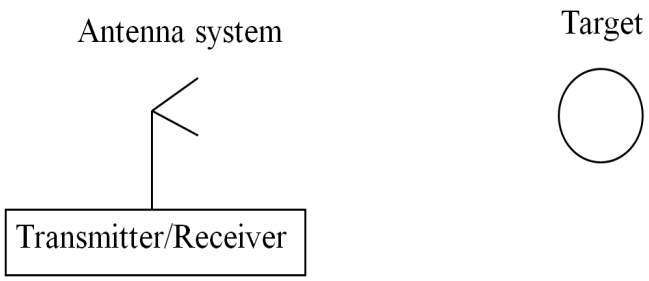

FIGURE 3.1: The radar system diagram

is made at the output of the receiver as to whether or not a target echo signal is present. At that time, the target location and other information about the target are acquired.

3.2.1 Information available from a radar

Several types of information can be collected by a radar:

- *Detection.* The radar is now employed in many divers uses, but its original purpose of detecting objects in some volume of space still constitutes a major part of all its applications. In this case, the user is interested in distinguishing targets in the illuminated volume from the clutter and noise that tend to obscure it.

- *Range.* The range to a target is determined by measuring the time it takes for the radar signal to propagate at the speed of light out to the target and back to the radar. No other sensor can measure the distance to a remote target at long range with the accuracy of radar. At modest ranges, the precision can be a few centimeters. The distance D is given by:

$$D = \frac{c \cdot \Delta T}{2} \tag{3.1}$$

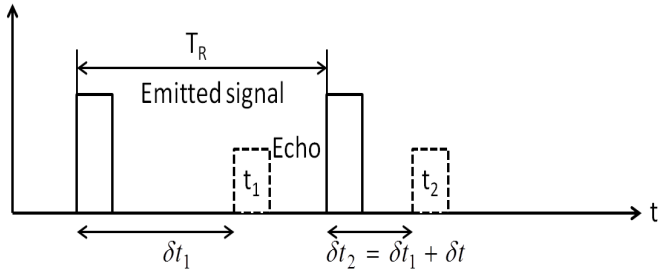

FIGURE 3.2: Schematic of the calculation of the velocity

where c is the speed of light, and ΔT is the temporal shift between transmission and reception of the radar signal.

- *Radial Velocity.* The radial velocity of a target is obtained from the rate of change of range over a period of time. It can also be obtained from the measurement of the Doppler frequency shift. The motion of the target implies that for two consecutively transmitted impulses, the time separating the transmission and reception of the radar echo is different for these two impulses. From this difference, the velocity of the target is deduced. The system emits a signal each T_R and receives the radiated echo by the target together with the generated temporal shift. If for the first echo, the shift is $\delta t_1 = \frac{2 \cdot D_1}{c}$ with D_1 the distance radar/target, for the next echo and because of the target motion, the temporal shift δt_2 will equal to δt_1 plus a quantity δt, positive if the target moves away and negative if it comes closer. If V_R is the velocity, then:

$$\delta t = \frac{2 \cdot V_R \cdot T_R}{c} \tag{3.2}$$

So, the velocity V_R of the target is:

$$V_R = \frac{c \cdot \delta t}{2 \cdot T_R} \tag{3.3}$$

- *Localization.* It can be realized by two methods: The first method is to determine the direction of the target by determining the angle where the magnitude

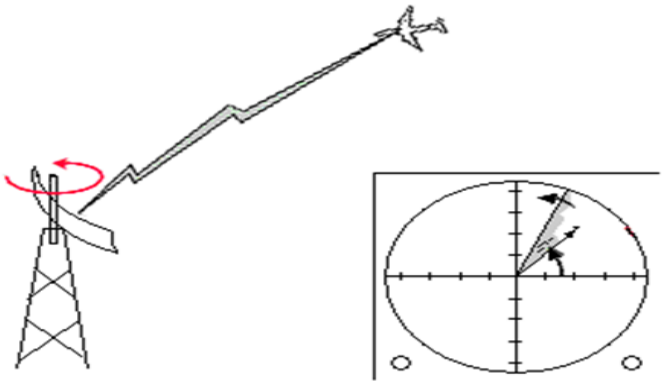

FIGURE 3.3: An air-surveillance radar

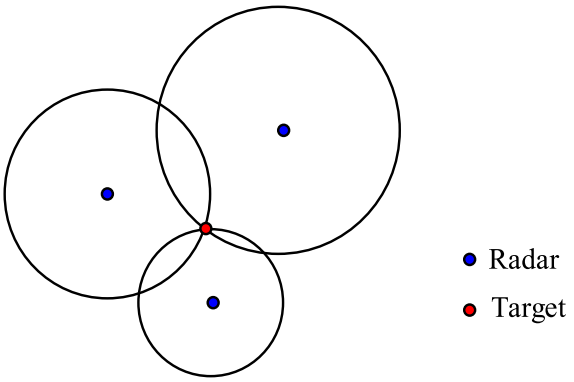

FIGURE 3.4: Target localization using three radars

of the echo signal from a scanning antenna is maximum. This usually requires a directional antenna. An air-surveillance radar with a rotating antenna beam determines angle in this manner (Figure 3.3). The second method is to use collected data from many measures realized in different points of the space. Multiple range measures between the target and the different radars are combined to produce a position. The target will be localized by finding the intersection point of different circles (Figure 3.4).

- *Radar imaging.* When the radar has sufficient resolution capability in range or

angle, it can provide a measurement of the target extent in the dimension of high resolution. Most of the imaging radars use two techniques, the first one is to use a very narrow beamwidth antennae. The second technique, employs the Doppler frequency domain based on Synthetic Aperture Radar (SAR) or Inverse Synthetic Aperture Radar (ISAR). There needs to be relative motion between the target and the radar, to obtain the synthetic aperture [12].

- *Target identification.* It can be done by comparing or correlating the received response with known targets. Applying classification methods is crucial for automatic target identification, more information will be given later in this dissertation.

3.2.2 The deficiencies of conventional radars

The majority of traditional radio systems use a narrow band of signal frequencies modulating a sinusoidal carrier signal. The reason is the simplicity of the oscillatory system based on an LC circuit. The resonant properties of this system allow an easy frequency selection of necessary signals. Therefore, frequency selection is the basic way of information channel division in radio engineering, and the majority of radio systems have a band of frequencies that is much lower than their carrier signal. The theory and practice of modern radio engineering are based on this feature.

Narrowband signals limit the information capability of radio systems, because the amount of the information transmitted in a unit of time is proportional to this band. Increasing the system's information capacity requires expanding its band of frequencies. The only alternative is to increase the information transmitting time.

The use of a relatively small bandwidth results in poor down-range resolution (with limited capability of discriminating between two closely spaced targets) and inability to accurately determine the range of the target. Due to the same reason, it is not capable of separating target from various sources of non-stationary clutter.

The new applications of the radar mostly require the use of imaging, obstacle crossing, target identification, and discretion. It is necessary to have important quantity of information collected by the radar in order to identify the target and a good accuracy to localize it. This requires radar working with a wideband frequency. Indeed, the wider bandwidth a system has the important information about the target it collects.

3.3 Historical review of UWB radar

The contributions to the development of Ultra WideBand radio frequency signals and their applications started in the 50s and 60s of the 20th century. Within the early phase of the development, terms such as baseband, carrier-free, impulse, time domain, non-sinusoidal, were commonly used to describe wideband techniques [32]. The term Ultra Wideband was introduced by the DARPA (US Defense Advanced Research Projects Agency) around 1990.

In the late 1960's, Harmuth, Ross and Robbins, and Etten started contributing to the development of the field addressing UWB radio frequency signals. The work of Harmuth was based on the basic design for UWB transmitters and receivers [33, 34, 35, 36, 37]. At approximately the same time and independently, Ross and Robbins [38, 39, 40] worked on the use of UWB signals in several application areas, including communications, radar, and using coding schemes. Both Harmuth, Ross and Robbins applied the 50 years old concept of matched filtering to UWB systems. Etten's empirical test of UWB radar systems resulted in developing system design and antenna concept [41]. In 1974, Morey designed a UWB radar system for ground penetration [42]. Other subsurface UWB radar designs followed [43].

In the late 1960s, Tektronix and Hewlett Packard developed oscilloscopes for UWB signals [44]; they also produced the first time domain instruments for diagnostics. In the 1960s both Lawrence Livermore National Laboratory and Los Alamos

National Laboratory performed original research on pulse transmitters, receivers and antennae. Cook and Bernfeld [45] presented the developments in pulse compression, matched filtering and correlation techniques that began in 1952 at the Sperry Gyroscope Company.

In the 1970s Lawrence Livermore National Laboratory expanded its laser-based diagnostics research into pulse diagnostics. Thus, by the early 1970s basic designs for UWB signal systems were done, however, no strong efforts could be observed in perfecting such systems. In fact, by 1975 a UWB system for communications or radar could be constructed from components purchased from Tektronix. After the 1970s, the only innovations in the UWB field could come from improvements of some parts within the UWB system. The basic known components were pulse train generators, pulse train modulators, switching pulse train generators, detection receivers and wideband antennae. Moreover, particular information about the subcomponents and methodologies were also known, such as avalanche transistor switches, light responsive switches, use of "subcarriers" in coding pulse trains, integration and averaging matched filters, template signal match detectors, correlation detectors, signal integrators, synchronous detectors and antennae driven by stepped amplitude input.

In 1978, Bennett and Ross [46] summarized the known pulse generation methods. Since that time there have been numerous sessions at various conferences, where the many approaches to pulse generation techniques have been, and, continue to be, discussed.

In 1988, Barret was able to organize a UWB workshop for the US Department of Defense's Director of Defense Research and Engineering attended by over 100 participants [47]. At this time, there was already substantial progress in UWB in the former Soviet Union/Russian Federation and China, which paralleled the progress in the US. There were also very active academic programs (e.g., at LLNL,

LANL, University of Michigan, University of Rochester and Polytechnic University, Brooklyn) which focused on the interesting physics of short pulse transmissions that differed from the physics of continuous or long pulse signals, especially with respect to interactions with matter.

With the conference held at W.J. Schafer Associates [47] and one at Los Alamos National Laboratory in 1991 [48], there have been numerous meetings held on impulse radar/radio [49, 50, 51, 52, 53, 54, 55, 56].

In 1994, McEwan, invented the Micropower Impulse Radar (MIR) which provided for the first time a UWB operating at ultralow power, besides being extremely compact and inexpensive [57]. This was the first UWB radar that required only microwatts of power to operate.

During the 90s, activities in UWB communications and radar gradually increased. Laboratories built experimental UWB radars: the BoomSAR of the Army Research Laboratory for mine detection and foliage penetration [58]; and the Microwave Microscope of the Naval Research Laboratory for characterizing the sea spikes associated with ocean scattering in naval radars [59]. These research systems were accompanied by several developments in the commercial sector like Multispectral Solutions, Inc. and Time Domain, Inc. This commercial advocacy of UWB systems led to the US FCC's (Federal Communication Commission) Notice of Inquiry for Part 15 usage by UWB systems in 1998 and to the subsequent Report and Order for Part 15 acceptance of UWB systems in 2002 [60].

3.4 Definition of UWB

The term UWB is used to represent a radio technique which was studied under various names. In the earliest works on this field, we can find the terms impulse radio, carrier-free radio, baseband radio, time domain radio, non-sinusoid radio, orthogonal function radio and large relative bandwidth radio. The term UWB was coined by

the US Department of Defense in the late 1980s [61].

According to the definition of US FCC, a signal is called UWB if it has an absolute bandwidth of at least 500 MHz, or a fractional bandwidth larger than 0.2. The absolute bandwidth is calculated as the difference between the upper frequency f_H of the -10 dB transmission point and the lower frequency f_L of the -10 dB transmission point:

$$B = f_H - f_L \tag{3.4}$$

which is also called 10 dB bandwidth, as shown in figure 3.5. On the other hand, the fractional bandwidth is defined as:

$$B_{frac} = \frac{B}{f_c} \tag{3.5}$$

where f_c is the center frequency given by:

$$f_c = \frac{f_H + f_L}{2} \tag{3.6}$$

From (3.4) and (3.6), the fractional bandwidth B_{frac} in (3.5) can be expressed as:

$$B_{frac} = \frac{2(f_H - f_L)}{(f_H + f_L)} \tag{3.7}$$

According to the FCC, a UWB system with f_c larger than 2.5 GHz must have an absolute bandwidth larger than 500 MHz, and a UWB system with f_c smaller than 2.5 GHz must have a fractional bandwidth larger than 0.2.

Due to their large bandwidth, UWB systems are characterized by very short duration waveforms, usually on the order of a nanosecond.

Figure 3.6 illustrates the comparison between conventional radio systems, which generally modulate a narrowband signal on a carrier frequency, wideband systems, with spreading spectrum for example, and ultra-wideband systems, which show a weak power spectral density. As a comparison, the bandwidth of UMTS (Universal

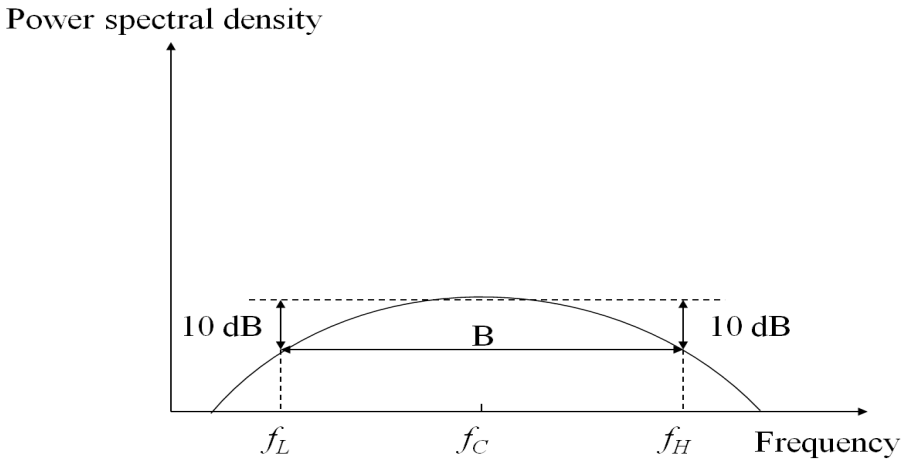

FIGURE 3.5: A UWB signal is defined to have an absolute bandwidth $B \geq 500MHz$, or a fractional bandwidth greater than 0.2

Mobile Telecommunications System) signals, the third generation of mobile communication, is 5 MHz.

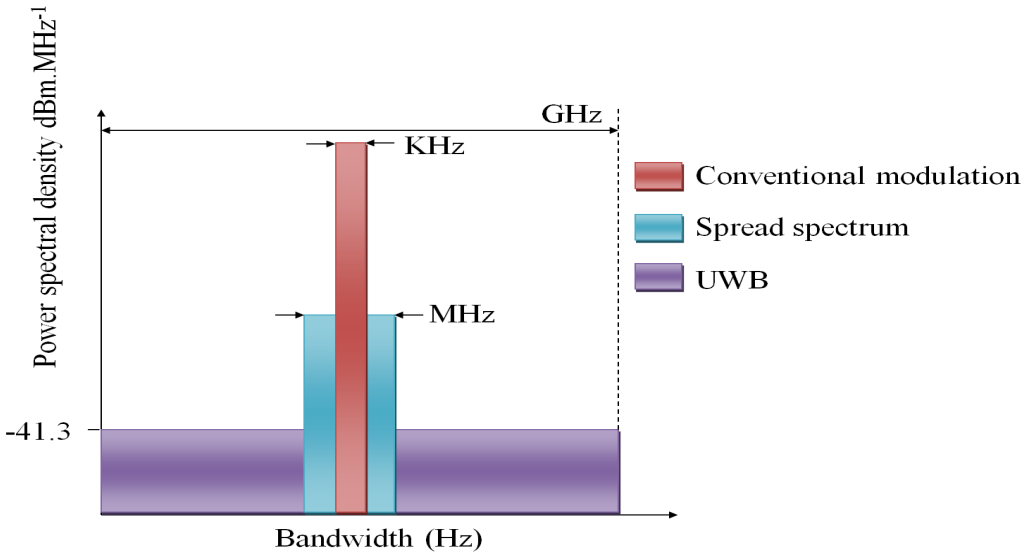

FIGURE 3.6: Comparison of various radio system spectrums

3.5 Application of ultra-wideband sensing

As long as the UWB sensors should be accessible for a larger community, they must be restricted to low power transmissions which entitles them to short range sensing, up to about 100 m.

UWB techniques have been used for a variety of applications including:

- *Ground penetrating radar (GPR).* Ground-Penetrating Radar is a geophysical method that uses radar pulses to image the subsurface. This method detects the reflected signals from subsurface structures. GPR can be used in a variety of media, including rock, soil, ice, fresh water, pavements and structures. It can detect objects, changes in material, and voids and cracks. GPRs are typically carrier-free or employ a low frequency carrier (500 MHz); the low frequency content of the transmitted signal allows it to penetrate materials such as concrete and soil more readily than a higher frequency signal.

  Consider a metallic object buried in the ground. The transmitted signal will be reflected from the object and, after some time delay, the reflected signal will be incident on the receive antenna. The distance to the buried object can be determined based on the time delay; which means, GPR employs time-domain techniques to locate any discontinuities in the otherwise opaque target.

  The GPR has been widely used by engineers in civilian and military domains since the 70s. However, the first GPRs allowing good performances have been commercialized in the early 90s. Since then, the number of users of this technique has been growing, and the GPRs are today employed in a variety of applications: detection of buried mines, fossils detection, evalulation of pavements, study of the subsurface structure of the moon, etc [62, 63, 64, 65, 66, 67, 68].

- *Strong clutter penetration radar.* Similar to GPR, Strong clutter penetrating

radars utilize low frequency, wideband transmitted signals to detect and identify objects that are embedded in foliage, soil cover or buildings. The efficient and accurate detection provides a broad range of applications, such as locating weapon caches during military operations and rescuing people from natural disasters. In [69], a UWB radar was used to detect the target obscured by foliage by applying signal processing approaches.

- *Collision avoidance systems.* the requirements for advanced automotive safety and driver assistance systems are being made stricter to avoid or mitigate accidents at an early stage. Radar sensors are commonly used because of their robust obstacle detection even under adverse weather conditions. Because of diverse highway and urban scenarios, radar sensors must cope with different target types and scenarios. To realize automatic brake assistances or adaptive cruise control systems, they must observe forward targets and determine their exact location. In [70], a synthetic aperture radar is used in order to evaluate 3D scattering centers of two different vehicles.

- *UWB for medicine.* The inherent features of the UWB radio signals make them highly suitable for less invasive medical application. For example, the UWB radar may be used in novel noninvasive sensing and imaging techniques thanks to its high temporal resolution for detecting backscattered signals. In [71], the authors described their current research on the application of the UWB technology to noninvasive measurement of blood pressure. In addition, they reported a survey of recent research in UWB technology for medical sensing and communications.

  UWB radar can be used for early-breast cancer detection as it does not involve the use of ionising radiation (as is the case of X-Ray mammography). The UWB Radar Imaging involves illuminating the breast with a UWB pulse, and

recording the resulting backscattered signals. Signal processing techniques such as beamforming, or time-reversal imaging can then be applied to the received space-time backscatter to detect and localize significant scattering regions, such as malignant tumors [72].

- *Short range communications.* One of the most popular applications of UWB is data transmission with a very high rate (more than 500 Mbit/s) [73]. The range of such systems is limited to some 10 m. Networks that cover such a short range are often called personal area networks (PANs). High-data-rate PANs are used especially for consumer electronics and personal computing applications. Examples include the transmission of HDTV (high definition television) streams from a set-top box or a DVD player to the TV requires high data rates and wireless USB (universal serial bus), which aims to transmit data at 480 Mbit/s between different components of a computer. The company: Samsung, made a monitor fitted with a UWB technology, which allows the user to connect it to a notebook or a desktop wirelessly.

  The UWB technology can also be used in low data rate communication. UWB technology is less affected by shadows and allows the transmission through objects. The innovative communication method of UWB at low data rate gives numerous benefits to government and private sectors. For instance, the wireless connection of computer peripherals such as mouse, monitor, keyboard, joystick and printer can utilize UWB technology. UWB allows the operation of multiples devices without interference at the same time in the same space.

- *Postion location and tracking.* locating patient in case of critical condition, hikers injured in remote area, tracking cars, and managing a variety of goods in a big shopping mall, are all an example of the benefits of position location and tracking. For active RF tracking and positioning applications, the short-pulse

UWB techniques offer distinct advantages in precision time-of-flight measurement, multipath immunity for leading edge detection, and low prime power requirements for extended-operation RF identification (RFID) tags. The reason of supporting human-space intervention is to identify the persons and the objects the user aims at, and identifying the target task of the user. Knowing where a person is, we can figure out near to what or who this person is and finally make a hypothesis what the user is aiming at [74].

3.6 Advantages of Ultra-Wideband Radar

Most of the advantages of UWB systems are associated with the bandwidth that is achieved. Basically, the wider bandwidth a system has the better it performs. Since UWB achieves the highest bandwidth, its performance is maximized. The advantages of UWB radar are listed below:

- Identification of target class because a received signal carries the information not only about the target as a whole, but also about its separate elements. Furthermore, the large bandwidth improves the radar resolution, which allows the discrimination of two or several closely located targets.

- Rise in protection against passive interference from rain, mist, aerosols, etc. This is because the scattering cross-section of interference source within a small pulse volume is less relative to the target scattering cross-section.

- Detection of hidden targets and investigation of opaque structures. At one hand microwave penetration in most of substances or randomly distributed bodies (foliage, soil) is restricted to low frequencies but on the other hand reasonable range resolution requires bandwidth. To bring both aspects together, the fractional bandwidth must be large. The absolute bandwidth is typically limited by the properties of the propagation medium.

- Typical power transmission levels for short-range UWB radar systems are in the milliwatt range, although levels in the watt range are not uncommon.
- Simpler implementation and lower cost compared to the traditional radar.
- UWB radar can be used in intelligent vehicles for localization, communication and obstacles detection. Due to the use of a very wide bandwidth, transmission is achieved with high data rate, it is also possible to achieve high precision ranging and positioning. Therefore, application of UWB is widely researched in intelligent transport systems radars, indoor ranging and positioning, etc [75, 76].
- Improvement of the radar's immunity to external narrowband electromagnetic radiation effects and noise.

3.7 UWB techniques

Several waveforms can be used to obtain a UWB spectrum, but two techniques can be distinguished: temporal techniques where the emitted signals can be pulses or random noises. And harmonic techniques which use sinusoidal signals with modulated frequency like step frequency or Frequency Modulated Continuous Wave (FMCW). In this case, the measure is performed in frequency domain. Figure 3.7 shows an overview of the different UWB techniques.

3.7.1 Impulse radar

The principle of a UWB impulse radar consists of transmission of a sequence of N ultra-short pulses $u(t)$ with fixed time interval T_R , also called Pulse Repetition Interval (PRI):

$$s(t) = \sum_{n=0}^{N-1} u(t - nT_R) \tag{3.8}$$

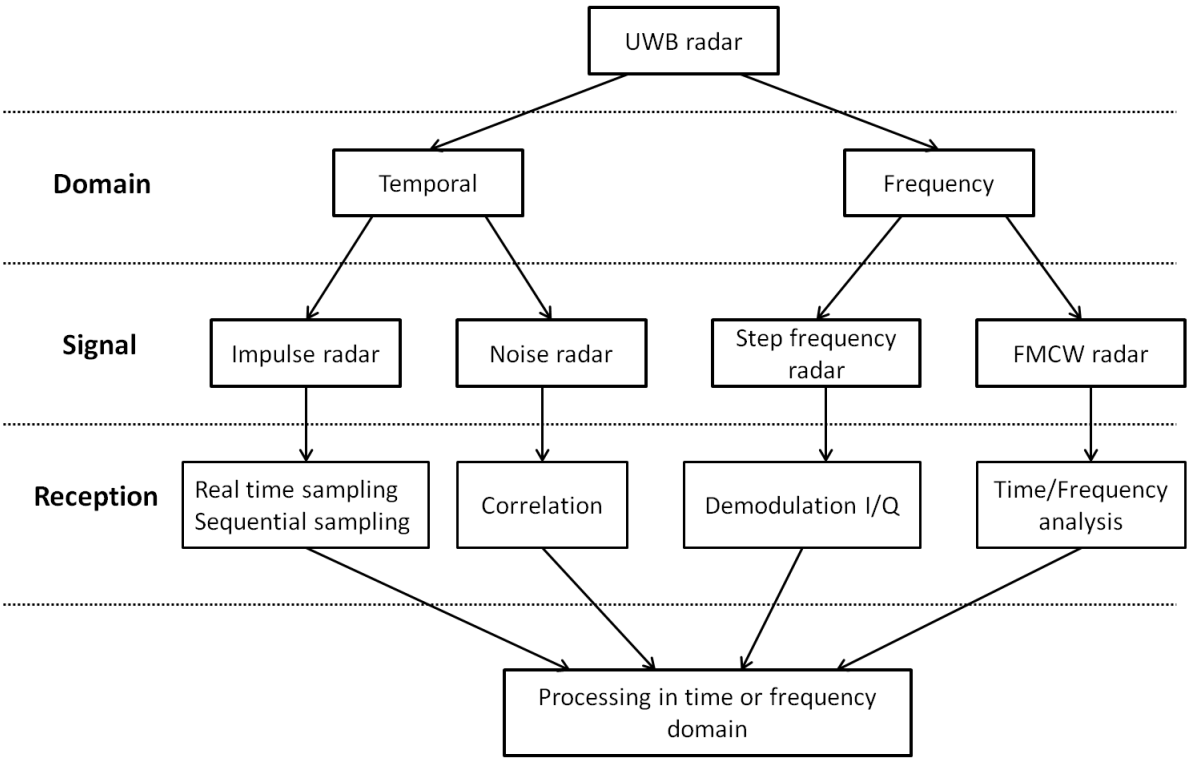

FIGURE 3.7: The different UWB techniques

The pulse widths are in the order of tens of picoseconds. The instantaneous equivalent spectrum of the pulse is between several MHz and several GHz. The most commonly generated pulse shapes are monopulse (Gaussian-like pulse), monocycle (first-order derivative of the monopulse) and ramp pulse. In impulse radar a short pulse is applied directly to the transmitter antenna. The transmitter antenna works as a filter, therefore, a band pass signal is radiated from the antenna. The transfer function of the antenna determines the shape and bandwidth of the radiated signal. In order to shape the spectrum, a filter may also be put in front of the antenna. The received signal needs to be sampled and stored for further treatment.

Due to baseband (carrier-less) nature of impulse radio UWB signals, frequency upconversion and down-conversion is not required in the radar system. This reduces

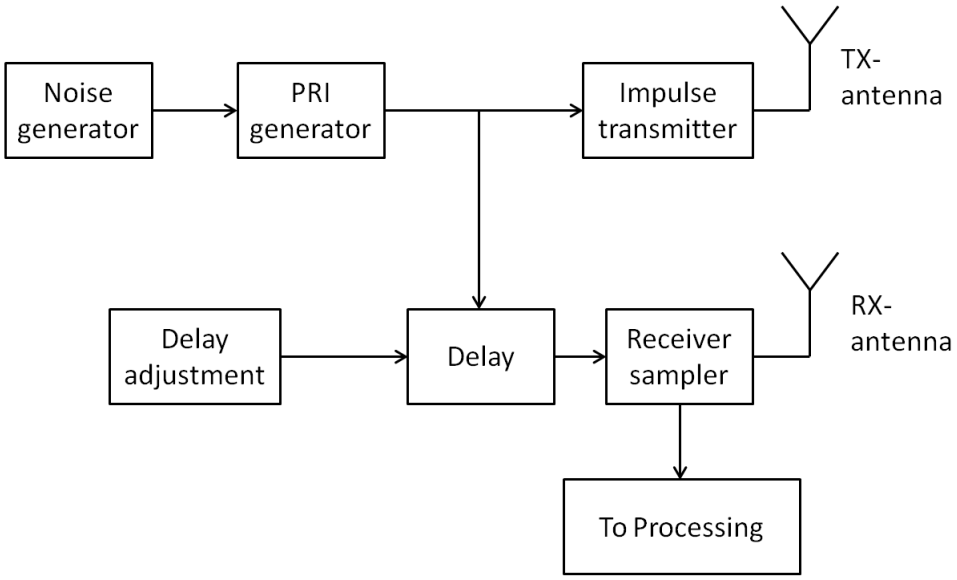

FIGURE 3.8: Impulse radar with sequential sampling

the complexity and power consumption of radar.

In reception, a real time sampling is used. But in UWB impulse radars, the highest frequency can be several GHz so that an Analog to Digital Converter (ADC) that can sample at this speed with several bit resolution is very difficult to manufacture and would be expensive and power consuming. A solution to this problem, called sequential sampling technique, is to take only one receive sample for each transmitted pulse. Then the ADC only needs to take one sample every pulse repetition interval (PRI) so the need for high speed ADC is avoided.

Figure 3.8 shows a block diagram of impulse radar with sequential sampling [77]. A noise generator is controlling the trigger of the transmitted pulse. This is to randomize the PRI of the pulse train and thereby reduce peaks and smooth the transmitted spectrum. The PRI-generator triggers the impulse transmitter. The trigger signal is delayed a certain amount before being used to trigger the receiver sampler to take one range sample. The delay is shifted before the next sample is

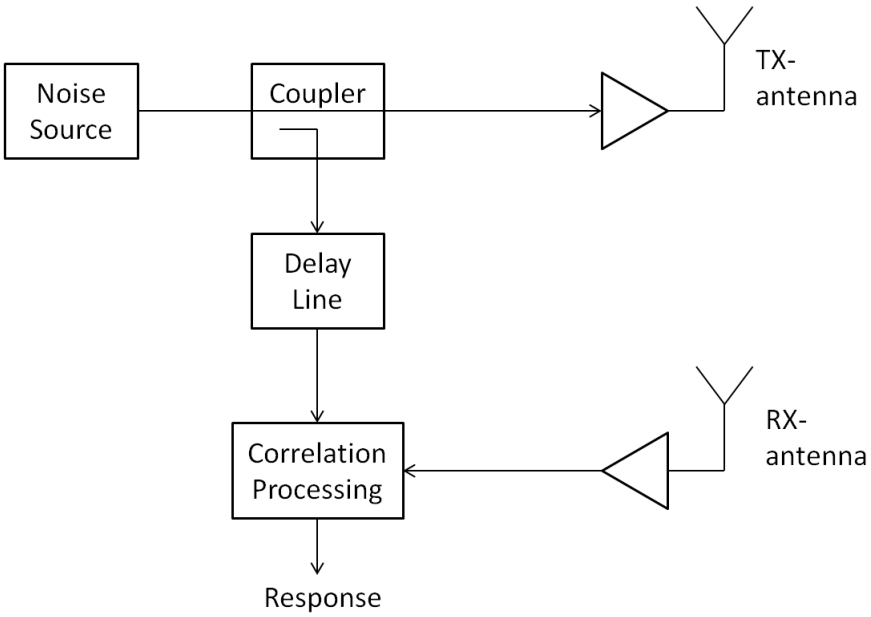

FIGURE 3.9: Block diagram of a noise radar

taken. In this radar a multi bit high resolution ADC can be used.

3.7.2 Noise radar

A random noise signal is generated by a source and transmitted by an antenna (Figure 3.9). A receiving antenna receives the reflected signal after a time given by the two way travel time delay. After amplification, the received signal is correlated with a reference signal. The reference signal, which is a delayed version of the transmitted noise signal, when it is delayed the same amount as the received signal a strong correlation value would be expected.

There are many ways to implement the delay line. A cable with a given length providing the correct delay is the simple way.

Concerning the correlator, a mixer and a low pass filter can be used. Another implementation is using a digital RF-memory where the transmitted signal is sampled and delayed digitally before converted to analog signal and correlated with the

received signal.

In order to have a long range, the radar must emit sufficient energy, thus, it emits long signals in time. A long signal in time offers a low resolution because the frequency band is inversely proportional to the temporal width.

To obtain high-range resolution with long signals, pulse compression method is used in the noise radar [78]. Pulse compression can provide the fine range resolution of impulse signals with the high signal energy of conventional narrowband radars. Because range resolution depends solely on the bandwidth, encoding can increase the signal bandwidth to give wideband signal resolution the longduration, low-power, and high-energy signals needed for long-range target detection. Pulse compression method is based on generating long waveforms by coding the transmitted signal and the processing of the received signal by a correlation processor. There are a number of codes that can be used for pulse compression. The codes are selected based on their length and on their autocorrelation properties.

3.7.3 Step frequency radar

Radars employing a step-frequency waveform increase the frequency of successive pulses linearly in discrete steps. The different pulses will sum up, and the transmitted signal will be a pulse train. The repetition interval is determined by the distance between the transmitted frequencies. A pulse train can also be synthesized by transmitting the different frequencies one at a time and summing them up afterwards. The step frequency radar does this and transmits single tone frequencies in sequence where only one frequency is transmitted at a time.

Figure 3.10 shows a group of N coherent pulses whose frequencies are increased from pulse to pulse by a fixed frequency increment df. The frequency of the nth pulse can be written as:

$$f_n = f_0 + n \cdot df \tag{3.9}$$

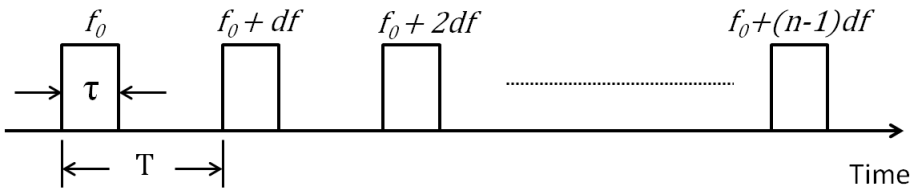

FIGURE 3.10: Step-frequency waveform

where f_0 is the starting carrier frequency and df is the frequency step size, that is, the change in frequency from pulse to pulse. Each pulse is τ seconds wide, and the time interval between the pulses is equal to T. Note that the frequency stays constant within each pulse.

A step-frequency radar has a narrow instantaneous bandwidth (corresponding to individual pulse) and attains a large effective bandwidth (corresponding to frequency spread of pulses within a burst) sequentially over many pulses in the processor. As a result, the hardware requirements become less stringent. Lower-speed ADC (commensurate with the low bandwidth of individual pulses) and slower processors can be used for reduced data. The receiver bandwidth would be smaller, resulting in lower noise bandwidth and a higher signal-to-noise ratio.

Figure 3.11 shows a block diagram of a step frequency radar. An oscillator generates the correct frequency that is transmitted by an antenna. The received signal is captured by the receiver antenna and amplified before it is multiplied with the same signal as transmitted. The signal after the mixer is low pass filtered and sampled in an I and Q detector. The I and Q detector can be implemented after the signal has been sampled.

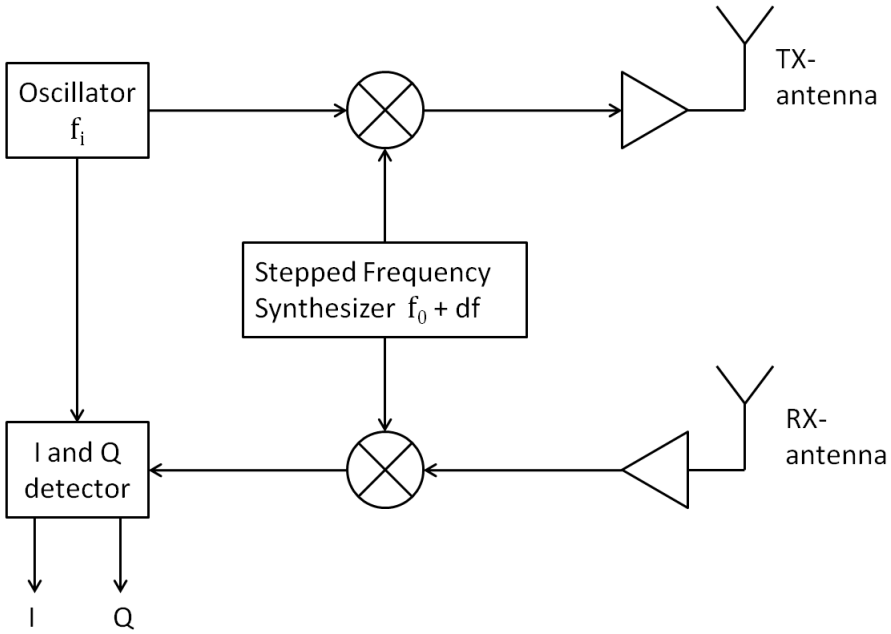

FIGURE 3.11: Block diagram of step-frequency radar

3.7.4 Frequency modulated continuous wave radar

The Frequency Modulated Continuous Wave (FMCW) radar is widely used technique in UWB systems. This radar is also collecting the data in the frequency domain as with the step frequency radar technique. In stead of changing the frequency in steps, the frequency is changed linearly as a function of time (Figure 3.12). A linear frequency modulation is a particular case of FMCW that we will explain in this subsection.

Figure 3.13 shows a block diagram of an FMCW radar. A voltage-controlled oscillator (VCO) forms the signal source that is modulated as a linear frequency ramp. The signal is then transmitted to the transmitter antenna. Next, the reflected signal by a target is received by a receiver antenna, and it is treated to extract needed information from it.

The FMCW radars are easily overwhelmed by interference from pulse radars.

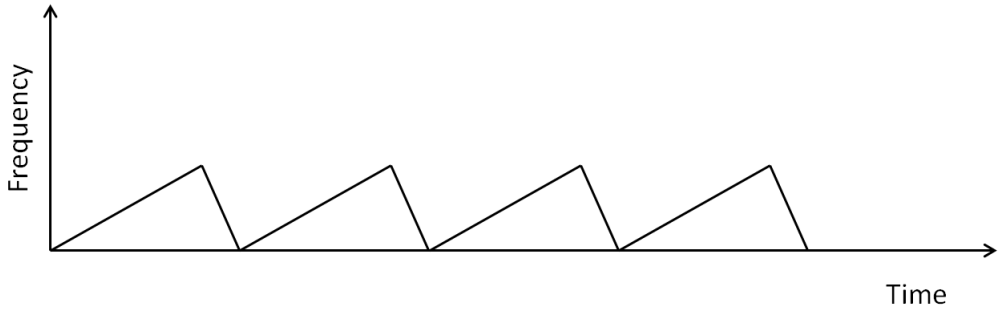

FIGURE 3.12: The principle of operation of an FMCW radar

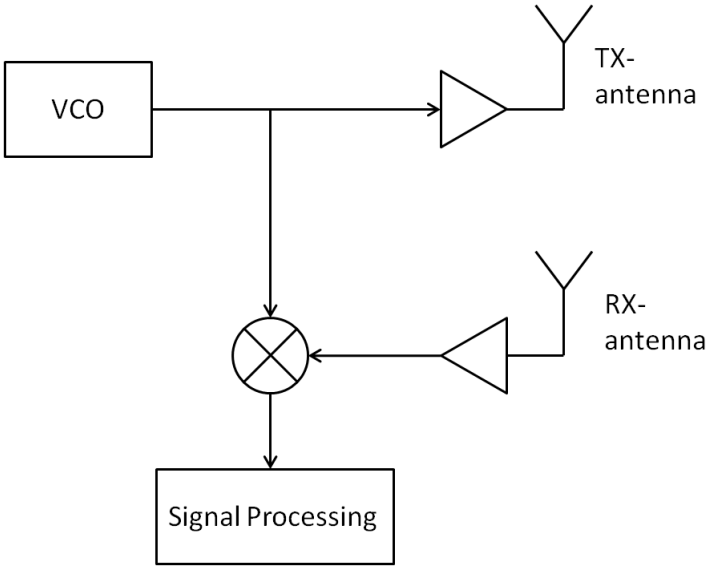

FIGURE 3.13: Block diagram of an FMCW radar

Also, they potentially get confused by onboard reflectors such as masts and satellite antennae.

3.7.5 Conclusion

In our experiments we use the impulse radar for several reasons. Firstly, the radar system is simplified. It is composed by only a generator, sampler and antennae. There is no demodulator, correlator, etc. Moreover, the impulse radar is robust

against other perturbations like: clouds and rains. The radar can be designed with coherent operation which allows energy received from subsequent pulses to be summed and by integrating these multiple returns it is possible to increase the Signal-to-Noise Ratio (SNR). In addition, it provides accurate, high rate range measurements. Finally, the UWB chipset enables low cost, small size, and low power operation which is convenient in autonomous vehicles.

3.8 UWB radar in Automatic target classification

The principal objective of ATC is to identify the target from UWB radar. The identification of the target will be realized by the comparison between the deduced target properties and the different target features already recorded in a database.

After the radar has transmitted the pulse train, the first step is to detect whether or not a target is present in the data. At this stage it may be determined that no targets of interest are present and it is not necessary to carry out further processing. If a target exists there are two processing methods for target identification and recognition. One method is based on the radar reconstruction of image to show the detected target. The other method is based on ATC and exploits the information stored in the signal echoes. In our work, we seek to determine the nature of the target and not the target view, hence we opt for the second method. This method is based on ATC and consists of the following successive stages:

- Signal preprocessing. The aim of signal preprocessing in ATC is to prepare and condition the acquired signal in order to simplify the feature extraction and later classification of the required target. Generally for the signal preprocessing, filtering and normalization are used. Filtering is applied in order to remove unwanted signals coming from all objects surrounding the radar. These unwanted signals that are included in the recorded signal act as clutter and

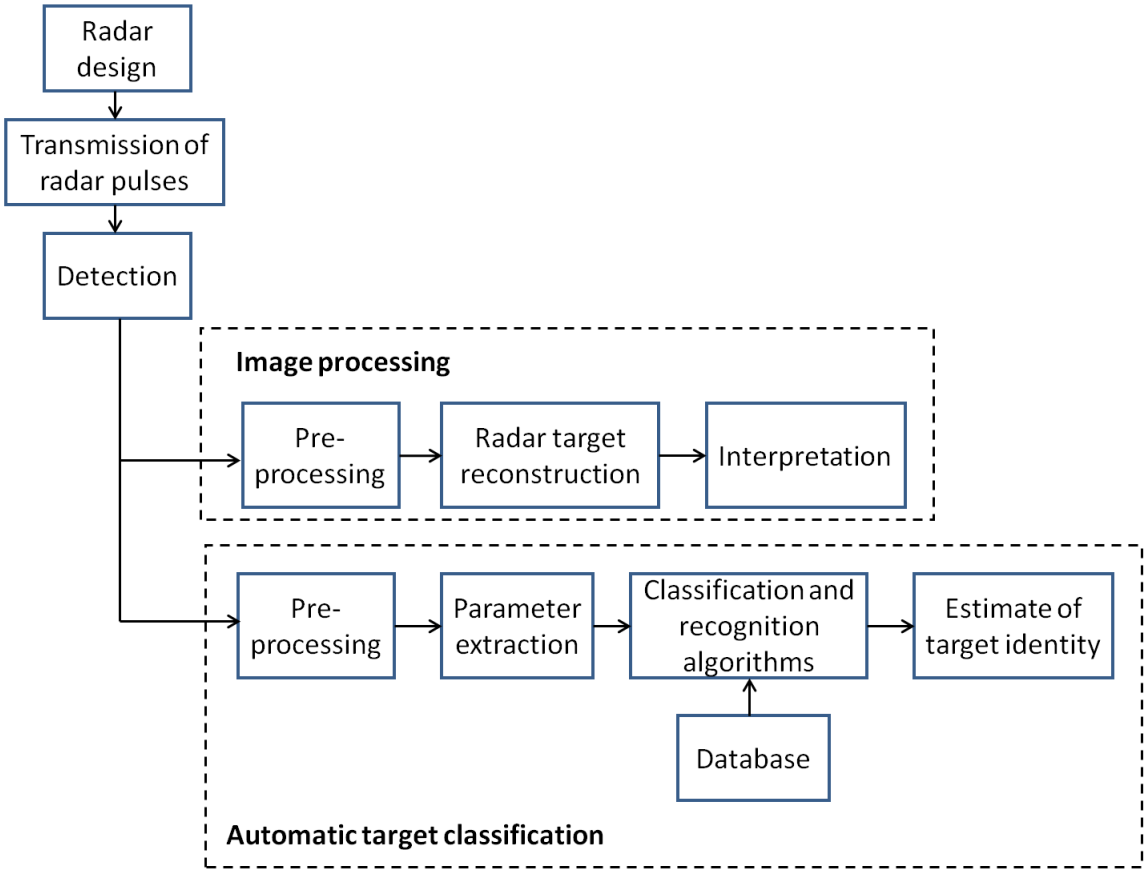

FIGURE 3.14: Overview of the target recognition process

noise . The normalizing process conditions the signal to make it independent of the data acquisition situation. For example, the amplitude of a scattered field by an object will change if the distance of this object from the radar changes. Therefore, the amplitude of the scattered field must be normalized before feature extraction.

In the case where we have a signal in time domain obtained by a radar using temporal technique, and we want to apply a feature extraction method in frequency domain, an FFT is applied on the signal in this step of signal preprocessing.

- Feature extraction. Feature extraction is the process of obtaining a useful subset of information about a target from an entire measured signal. The best handling of the feature extraction consists of understanding the physical behavior of a radar system in its environment. Based on this understanding, features must then be mathematically described depending on the given requirements.

  A variety of algorithms for feature extraction are possible. In our thesis, we have used wavelet transform and high resolution methods.

- Classification and recognition algorithms. The previous two phases, preprocessing and feature extraction, aimed to extract the essential information about the observed signals and present it in the most appropriate and condensed form to the classifier. From this point, the quality of decision made depends only on the classifier choice and its implementation.

  The extracted features are compared with the information in the reference library and classified to the object giving the best match. In general, there are two phases in constructing a classification system: training phase and testing phase. In the training phase, the learning algorithm is applied on a subset of the dataset, called training data. This results in a trained model. In the testing phase, another subset of the data, called test data, is evaluated using the model created in the training phase.

3.9 Conclusion

In this chapter, the deficiencies of conventional radar have been presented. The history, definition, application and advantages of UWB radar have been provided. The temporal and frequency techniques used in UWB radar have been presented. We showed the advantages of the impulse radar and why it is suitable for autonomous vehicles. Finally, the different steps of automatic target classification by using UWB

radar have been described. In the next chapter we will present the methods used for feature extraction and for classification.

4

Radar automatic target classification

4.1 Introduction

A major aim of this thesis is to investigate the variation of classification performance with key parameters of the signal processing and feature extraction methods applicable to backscattered signals from UWB radar. In ATC, the two main steps are feature extraction and classification. In this chapter, firstly we present the methods used for feature extraction in our work which are wavelet transform and high resolution techniques. Then, we present the methods used for classification which include Mahalanobis Distance Classifier (MDC), Naïve Bayes (NB), k-Nearest Neighbors (k-NN) and Support Vector Machine (SVM). In order to evaluate and compare the different methods of classification, cross validation method is applied which is explained in this chapter.

4.2 Feature extraction

The UWB backscattered signals from unknown targets are firstly processed through a feature extraction method so that the most relevant features from each signal can

be highlighted and forwarded to the classification algorithms. The methods used for feature extraction in our work include wavelet transform and high resolution methods which are detailed below.

4.2.1 Wavelet transform

The wavelet transform has been found to be particularly useful for analysing signals which can best be described as aperiodic, noisy, transient, etc. Its ability to examine the signal simultaneously in both time and frequency has generated a number of sophisticated wavelet-based methods for signal processing. Many of the ideas behind wavelet transforms have been in existence for a long time. However, wavelet transform analysis as we now know it really began in the mid-1980s where they were developed to interrogate seismic signals. The application of wavelet transform analysis in science and engineering really began to take off at the beginning of the 1990s, with a rapid growth in the numbers of researchers turning their attention to wavelet analysis during that decade.

Wavelets are used to transform the signal under investigation into another representation which presents the signal information in a more useful form. This transformation of the signal is known as the wavelet transform. Mathematically speaking, the wavelet transform is a convolution of the wavelet function with the signal. The Discrete Wavelet Transform (DWT) can be used as a feature extraction method by producing wavelet coefficients which may be used as discriminant bases for classification methods [79, 80]. Before explaining how we use the DWT for feature extraction, we first present the Continuous Wavelet Transform (CWT).

Continuous Wavelet Transform

The CWT of a signal $x(t)$ is defined as [81]:

$$T(a,b) = \int_{-\infty}^{+\infty} x(t)\psi_{a,b}^{*}(t)dt = \langle x(t), \psi_{a,b}(t) \rangle \tag{4.1}$$

where $(^*)$ denotes complex conjugate, $\psi(t)$ is the mother wavelet function. The time location is determined by the term:

$$\psi_{a,b}(t) = \frac{1}{\sqrt{a}}\psi(\frac{t-b}{a}) \tag{4.2}$$

where $\psi_{a,b}(t)$ is a set of wavelets generated from $\psi(t)$, which expands and attenuates as a increases or diminishes, respectively. In addition, $\psi(t)$ shifts in the time domain as b changes.

The energie E of a wavelet must be finite:

$$E = \int_{-\infty}^{+\infty} |\psi(t)|^2 \, dt < \infty \tag{4.3}$$

If $\hat{\psi}(f)$ is the Fourier transform of $\psi(t)$:

$$\hat{\psi}(f) = \int_{-\infty}^{+\infty} \psi(t)e^{-j(2\pi f)t}dt \tag{4.4}$$

The wavelet $\psi(t)$ must have a zero mean:

$$\int_{-\infty}^{+\infty} \psi(t)dt = 0 \tag{4.5}$$

and therefore it must be oscillatory. In other words, $\psi(t)$ must be a wave.

There is an inverse wavelet transform, defined as:

$$x(t) = \frac{1}{C_\psi} \int_{-\infty}^{+\infty} \int_{0}^{+\infty} T(a,b)\psi_{a,b}(t)\frac{da \; db}{a^2} \tag{4.6}$$

where:

$$C_\psi = \int_0^{+\infty} \frac{|\psi(f)|^2}{f} df < \infty \tag{4.7}$$

This allows the original signal to be recovered from its wavelet transform by integrating over all scales and locations, a and b.

Discrete Wavelet Transform

The DWT is obtained by considering that parameters of scaling a and shifting b take discrete values: $a = a_0^i$, $b = kb_0a_0^i$, with i, $k \in Z$, $a_0 > 1$ and $b_0 > 0$. Replacing these values in (4.1) yields:

$$T_{i,k} = \frac{1}{\sqrt{a_0^i}} \int_{-\infty}^{+\infty} x(t)\psi(a_0^{-i}t - kb_0)dt = \langle x(t), \psi_{i,k}(t) \rangle \tag{4.8}$$

When the DWT is applied to a set of radar target signals, the wavelet coefficients are obtained by the decomposition Low-Pass Filter (LPF) and the decomposition High-Pass Filter (HPF).

Given samples $c(n)$ of the signal, two sets of coefficients are produced: approximation coefficients cA_1, and detail coefficients cD_1. These vectors of coefficients are obtained by convolving c_n with the the low-pass filter for approximation, and with the high-pass filter for detail, followed by decimation process which divides the number of samples by two (figure 4.1).

$$cA_1(n) = \sum_k h(k - 2n)c(n) \tag{4.9}$$

$$cD_1(n) = \sum_k g(k - 2n)c(n) \tag{4.10}$$

Here, $h(n)$ and $g(n)$ are the associated filter coefficients that decompose $c(n)$ into $cA_1(n)$ and $cD_1(n)$ respectively. The coefficients of the filters $h(n)$ and $g(n)$ are associated with the selected mother wavelet.

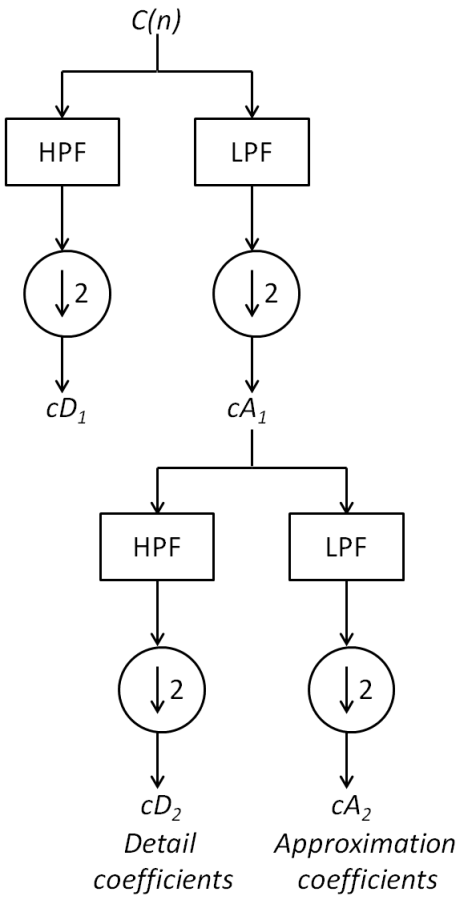

FIGURE 4.1: Wavelet decomposition scheme

The chosen wavelets in our work are Coiflet 5 (coif 5) and Daubechies 4 (db4), as they gave the best performance.

The next step splits the approximation coefficients cA_1 in two parts using the same scheme, replacing $c(n)$ by cA_1, and producing cA_2 and cD_2, etc. With these coefficients it is possible to reconstruct the signal by inserting zeros between samples. Then, these sequences are processed using the low pass and high pass filters.

Let's M be the order of decomposition. The total energy of the discrete input

signal is given by:

$$E = (cA_M)^2 + \sum_{m=1}^{M} (cD_m)^2 \tag{4.11}$$

The $(M+1)$ terms of this equation are used to build the database corresponding to wavelet feature data. In our simulations, we take $M = 1, 2, \ldots, 5$.

4.2.2 High resolution methods

High resolution methods are applied on the desired and/or undesired signal components present in a given set of data to estimate and/or detect them. The term high resolution implies a good ability to separate very similar signal components. The parametric high resolution methods result from ingenious exploitations of known data structures.

In this section, we present four parametric methods: Prony's method, Root-MUltiple SIgnal Classification (Root-MUSIC), Estimation of Signal Parameters via Rotational Invariance Techniques (ESPRIT) and Matrix Pencil Method (MPM).

Prony's method

In 1795, Prony described a method for modeling experimental data as a linear combination of damped exponentials [82]. The principle of this method is to transform the nonlinear problem of finding damping factors in a linear problem. The exponentials that have to be found are the roots of a polynomial and estimating the coefficients of this polynomial is a linear problem. Prony treated the case of real exponentials but the principle remains the same if we extend the problem to the case of complex exponentials.

Prony's method is a decomposition of a signal $y(t)$ with M complex exponentials.

$y(t)$ is written as follows:

$$y(t) = \sum_{i=1}^{M} R_i e^{(\alpha_i + j\omega_i)t} \tag{4.12}$$

Firstly, Prony's method regularly samples $y(t)$ so that it will be written as:

$$\begin{aligned} y(nT_s) &= \sum_{i=1}^{M} R_i e^{(\alpha_i + j\omega_i)nT_s} \\ &= \sum_{i=1}^{M} R_i z_i^n \end{aligned} \tag{4.13}$$

The key to Prony's Method is that the coefficients in the difference equation are related to the following polynomial:

$$\prod_{i=1}^{M}(1 - \frac{z_i}{z}) = \sum_{i=0}^{M} p_i z^{-i} = 0 \tag{4.14}$$

with $p_0 = 1$.

Because the summation of complex exponentials is the homogeneous solution to a linear difference equation, the following difference equation will exist:

$$y(n) = -\sum_{i=1}^{M} p_i y(n-i) \tag{4.15}$$

Therefore, with $2M$ samples, the coefficients p_i are calculated by solving the following system:

$$\begin{bmatrix} y(M) & y(M-1) & \cdots & y(1) \\ y(M+1) & y(M) & \cdots & y(2) \\ \vdots & \vdots & \vdots & \vdots \\ y(2M-1) & y(2M-2) & \cdots & y(M) \end{bmatrix} \begin{bmatrix} p_1 \\ p_2 \\ \vdots \\ p_M \end{bmatrix} = - \begin{bmatrix} y(M+1) \\ y(M+2) \\ \vdots \\ y(2M) \end{bmatrix} \tag{4.16}$$

Once the coefficients are computed, the ith root of the polynomial can be determined by solving the equation (4.16). Finally, the complex amplitudes (R_i) are calculated via linear least squares:

$$\begin{bmatrix} z_1 & z_2 & \cdots & z_M \\ z_1^2 & z_2^2 & \cdots & z_M^2 \\ \vdots & \vdots & \vdots & \vdots \\ z_1^M & z_2^M & \cdots & z_M^M \end{bmatrix} \begin{bmatrix} R_1 \\ R_2 \\ \vdots \\ R_M \end{bmatrix} = \begin{bmatrix} y(1) \\ y(2) \\ \vdots \\ y(M) \end{bmatrix} \tag{4.17}$$

The Prony's method is quite efficient and accurate for extracting the roots and reconstructing the signal $y(t)$; however, it is well known for its extreme sensitivity to noise. Moreover, The number of zeros is directly linked to the number of considered samples which involves two difficulties: the choice of M and solving a high size system.

Root-MUSIC

The idea of MUSIC was developed in [83] to estimate the signal frequencies. The signal model is expressed as follows:

$$x(k) = \sum_{i=1}^{M} A_i e^{j\omega_i k} + n(k) \tag{4.18}$$

where $A_i \in C$ is a complex number representing the magnitude and phase of the ith frequency component and $n(k)$ represents the noise.

From the available N data samples, the discret autocorrelation sequence $r_x[k]$ is computed:

$$R_x = E[xx^H] = \begin{bmatrix} r_x(0) & \cdots & r_x(N-1) \\ \vdots & \ddots & \vdots \\ r_x(N-1) & \cdots & r_x(0) \end{bmatrix} \tag{4.19}$$

where E and H are the expectation and the conjugate-transpose operators, respectively.

After that, The autocorrelation matrix R_x is eigendecomposed as:

$$R_x = U\Lambda_x U^H \tag{4.20}$$

where $U = [u_1, u_2, \ldots, u_N]$. All eigenvalues can be partitioned as follows:

$$\underbrace{\lambda_1 \geq \lambda_2 \geq \ldots \lambda_M}_{M\ signal\ eigenvalues} \geq \underbrace{\lambda_{M+1} \geq \lambda_{K+2} \geq \ldots \lambda_N}_{N-M\ noise\ eigenvalues} \tag{4.21}$$

Next, we put $\widetilde{U} = [u_1, u_2, \ldots, u_M]$ and we form annihilating filters using $N - M$ noise eigenfilters:

$$\widetilde{U}_i(z) = \sum_{m=0}^{N-1} u_i(m) z^{-m}; \quad i = M+1, \ldots, N \tag{4.22}$$

where $u_i(0) = 1$, $z_i = e^{\pm j\omega_i T_s}$. Every eigenfilter has $N-1$ roots, M roots are common for all eigenfilters. Now the following expression can be defined:

$$D(z) = \sum_{i=M+1}^{N} [\widetilde{U}_i(z)][\widetilde{U}_i^*(1/z^*)] \tag{4.23}$$

The MUSIC spectrum can be obtained by evaluating $D(z)$ on the unit circle $(D(z)_{z=e^{j\omega T_s}} = D(e^{j\omega T_s}))$.

Using the property that $(z_i)_{1 \leq i \leq N}$ are the roots of (4.22), the equation (4.23) can be rewritten as:

$$\begin{aligned} D(z) &= \prod_{i=1}^{M} (1 - z_i z^{-1})(1 - z_i^* z) \\ &\quad \cdot \prod_{i=M+1}^{N} (1 - z_i z^{-1})(1 - z_i^* z) \\ &= H_1(z) H_1^*(1/z^*) H_2(z) H_2^*(1/z^*) \end{aligned} \tag{4.24}$$

where $H_1(z)$ contains the M significant zeros of (4.22) whereas $H_2(z)$ contains the extraneous zeros which lie inside the unit circle. The root-MUSIC procedure uses the

most straightforward way to find the roots of $D(z)$ and to identify the frequencies of the signal components by using the knowledge that all those roots lie close to the unit circle.

ESPRIT

The original ESPRIT was described by Paulraj, Roy and Kailath [84].It is based on a naturally existing shift invariance between the discrete time series which leads to rotational invariance between the corresponding signal subspaces.

To illustrate the shift invariance, let's consider the single signal case without noise. Consider a vector of observations called X:

$$\begin{aligned} X &= [x(0), x(1), \ldots, x(N-1)] \\ &= A_1 \left[1, e^{j\omega_1 T_s}, e^{j\omega_1 2T_s}, \ldots, e^{j\omega_1 (N-1)T_s}\right] \end{aligned} \tag{4.25}$$

where $x(n)$ is represented by one exponential component as follows:

$$x(n) = A_1 e^{j\omega_1 n T_s} \tag{4.26}$$

The vector X can be partitioned as follows:

$$\begin{aligned} X &= [\underbrace{x(0), x(1), \ldots, x(N-2)}_{s_1}, x(N-1)] \\ &= [x(0), \underbrace{x(1), \ldots, x(N-2), x(N-1)}_{s_2}] \end{aligned} \tag{4.27}$$

We note that:

$$s_1 = e^{j\omega_1 T_s} s_2 \tag{4.28}$$

This approach can be extended to the multiple signal case where M exponential components are considered:

$$x(n) = \sum_{i=1}^{M} A_i e^{j\omega_i n T_s} \tag{4.29}$$

We compute the discret autocorrelation sequence $r_x(n)$ from the available N data samples. The autocorrelation matrix is arranged as follows:

$$R_x = E(xx^H) = \begin{bmatrix} r_x(0) & \cdots & r_x(N-1) \\ \vdots & \ddots & \vdots \\ r_x(N-1) & \cdots & r_x(0) \end{bmatrix} \tag{4.30}$$

Now we can eigen-decompose the matrix R_x as: $R_x = U\Lambda_x U^H$, where $U = [u_1, u_2, \ldots, u_N]$.

It is possible to partition a matrix by using special selector matrices which select the first and the last $(M-1)$ columns of a $(M \times M)$ matrix, respectively:

$$\begin{aligned} \Gamma_1 &= [I_{M-1}\ 0_{(M-1)\times 1}]_{(M-1)\times M} \\ \Gamma_2 &= [0_{(M-1)\times 1}\ I_{M-1}]_{(M-1)\times M} \end{aligned} \tag{4.31}$$

We use the selector matrices as follows:

$$\begin{aligned} S_1 &= \Gamma_1 \widetilde{U} \\ S_2 &= \Gamma_2 \widetilde{U} \end{aligned} \tag{4.32}$$

where $\widetilde{U} = [u_1, u_2, \ldots, u_M]$.

For the matrices defined in equation (4.32), for every i denoting the different frequency components, we have:

$$[\Gamma_1 \widetilde{U}]\Phi = \Gamma_2 \widetilde{U} \tag{4.33}$$

Where:

$$\Phi = \begin{bmatrix} e^{j\omega_1} & 0 & \cdots & 0 \\ 0 & e^{j\omega_2} & 0 & 0 \\ \vdots & \vdots & \ddots & \vdots \\ 0 & 0 & \cdots & e^{j\omega_k} \end{bmatrix} \tag{4.34}$$

The matrix Φ contains all information about frequency components. In order to extract this information, it is necessary to solve the equation (4.33) for Φ. By using

a unitary matrix (denoted as T), the following equations can be derived:

$$\begin{aligned} \Gamma_1(\widetilde{U}T)\Phi &= \Gamma_2(\widetilde{U}T) \\ \Gamma_1\widetilde{U}\underbrace{(T\Phi T^H)}_{eig.of\Phi} &= \Gamma_2\widetilde{U} \end{aligned} \tag{4.35}$$

In practice, the only interesting subspace is the signal subspace, spanned by signal eigenvectors U_s. Usually it is assumed that these eigenvectors correspond to the largest eigenvalues of the correlation matrix and ESPRIT algorithm determines the frequencies $e^{j\omega_k T_s}$ as the eigenvalues of the matrix Φ. In solving the rotational invariance formula of equation (4.33) we can use the Least-Squares (LS) solution, which is given by:

$$\Phi_{LS} = [\Gamma_1 U_s]^{-1}\Gamma_2 U_s \tag{4.36}$$

Knowing that both S_1 and S_2 contain errors, estimating Φ using the Total Least Squares (TLS) criterion is more appropriate. The TLS approach takes into account possible errors $(\Delta_{S_1}, \Delta_{S_2})$ for both estimated matrices S_1 and S_2. The TLS problem has the form:

$$(S_1 + \Delta_{S_1})\Phi = S_2 + \Delta_{S_2} \tag{4.37}$$

The TLS solution minimizes the Euclidean norm of the error matrix:

$$\|\Delta_{S_1}\Delta_{S_2}\| \tag{4.38}$$

The solution can be obtained using the singular value decomposition. Let V be the matrix of right singular vectors of the matrix $[S_1\ S_2]$. The matrix V can be partitioned into four square parts of equal size, as follows:

$$V = \begin{bmatrix} V_{11} & V_{12} \\ V_{21} & V_{22} \end{bmatrix} \tag{4.39}$$

Then the solution is given by:

$$\Phi_{TLS} = -V_{12}V_{22}^{-1} \tag{4.40}$$

Matrix Pencil Method

The matrix pencil method shows an improvement in terms of variance estimators compared to previous methods. A matrix pencil is a linear combination of two matrices Y_1 and Y_2, as in $Y_2 - \lambda Y_1$, in which λ is a scalar variable [4].

Theoretical backgrounds To explain the theory of MPM, we use as an example a temporal noisy signal $y(t)$ of a physical measurement, which has the following form:

$$y(t) = x(t) + n(t) \qquad 0 \leq t \leq T \tag{4.41}$$

Where:

- $y(t)$ = observed time response
- $x(t)$ = signal
- $n(t)$ = noise in the system

After sampling, the time variable, t, is replaced by kT_s, where T_s is the sampling period. Then, the signal $x(t)$ can be expressed as:

$$x(kT_s) = \sum_{i=1}^{M} R_i z_i^k \qquad k = 1, \ldots, N \tag{4.42}$$

and:

$$\begin{aligned} z_i^k &= e^{S_i T_s k} \\ &= e^{(\alpha_i + j\omega_i) T_s k} \end{aligned} \tag{4.43}$$

With:

- $S_i = \alpha_i + j\omega_i$
- R_i = residues or complex amplitudes

- α_i = damping factors
- ω_i = angular frequencies

Finally, the complete equation will have the following form:

$$\begin{aligned} y(kT_s) &= x(kT_s) + n(kT_s) \\ &\approx \sum_{i=1}^{M} R_i z_i^k + n(kT_s) \end{aligned} \tag{4.44}$$

In equation (4.44), the M complex values of z_i and the complex residues R_i are the unknowns that we need to estimate. The broad-band noise, $n(kT_s)$, is described by its statistical properties:

$$E\left\{n(kT_s)n^*((k-m)T_s)\right\} = \begin{cases} \sigma_n^2, & m = 0 \\ 0, & m \neq 0 \end{cases} \tag{4.45}$$

where $E(\cdot)$ is the expectation operator, $(*)$ is the complex conjugate and σ_n^2 is the variance. The signal-to-noise ratio is defined by:

$$SNR = 10\ log_{10}\left(\frac{Power(x)}{Power(n)}\right) dB \tag{4.46}$$

Given a set of sampled data $y(kT_s)$, the data is formed into a data matrix called a Hankel matrix. A Hankel matrix has the same value in each element along each anti-diagonal, as shown in Equations (4.47) and (4.48) where Y_1 and Y_2 are constructed by removing the last and first column respectively.

$$Y_1 = \begin{bmatrix} y(1) & y(2) & \cdots & y(L) \\ y(2) & y(3) & \cdots & y(L+1) \\ \vdots & \vdots & \cdots & \vdots \\ y(N-L) & y(N-L+1) & \cdots & y(N-1) \end{bmatrix}_{(N-L)\times L} \tag{4.47}$$

$$Y_2 = \begin{bmatrix} y(2) & y(3) & \cdots & y(L+1) \\ y(3) & y(4) & \cdots & y(L+2) \\ \vdots & \vdots & \cdots & \vdots \\ y(N-L+1) & y(N-L+2) & \cdots & y(N) \end{bmatrix}_{(N-L)\times L} \tag{4.48}$$

The matrix Y_2 is shifted by one sample in comparison to the matrix Y_1. The shape of the Hankel matrices is determined by the free-moving window length L, also known as the pencil parameter. The pencil parameter, L, is very useful in eliminating some effects of noise in the data. For best estimation results, it is shown that [85, 86]:

$$\frac{N}{3} \leq L \leq \frac{N}{2} \tag{4.49}$$

The data matrix Y_1 can be decomposed into three matrices, as:

$$Y_1 = Z_1 \cdot R \cdot Z_2 \tag{4.50}$$

where Z_1 and Z_2 are Vandermonde matrices as follows:

$$Z_1 = \begin{bmatrix} 1 & 1 & \cdots & 1 \\ z_1 & z_2 & \cdots & z_M \\ \vdots & \vdots & \cdots & \vdots \\ z_1^{N-L-1} & z_2^{N-L-1} & \cdots & z_M^{N-L-1} \end{bmatrix}_{(N-L)\times M} \tag{4.51}$$

$$Z_2 = \begin{bmatrix} 1 & z_1 & \cdots & z_1^{L-1} \\ 1 & z_2 & \cdots & z_2^{L-1} \\ \vdots & \vdots & \cdots & \vdots \\ 1 & z_M & \cdots & z_M^{L-1} \end{bmatrix}_{M\times L} \tag{4.52}$$

and:

$$R = \begin{bmatrix} R_1 & 0 & \cdots & 0 \\ 0 & R_2 & \cdots & 0 \\ \vdots & \vdots & \cdots & \vdots \\ 0 & 0 & \cdots & R_M \end{bmatrix}_{M\times M} \tag{4.53}$$

The values R_i found on the main diagonal of R are the residues of the signal model in equation (4.42). In a similar manner, Y_2 can be decomposed as:

$$Y_2 = Z_1 \cdot R \cdot Z_0 \cdot Z_2 \tag{4.54}$$

where Z_1, Z_2 and R are as defined in equations (4.51), (4.52) and (4.53), respectively, and:

$$Z_0 = \begin{bmatrix} z_1 & 0 & \cdots & 0 \\ 0 & z_2 & \cdots & 0 \\ \vdots & \vdots & \cdots & \vdots \\ 0 & 0 & \cdots & z_M \end{bmatrix}_{M \times M} \tag{4.55}$$

Using equations (4.50) and (4.54), the matrix pencil $Y_2 - \lambda Y_1$ can be rewritten as:

$$\begin{aligned} Y_2 - \lambda Y_1 &= Z_1 \cdot R \cdot Z_0 \cdot Z_2 - \lambda Z_1 \cdot R \cdot Z_2 \\ &= Z_1 \cdot R \cdot [Z_0 - \lambda I] \cdot Z_2 \end{aligned} \tag{4.56}$$

where I is the $(M \times M)$ identity matrix. The rank of the matrix pencil $Y_2 - \lambda Y_1$ is M, provided that $M \leq L \leq N - M$, for an arbitrary value of λ [4]. However, if $\lambda = z_i$, $i = 1, \ldots, M$, a row of $[Z_0 - \lambda I]$ goes to zero, and the rank of the matrix pencil is reduced by one. Hence, the parameters z_i may be found by constructing the following eigenvalue problem:

$$det\left\{Y_2 - \lambda Y_1\right\} = 0 \tag{4.57}$$

or:

$$det\left\{Y_1^{+} Y_2 - \lambda I\right\} = 0 \tag{4.58}$$

where Y_1^{+} is the Moore-Penrose pseudoinverse of Y_1. This, in turn, is defined as:

$$Y_1^{+} = (Y_1^{H} \cdot Y_1)^{-1} \cdot Y_1^{H} \tag{4.59}$$

where the superscript H denotes the conjugate transpose.

In the presence of noise, some prefiltering needs to be done. To avoid noise, the total-least-squares Matrix Pencil has been found to be superior [85, 86]. With the two matrices Y_1 and Y_2 from the noise-contaminated data $y(t)$, we construct the data matrix Y as follows:

$$Y = \begin{bmatrix} y(1) & y(2) & \cdots & y(L+1) \\ y(2) & y(3) & \cdots & y(L+2) \\ \vdots & \vdots & \cdots & \vdots \\ y(N-L) & y(N-L+1) & \cdots & y(N) \end{bmatrix}_{(N-L)\times(L+1)} \tag{4.60}$$

Note that Y_1 is obtained from Y by deleting the last column, and Y_2 is obtained from Y by deleting the first column. The next step is to apply the singular value decomposition of this matrix in order to separate the signal from noise.

Singular value decomposition of the data matrix Computing the eigenvalues and eigenvectors of a matrix is one of the most important problems in linear numerical analysis. The decomposition of a matrix in singular values is more robust from a numerical point of view and more used in practice than other decompositions like Jordan or Smith. The decomposition in singular values of a matrix $Y \in R^{(N-L)\times(L+1)}$ is as follows:

$$Y = U\Sigma V^H \tag{4.61}$$

Where U of dimensions $(N-L)\times(N-L)$ and V of dimensions $(L+1)\times(L+1)$ are unitary matrices of eigenvectors, while Σ of dimension $(N-L)\times(L+1)$ is a diagonal matrix of singular values σ_i. These matrices are such that:

$$\begin{aligned} UU^H &= I \\ VV^H &= I \end{aligned} \tag{4.62}$$

$$\Sigma = diag\left\{\sigma_1, \sigma_2, \ldots, \sigma_h\right\}, \quad with\ h = min\left\{N-L, L+1\right\} \tag{4.63}$$

With:

$$\sigma_1 \geq \sigma_2 \geq \ldots \geq \sigma_M \geq \sigma_{M+1} \geq \ldots \geq \sigma_h \tag{4.64}$$

The parameter M is very important to separate the signal from the noise. It should be estimated by the ratio of singular values to the largest one:

$$\frac{\sigma_M}{\sigma_1} \approx 10^{-p} \tag{4.65}$$

where p is the number of significant decimal digits in the data.

The decomposition in singular values of the matrix Y given in equation (4.61) will allow to give the expressions of the decomposition of the matrices Y_1 and Y_2 given in equations (4.47) and (4.48) as follows:

$$Y_1 = U\Sigma V_1^H \tag{4.66}$$

$$Y_2 = U\Sigma V_2^H \tag{4.67}$$

V_1 is obtained by deleting the last row of V, and V_2 is obtained by deleting the first row of V. Let's M be the number of significant singular values, we construct the matrices U, V_1, V_2 and Σ by keeping only the useful part:

$$\begin{aligned} U^M &= U(1:N-L, 1:M) \\ V_1^M &= V_1(1:L, 1:M) \\ V_2^M &= V_2(2:L+1, 1:M) \\ \Sigma^M &= \Sigma(1:M, 1:M) \end{aligned} \tag{4.68}$$

By using the equations (4.66) and (4.67), the equation (4.57) will become:

$$det\left\{U^M \Sigma^M V_2^{MT} - \lambda U^M \Sigma^M V_1^{MT}\right\} = 0 \tag{4.69}$$

which is equivalent to:

$$det\left\{V_2^{MT} - \lambda V_1^{MT}\right\} = 0 \tag{4.70}$$

The eigenvalue of lower matrix rank $\left\{V_2^{MT} - \lambda V_1^{MT}\right\}$ provides the estimation of z_i. Once the z_i are known, the residues R_i are solved by using the following least square

equation:

$$\begin{bmatrix} y(1) \\ y(2) \\ \vdots \\ y(N) \end{bmatrix} = \begin{bmatrix} 1 & 1 & \cdots & 1 \\ z_1 & z_2 & \cdots & z_M \\ \vdots & \vdots & \vdots & \vdots \\ z_1^{N-1} & z_2^{N-1} & \cdots & z_M^{N-1} \end{bmatrix} \begin{bmatrix} R_1 \\ R_2 \\ \vdots \\ R_M \end{bmatrix} \tag{4.71}$$

Model accuracy Let $\hat{x}(kT_s)$ be the reconstructed signal by using the estimated parameters by Matrix Pencil. In order to estimate the model accuracy, the following expressions can be used:

- Comparison between the reconstructed signal and the corrupted signal using the mean-square error:

$$C_1 = \frac{1}{N} \sum_k |y(kT_s) - \hat{x}(kT_s)|^2 \tag{4.72}$$

  or the signal-to-residue ratio in dB:

$$C_2 = 10\ log_{10} \frac{\sum_k |y(kT_s)|^2}{\sum_k |y(kT_s) - \hat{x}(kT_s)|^2} \tag{4.73}$$

- Comparison between the reconstructed signal and the noise-free signal using the mean-square error:

$$C_3 = \frac{1}{N} \sum_k |x(kT_s) - \hat{x}(kT_s)|^2 \tag{4.74}$$

  or the signal-to-residue ratio in dB:

$$C_4 = 10\ log_{10} \frac{\sum_k |x(kT_s)|^2}{\sum_k |x(kT_s) - \hat{x}(kT_s)|^2} \tag{4.75}$$

The functions C_3 and C_4 are suitable for simulation only, because they require knowledge of the uncorrupted signal $x(kT_s)$.

4.3 Classification methods

4.3.1 Introduction

A major aim of this thesis is to investigate the variation of classification performance with key parameters of the signal processing and feature extraction methods applicable to backscattered signals from UWB radar. The objective is not the assessment of novel classification algorithms. In the literature we can find many algorithms used for classification [87]. In this thesis, we have used the following classifiers: MDC, NB, k-NN and SVM. All these classification methods are applied to the processed data using the cross-validation, or leave-one-out, method so that the performance of each classifier is evaluated using a testing set independent from the training set, hence minimising the generalisation error.

Learning techniques are classified in two classes: supervised learning and unsupervised learning. In supervised learning, we assume that a set of training data is available, and the classifier will be designed by exploiting this a priori known information. In unsupervised learning, the training data, of known class labels, are not available. In this case, we are given a set of feature vectors and the goal is to partition this data set into subsets (clusters) so that data in each subset ideally share some common characteristics. In our work we want to classify specific objects, then we use the supervised learning. This process has two phases: Training phase and testing phase.

4.3.2 Cross Validation

Cross Validation is a statistical method of evaluating and comparing learning algorithms by dividing data into two segments: one used to learn or train a model and the other used to validate the model. The basic form of cross-validation is k-fold cross-validation. The data is first partitioned into k equally (or nearly equally) sized

segments or folds. Subsequently k iterations of training and validation are performed such that within each iteration a different fold of the data is used for validation while the remaining $k-1$ folds are used for learning. Empirical studies showed that 10 seems to be an optimal number of folds [88]. Data is commonly stratified before spliting them into k folds. Stratification is the process of rearranging the data as to ensure each fold is a good representative of the whole.

A special case of k-fold cross-validation named Leave-one-out cross-validation (LOOCV) can be used in the case where the size of the database is small. Using this method, we split the data set of size m into m partitions of size 1. Each partition is used for testing only once, whereas the remaining partitions are used for training.The estimation of the overall accuracy is calculated as an average of the individual accuracy measures

4.3.3 The Mahalanobis Distance Classifier

The Mahalanobis distance classifier uses statistics for each class. It assumes that the data for each class are normally distributed; thus, the samples, x_m $(m = 1, \ldots, K)$ of each class will form a cluster in K dimensional space, with a center given by the mean vector, A_m calculated by the expected value E of the mth entry in the vector x_m, and shape dependent on the covariance matrix, Σ. Estimates are formed for these parameters regarding each class, using the training vectors:

$$A_m = E[x_m] \tag{4.76}$$

$$\Sigma_m = E[(x_m - A_m)(x_m - A_m)^T] \tag{4.77}$$

where T denotes the transpose.

The mahalanobis distance calculates the distance between a given vector x and the mean vector A_m for a given class which is normalized by the variance Σ_m of training vectors in that direction. For a given class, m, the distance is calculated

by [89]:

$$\rho_m(x) = \sqrt{(x - A_m)^T \Sigma_m^{-1} (x - A_m)} \tag{4.78}$$

Classification is then performed by assigning a label to the given vector for which the Mahalanobis distance is minimized. This Mahalanobis distance classifier is simple to implement.

4.3.4 Naïve Bayes

Naïve Bayes is one of the most effective and efficient classification algorithm. It is easy to construct and to interpret. It is based around Bayes's theorem and makes the naïve assumption that the elements of an input feature vector are statistically independent. Despite this simplifying assumption the classifier achieves good results.

Let $x = (x_1, \ldots, x_N)$ be an N-dimensional instance which has no class label. Our goal is to build a classifier to predict its unknown class label. Let $C = (C_1, \ldots, C_K)$ be the set of the class labels. $P(C_k)$ is the prior probability of $C_k (k = 1, \ldots, K)$; $P(x/C_k)$ is the conditional probability of the evidence x if the hypothesis C_k is true. It is necessary to assess the class maximizing $P(C_k/x)$. The class C_k which maximizes $P(C_k/x)$ is called the maximum a posteriori hypothesis. By using Bayes's theorem, we obtain:

$$P(C_k/x) = \frac{P(x/C_k) \cdot P(C_k)}{P(x)} \tag{4.79}$$

A naïve Bayes classifier assumes that the value of a particular feature of a class is unrelated to the value of any other feature, so that:

$$P(x/C_k) = \prod_{j=1}^{N} P(x_j/C_k) \tag{4.80}$$

4.3.5 k-NN

k-Nearest Neighbors is based on the principle that the instances within a dataset will generally exist in close proximity to other instances having similar properties. The k-Nearest Neighbors algorithm is based on learning by analogy, that is, by comparing a given test example with training examples that are similar to it. The training examples are described by n attributes. Each example represents a point in an n-dimensional space. In this way, all of the training examples are stored in an n-dimensional pattern space. When given an unknown example, a k-nearest neighbors algorithm searches the pattern space for the k training examples that are closest to the unknown example. These k training examples are the k "nearest neighbors" of the unknown example. "Closeness" is defined in terms of a distance metric, such as the Euclidean distance.

The k-nearest neighbors algorithm is amongst the simplest of all classification algorithms: an example is classified by a majority vote of its neighbors, with the example being assigned to the class most common amongst its k nearest neighbors, k is a positive integer, typically small. If $k = 1$, then the example is simply assigned to the class of its nearest neighbor.

The basic k-Nearest Neighbors algorithm is composed of two steps: Find the k training examples that are closest to the unseen example. Take the most commonly occurring classification for these k examples. Usually the Euclidean distance criterion is used. A Euclidean distance between any pair $x_1 = (x_{1,1}, ..., x_{1,k})$ and $x_2 = (x_{2,1}, ..., x_{2,k})$ of instances is defined as:

$$d(x_1, x_2) = \sqrt{\sum_{j=1}^{k} (x_{1,j} - x_{2,j})^2} \tag{4.81}$$

Let $x = (x_1, \cdots, x_N)$ be an N-dimensional instance which has no class label. The

goal is to build a classifier to predict its unknown class label. Let $C = \{C_1, \cdots, C_K\}$ be the set of the class labels. The classification rule consists of the following steps:

- Among the N training points, search for the k neighbors closest to x using a distance measure. The parameter k is user-defined. Note that k should not be a multiple of K in order to make a decision. Hence, for two classes k should be an odd number.

- Out of the k-closest neighbors, identify the number k_j of the points that belong to class C_j. Obviously, $\sum_{j=1}^{K} k_j = k$.

- Assign x to class C_j, for which $k_j > k_n$, $j \neq n$. In other words, x is assigned to the class in which the majority of the k-closest neighbors belong.

4.3.6 Support Vector Machine

Introduction

The support vector machine is a classification method introduced in 1992 by Boser, Guyon, and Vapnik [90]. SVM maps the input vectors to a higher dimensional space where a maximal separating hyper plane is constructed [91]. Two parallel hyper planes are constructed on each side of the hyper plane separating the data. The maximum distance between the parallel planes is known as the margin. SVM maximizes the margin and thereby creates the largest possible distance between the separating hyper plane and the examples in the training set on either side of it.

Linearly separable classes

We work with the two-class linearly separable task in order to explain the method. Let $\vec{x_i}$, $i = 1, 2, \cdots, N$, be the feature vectors of the training set, X. These belong to either of two classes, C_1, C_2, which are assumed to be linearly separable. The goal,

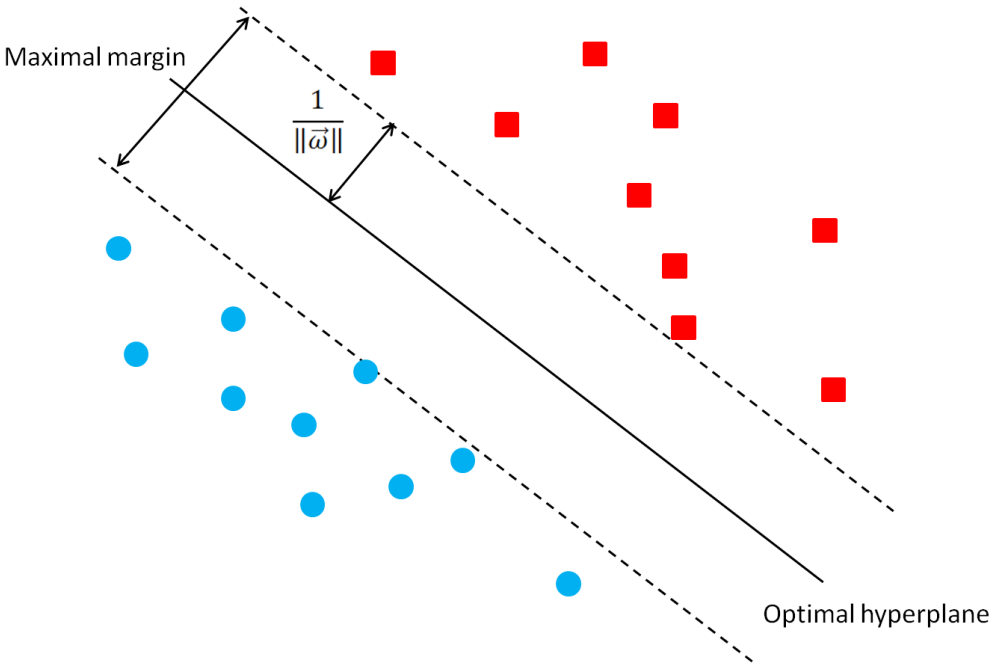

FIGURE 4.2: Optimal separating hyperplane in a two-dimensional space

is to design a hyperplane:

$$g(\vec{x}) = \vec{\omega} \cdot \vec{x} + \omega_0 = 0 \tag{4.82}$$

that classifies correctly all the training vectors. $\vec{\omega}$ is known as the weight vector, and ω_0 is called the bias. Such a hyperplane is not unique. The algorithm may converge to any one of the possible solutions. The very sensible choice for the hyperplane classifier would be the one that leaves the maximum margin from both classes (Figure 4.2).

The margin is the region between the two parallel hyperplanes:

$$\vec{\omega} \cdot \vec{x} + \omega_0 = 1 \tag{4.83}$$

and

$$\vec{\omega} \cdot \vec{x} + \omega_0 = -1 \tag{4.84}$$

The distance of a point from a hyperplane is given by:

$$z = \frac{\left|g(\vec{x})\right|}{\left\|\vec{\omega}\right\|} \tag{4.85}$$

We can scale $\vec{\omega}$, ω_0 so that the value of $g(\vec{x})$ at the nearest points in C_1, C_2, is equal to 1 for C_1 and, thus, equal to -1 for C_2. This is equivalent with:

- Having a margin of $\frac{2}{\left\|\vec{\omega}\right\|}$
- Requiring that

$$\vec{\omega} \cdot \vec{x} + \omega_0 \geq 1, \forall\ \vec{x} \in C_1 \tag{4.86}$$

$$\vec{\omega} \cdot \vec{x} + \omega_0 \leq -1, \forall\ \vec{x} \in C_2 \tag{4.87}$$

For each x_i, we denote the corresponding class indicator by y_i ($+1$ for C_1, -1 for C_2). Our task can now be summarized as: Compute the parameters $\vec{\omega}$, ω_0 of the hyperplane so that to:

$$minimize\ J(\vec{\omega}, \omega_0) \equiv \frac{1}{2}\left\|\vec{\omega}\right\|^2 \tag{4.88}$$

$$subject\ to\ y_i(\vec{\omega} \cdot \vec{x} + \omega_0) \geq 1, \quad i = 1, 2, \cdots, N \tag{4.89}$$

This is a classic nonlinear optimization problem with inequality constraints. Such an optimization problem is solved by using the lagrange function:

$$L(\vec{\omega}, \omega_0, \vec{\lambda}) = \frac{1}{2}\left\|\vec{\omega}\right\|^2 - \sum_{i=1}^{N} \lambda_i [y_i(\vec{\omega} \cdot \vec{x_i} + \omega_0) - 1] \tag{4.90}$$

where the λ_i are Lagrange multipliers.

The KarushKuhnTucker conditions are used to minimize (4.88), (4.89) as follows:

$$\frac{\partial}{\partial \omega} L(\vec{\omega}, \omega_0, \vec{\lambda}) = 0 \tag{4.91}$$

$$\frac{\partial}{\partial \omega_0} L(\vec{\omega}, \omega_0, \vec{\lambda}) = 0 \tag{4.92}$$

$$\lambda_i \geq 0, \qquad i = 1, 2, \cdots, N \tag{4.93}$$

$$\lambda_i [y_i (\vec{\omega} \cdot \vec{x_i} + \omega_0) - 1] = 0, \qquad i = 1, 2, \cdots, N \tag{4.94}$$

where $\vec{\lambda}$ is the vector of the Lagrange multipliers λ_i.
Combining 4.90 with 4.91 and 4.92 results in:

$$\vec{\omega} = \sum_{i=1}^{N} \lambda_i y_i \, \vec{x_i} \tag{4.95}$$

$$\sum_{i=1}^{N} \lambda_i y_i = 0 \tag{4.96}$$

To compute the involved parameters, the problem can be stated equivalently by its Wolfe dual representation form, to finally obtain:

$$max_{\lambda} (\sum_{i=1}^{N} \lambda_i - \frac{1}{2} \sum_{i,j} \lambda_i \lambda_j y_i y_j \, \vec{x_i} \cdot \vec{x_j}) \tag{4.97}$$

$$subject\ to \ \sum_{i=1}^{N} \lambda_i y_i = 0 \tag{4.98}$$

$$\lambda_i \geq 0 \tag{4.99}$$

If $\lambda_i = 0$, then x_i is not used in decision rule and can be discarded. Points x_i such that $\lambda_i \neq 0$ lie on the margin and are called support vectors. They determine the decision boundary.

Nonlinearly separable classes

When the classes are nonlinearly separable, the previous method can be applied but some points will be misclassified. The main idea is that those points that lie on

the wrong side of the hyperplane are explicitly penalized by introducing variables, ξ, that control how far on the wrong side of a hyperplane a point lies. The optimization problem becomes:

$$minimize\ \frac{1}{2}\left\|\vec{\omega}\right\|^2 + C\sum_{i=1}^{N}\xi_i \tag{4.100}$$

subject to:

$$y_i(\vec{\omega}\cdot\vec{x}\ +\omega_0) \geq 1-\xi_i,\ \xi_i \geq 0,\ i=1,2,\cdots,N \tag{4.101}$$

where, C is the penalty parameter of the error term.

The dual then becomes:

$$max_\lambda(\sum_{i=1}^{N}\lambda_i - \frac{1}{2}\sum_{i,j}\lambda_i\lambda_j y_i y_j\ \vec{x_i}\cdot\vec{x_j}) \tag{4.102}$$

$$subject\ to\ 0 \leq \lambda_i \leq C,\quad i=1,2,...,N \tag{4.103}$$

$$\sum_{i=1}^{N}\lambda_i y_i = 0 \tag{4.104}$$

There are no general methods for choosing parameters ω_0 and b in a non-separable case. The parameters are usually found by optimizing some performance measure on a training set.

For a more complex problem, using a kernel function is necessary.The main idea behind using a kernel function is to map the data into a different space and to construct a linear classifier in this space.

Given an appropriate mapping ϕ: $x \to \phi(x)$, we can put:

$$K(x,z) = \langle\phi(x),\phi(z)\rangle \tag{4.105}$$

where $x, z \in \mathbb{R}^n$, $\phi \in \mathbb{R}^m$ with $m \geq n$ and $\langle\cdot,\cdot\rangle$ denotes the inner product operation. Such functions K are called kernel functions.

Some examples of kernels include:

- polynomial kernels:

$$K(x,z) = (x^T z + 1)^q, \quad q > 0 \tag{4.106}$$

- Radial Basis Functions:

$$K(x,z) = e^{-\frac{\|x-z\|^2}{2\sigma^2}} \tag{4.107}$$

- Hyperbolic Tangent:

$$K(x,z) = tanh(\beta x^T z + \gamma) \tag{4.108}$$

Once an appropriate kernel has been adopted, the Wolfe dual optimization task becomes:

$$max_\lambda(\sum_{i=1}^{N} \lambda_i - \frac{1}{2}\sum_{i,j} \lambda_i \lambda_j y_i y_j K(x_i, x_j)) \tag{4.109}$$

$$subject\ to\ 0 \leq \lambda_i \leq C, \quad i = 1, 2, ..., N \tag{4.110}$$

$$\sum_{i=1}^{N} \lambda_i y_i = 0 \tag{4.111}$$

A major limitation of the support vector machines is that up to now there has been no efficient practical method for selecting the best kernel function. Once a kernel function has been adopted, the so-called kernel parameters (e.g., σ for the Radial Basis Function kernel) aswell as the smoothing parameter,C,in the cost function are selected so that the error performance of the resulting classifier can be optimized. In our work we implement the radial basis function kernel.

The standard theory of SVM supports only binary classification problems. However, in our work we deal with classifying objects into more than two classes. The most popular technique for multiclass classification using binary support vector machines is called one-versus-the-rest classification [92].

In the one-versus-the-rest technique, given M classes, we construct M binary, support vectorbased decision surfaces, say: $g^1, ..., g^m$. Each decision surface is trained to separate one class from the rest. Therefore, the decision surface g^1 is trained to separate the class labeled 1 from all other classes, the decision surface g^2 is trained to separate the class labeled 2 from all other classes, and so on. To classify an unknown point we use a voting scheme based on which of the M decision surfaces returns the largest value for this unknown point. We then use the decision surface that returns the largest value for the unknown point to assign this point to a class.

4.4 Conclusion

In this chapter, wavelet transform and high resolution methods which are used for feature extraction have been presented. Wavelet transform is applied on the temporal signal in the next chapter but high resolution methods can be applied on the temporal or frequency signal. Four methods of supervised classification have been provided: MDC, NB, k-NN and SVM. We gave more detail in the explanation of SVM because the best results of classification accuracy are obtained with this method. However, SVM is considered as black box in comparison to other methods of classification because of the difficulty to understand the process of classifying. k-NN calculates the distance to all training vectors that are stored in the database, but MDC calculates the distance to only a given class which is represented by its mean and covariance matrix. In the next chapter, we present the results obtained by simulations and experiments.

5

Simulation and experimental results

5.1 Introduction

In this chapter, we present simulation and experimental results found in this work. Firstly, we present the simulation results of backscattered fields from canonical objects. Next, we show the results obtained by the comparison between the different methods of feature extraction. After that, we present the results obtained by the comparison between the different methods of classification. Then, we propose a powerful method for radar UWB automatic target classification in white Gaussian noise and different aspect angles between the radar and the target. Finally, we present the experimental results.

5.2 Simulation results of backscattered fields from canonical objects

In this section, we present the software tool and the simulation parameters used to compute the free-space backscattered fields from canonical objects. An electromagnetic commercial tool called FEKO [93], which is used by the laboratory, has been used to compute the different backscattered fields of canonical objects.

5.2.1 Presentation of FEKO and the simulation parameters

FEKO is a suite of tools that is used for electromagnetic field analysis of 3D structures. FEKO simulations are based on the Method of Moments (MoM). Other techniques such as MultiLevel Fast Multipole Method (MLFMM), Finite Element Method (FEM), Uniform Theory of Diffraction (UTD), Geometrical optics (ray launching) and Physical Optics (PO) have been implemented to allow the solving of electrically large problems and inhomogeneous dielectric bodies of arbitrary shape. Electromagnetic fields are obtained by calculating the electric surface currents on the conducting surfaces.

The choice of the method depends on the application case. Quasi-exact methods such as MOM or FEM are adapted for electrically small objects. But, they become inappropriate for electrically large objects. In this case, the processing requirements increase rapidly. Then, it is better to use approximated methods such as PO or UTD, which provide a compromise between the simulation time and the accuracy. Note that all these methods are solved in the frequency domain.

To illustrate the calculated fields with FEKO, we use three perfectly electric conducting objects: thin wire (length = 3 m and radius= 0.0025 m), sphere (radius = 0.3 m), and cylinder (length = 0.6 m and radius = 0.2 m). A plane wave excitation with normal incidence is used (figure 5.1).

5.2.2 The signals in time domain

We use TIME-FEKO to compute the free-space backscattered fields of the three objects. With the TIME-FEKO program, electromagnetic fields are given in the time domain. It is based on the FEKO program that does the relevant calculations in the frequency domain and an IFFT algorithm that transforms the data to the time domain. A Gaussian pulse is applied as an excitation plane wave. In the time

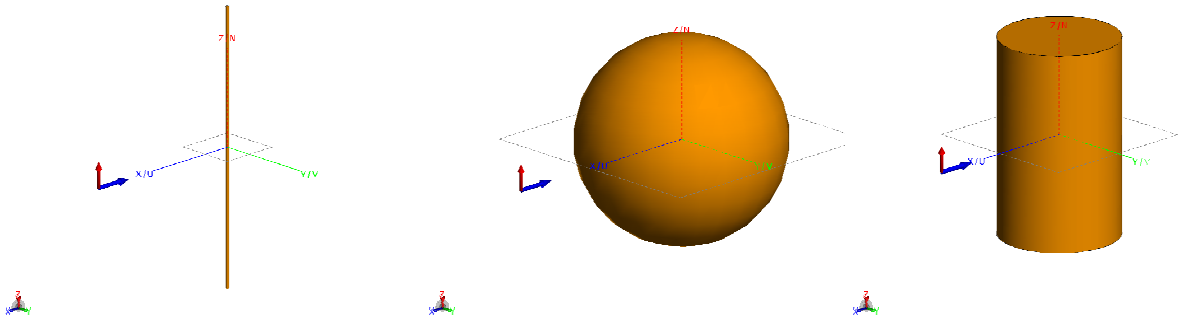

(a) Thin wire (b) Sphere (c) Cylinder

FIGURE 5.1: Example of the three canonical objects

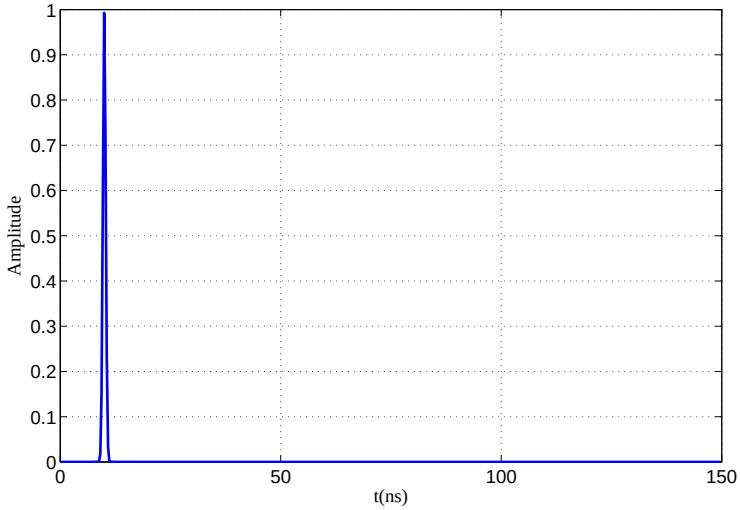

FIGURE 5.2: Gaussian pulse time

domain, the expression of the Gaussian pulse waveform is given by:

$$g(t) = Ae^{-(\frac{t-t_0}{\sigma})^2} \tag{5.1}$$

where A stands for the amplitude and σ for the width of the Gaussian pulse. In our simulations we have set $A = 1$, $t_0 = 10$ ns, and $\sigma = 0.454\ ns$ (Figure 5.2).

σ is chosen such that the upper frequency:

$$f_{max} \approx \frac{4}{\pi\sigma}\sqrt{\ln(\sqrt{2})} \approx 1.7\ GHz \tag{5.2}$$

This frequency is chosen by making a compromise between the calculation time and having the radiation of the targets in resonance and optical regions. The number of frequency samples is chosen to be at 256. The backscattered field is given in the time domain without considering the factor e^{-jkR}/R.

Figure 5.3 shows the backscattered fields form the three canonical objects in the time domain. We can see from the figures that the wire is very resonant in comparison to the sphere and the cylinder. Therefore, the contribution of the late time is very small for the sphere and the cylinder which are considered as less resonant objects.

5.2.3 The signals in Frequency domain

The signals in frequency domain can be obtained directly from the FEKO software, or they can be obtained from the time domain signals. To obtain the frequency response from the temporal signal, we first need to transform it by means of the fast Fourier transformed (FFT) technique and then dividing it by the FFT of the Gaussian incident pulse. Figure 5.4 shows the backscattered fields from the three canonical objects in the frequency domain. The real and imaginary parts of the signals are presented.

5.3 Feature extraction results

5.3.1 Comparison between analytical and measured CNRs

In this subsection, the CNRs of thin wire extracted by high resolution methods are compared to the CNRs calculated analytically. The high resolution methods used in this comparison are: Root-MUSIC, LS-ESPRIT, TLS-ESPRIT and Matrix Pencil Method. The comparison is made in terms of pole-position in the s-plane.

Figure 5.5 shows the backscattered noiseless signals in time domain from thin

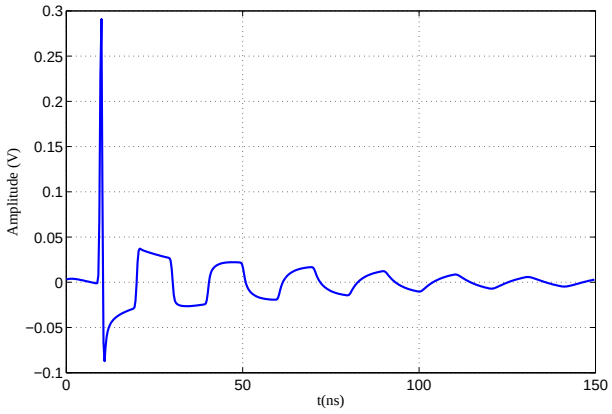

(a) Thin wire

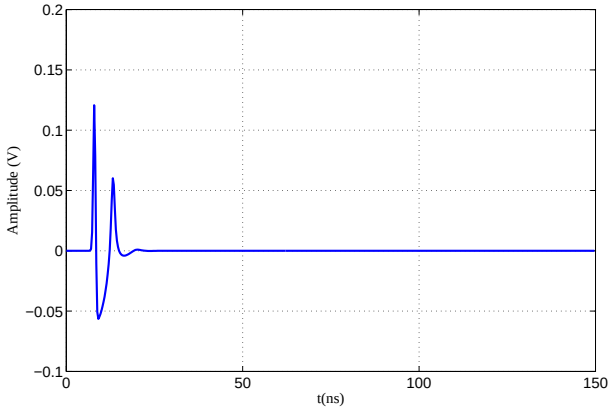

(b) Sphere

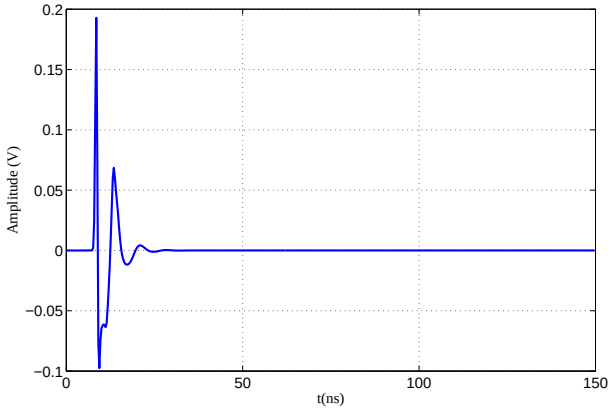

(c) Cylinder

FIGURE 5.3: The backscattered fields form the three canonical objects in the time domain

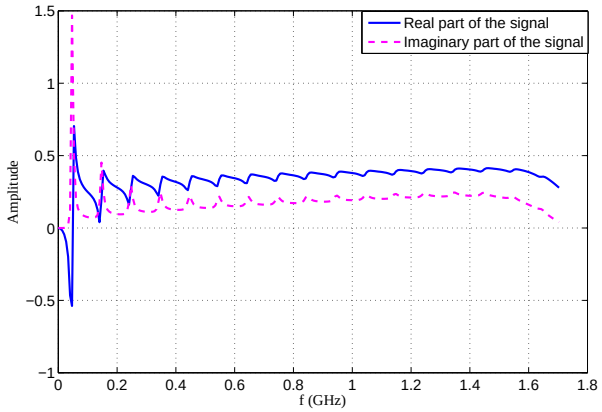

(a) Thin wire

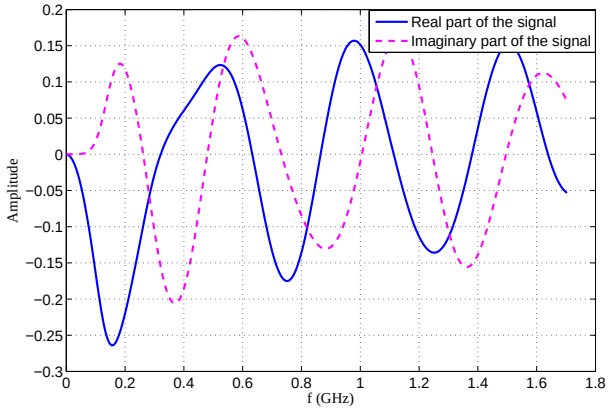

(b) Sphere

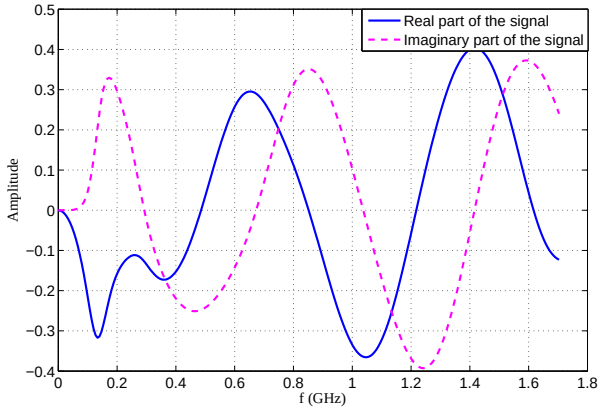

(c) Cylinder

FIGURE 5.4: The backscattered fields from the three canonical objects in the frequency domain

wire (a/L = 0.005) with three different incident angles $\theta_i = 50, 90$ and $150°$.

In order to find the start of the late time, the following expression can be applied [94]:

$$T_L = T_b + 2T_{tr} + T_p \tag{5.3}$$

where T_b is the time when incident wave strikes the leading edge of the target, T_{tr} is the maximum transit time of the target, and T_p is the pulse width of the transmitted waveform.

Figure 5.6 shows the normalized CNRs extracted by the four high resolution methods compared to the analytical CNRs given by Teshe (subsection 2.5.2), with the three incident angles. Analysis of the incident angles of 50° and 150° shows that the measured CNRs by the four methods fit well with the analytical CNRs. All the CNRs are well estimated except the last one. However with the incident angle of 90°, we can see that not all the CNRs are extracted. CNRs are known to be independent of the aspect angle between the radar and the target, but with normal incidence, some CNRs of the wire are not extracted because the resonance phenomena of the wire are weak when the incidence is normal.

Figure 5.7 shows normalized CNRs location in the s-plane extracted with the four high resolution methods with incident angle of 150° and SNR = 50 and 30 dB. With SNR = 50 dB, all the angular frequencies are well estimated except one which is not well estimated by Root-MUSIC. The first seven damping factors are well estimated with SNR = 50 dB but the remaining are not well estimated. More the value of SNR decreases, more the estimated angular frequencies and damping factors are different from the analytical CNRs. With SNR = 30 dB, we can see that the two last angular frequencies and damping factors are not well estimated.

Although all the four high resolution methods performed well, in the remaining of the thesis we will use the Matrix Pencil Method. This choice is driven by the

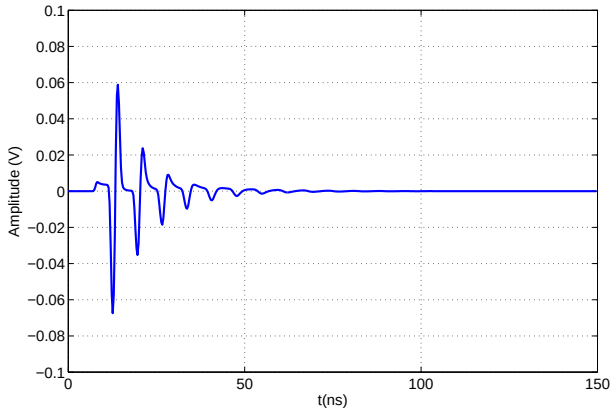

(a) Incident angle = 50°

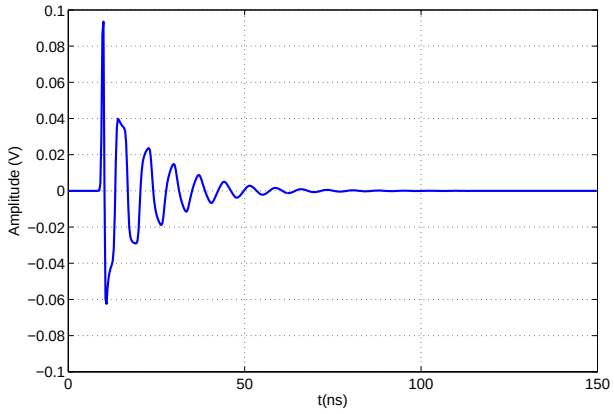

(b) Incident angle = 90°

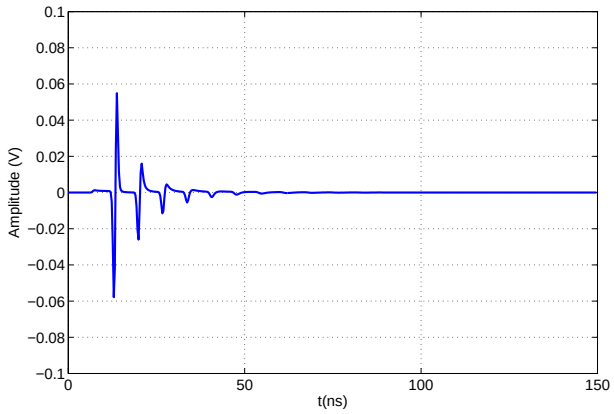

(c) Incident angle = 150°

FIGURE 5.5: The backscattered fields form thin wire (a/L = 0.005)

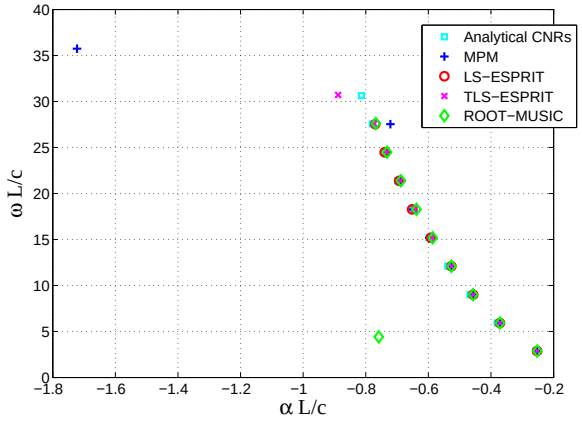

(a) Incident angle = 50°

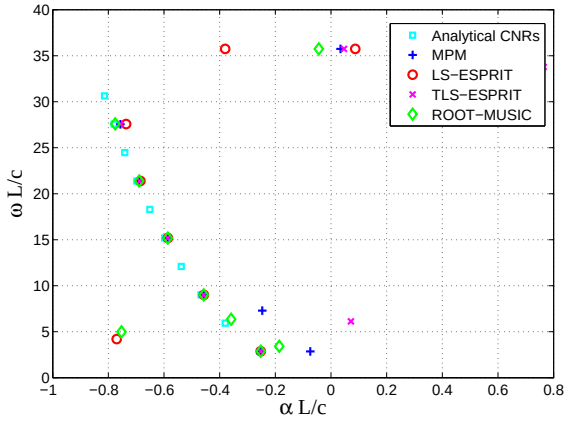

(b) Incident angle = 90°

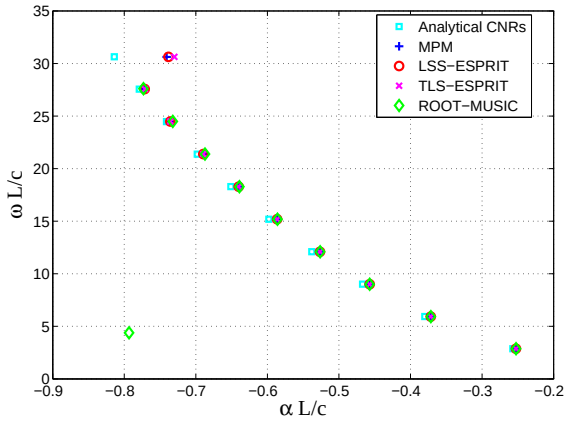

(c) Incident angle = 150°

FIGURE 5.6: Normalized CNRs location in the s-plane with different incident angles

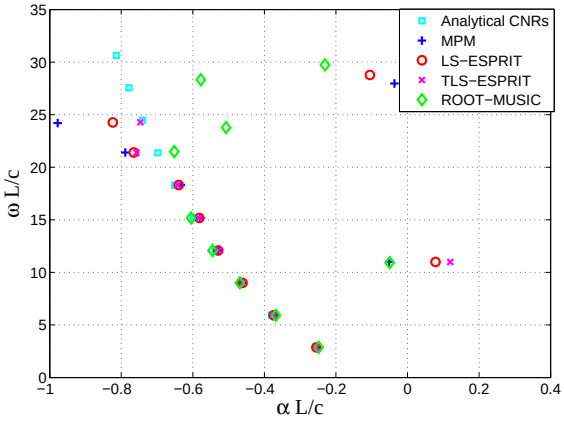

(a) SNR = 30 dB

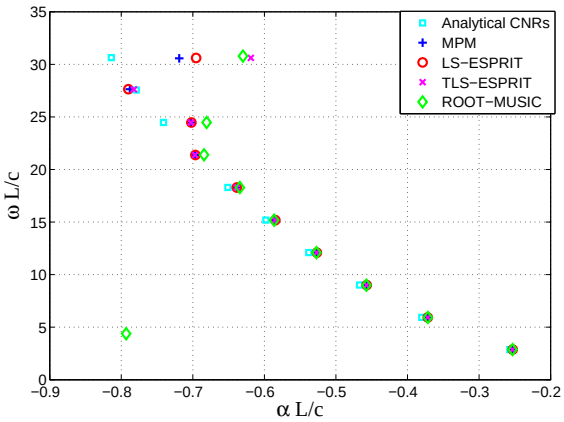

(b) SNR = 50 dB

FIGURE 5.7: Normalized CNRs location in the s-plane with different values of SNR

fact that MPM does not require estimation of an autocorrelation matrix which has an expensive computation. In addition, The Matrix Pencil approach has a lower variance of the estimates of the parameters of interest than the Prony's Method, and is also computationally more efficient and less sensitive to noise [4].

5.3.2 Matrix Pencil Method in Time Domain

In time domain we use the SEM presented in subsection 2.3.4. Simulations are conducted by using the targets presented in subsection 5.2.1: thin wire (length = 3m

Table 5.1: Features extracted by MPMTD from a thin wire (l = 3m), a sphere (r = 0.3 m), and a cylinder (l= 0.6 m, r= 0.2 m) (poles$\times$ 10^9)

	Thin wire	**Sphere**	**Cylinder**
$P_{1,2}$	$-0.080 \mp 3.409j$	$-1.859 \mp 4.502j$	$-1.313 \mp 5.250j$
$P_{3,4}$	$-0.053 \mp 2.791j$	$-1.401 \mp 1.729j$	$-1.248 \mp 3.858j$
$P_{5,6}$	$-0.044 \mp 2.166j$	$-0.438 \mp 0.843j$	$-0.520 \mp 1.690j$
$P_{7,8}$	$-0.038 \mp 1.541j$	0	$-0.339 \mp 0.849j$
$P_{9,10}$	$-0.031 \mp 0.917j$	0	0
$P_{11,12}$	$-0.018 \mp 0.297j$	0	0

and radius= 0.0025m), sphere (radius = 0.3m), and cylinder (length = 0.6 m and radius = 0.2 m). A plane wave excitation with normal incidence is used.

Table 5.1 shows the extracted features by MPMTD from a thin wire (l= 3m, r=0.0025 m), a sphere (r = 0.3 m), and a cylinder (l = 0.6m, r = 0.2 m). Features extracted by MPMTD are complex conjugates because the signal is real in time domain. We used the expression (5.3) to find the start of the late time.

In Figure 5.8, the reconstructed late time signal with MPMTD compared to the simulated one by Time-Feko of the three examples is depicted. The signal is well reconstructed by the MPMTD.

To use the expression (5.3), we need to know in advance the size of the target to calculate T_{tr}. This is inconvenient in the practical case, because we suppose that the size of the target is unknown for us.

Another method can be applied based on the use of a sliding window and observing the stability of the poles after moving the beginning of the window. By displacing the sliding window through the entire signal by small time steps and by applying MPMTD to the sampled data, we represent the positive imaginary part of the poles as a function of t_i (t_i is the beginning of the late time) in Figure 5.9. In Figure 5.9a

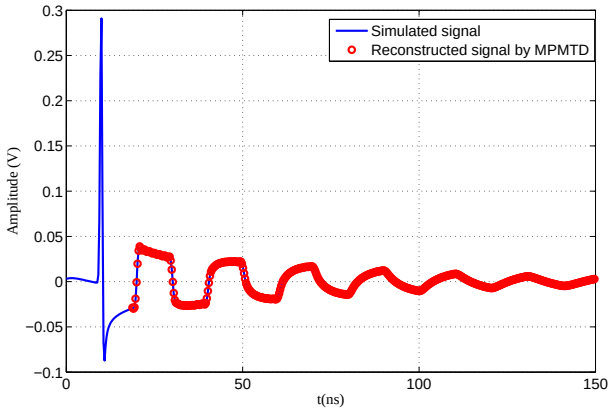

(a) Thin wire (length = 3m)

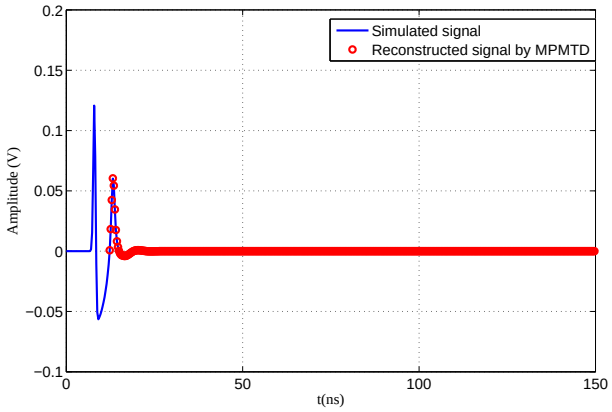

(b) Sphere (radius = 0.3 m)

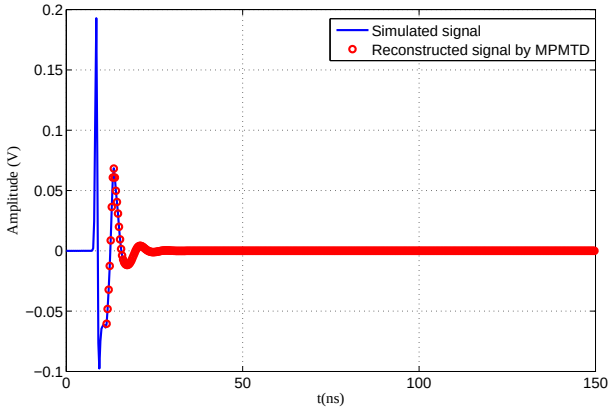

(c) Cylinder (length = 0.6m and radius = 0.2 m)

FIGURE 5.8: Simulated signal compared with reconstructed signal by MPMTD

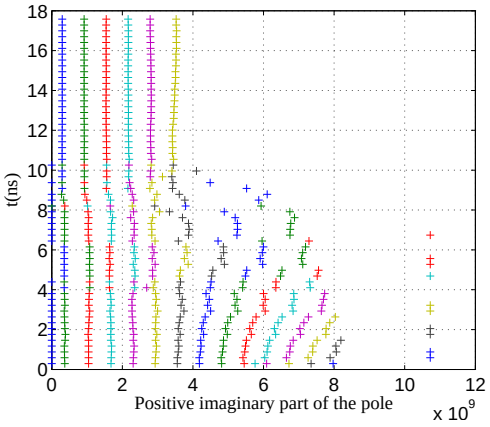

(a) Thin wire (length = 3m)

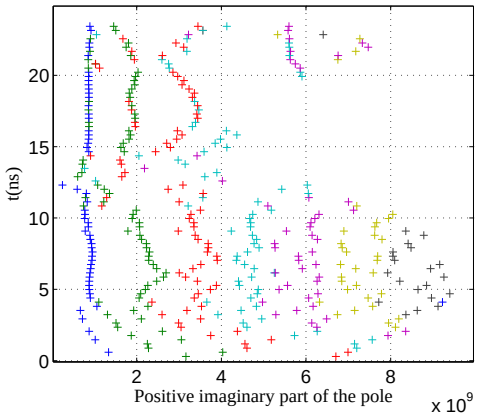

(b) Sphere (radius = 0.3 m)

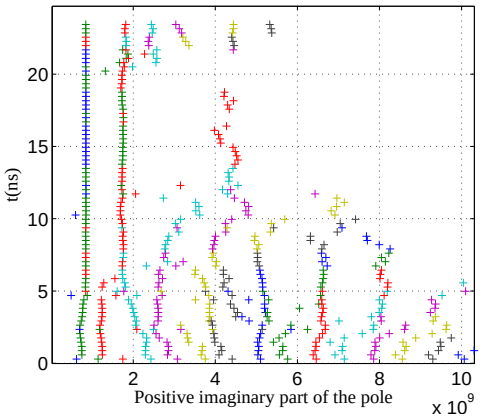

(c) Cylinder (length = 0.6 m and radius = 0.2 m)

FIGURE 5.9: Variation of positive imaginary part of the poles with sliding time

corresponding to the thin wire, we can see the 6 positive imaginary parts of the poles shown in Table 5.1 at around $t_i = 10\ ns$, which corresponds to the start of the late time.

The convergence to the natural resonances is stable in the thin wire when t_i is shifted in time (the stability is observed in the different wires that we have used), which is not the case for less resonant objects as the sphere and the cylinder. Only the first and second poles are stable (5.9b-5.9c). The instability of the convergence to the natural resonances is due to the small contribution of the late time part of the signal.

5.3.3 Matrix Pencil Method in Frequency Domain

Matrix Pencil Method in Frequency Domain (MPMFD) [95] is applied on the reduced complexity model presented in section 2.3.6.

Table 2, shows the extracted features with MPMFD from the same targets: the thin wire (l= 3m, r=0.0025 m), the sphere ($r = 0.3$ m) and the cylinder ($l = 0.6$m, $r = 0.2$ m). With the poles shown in Table 5.2, the real and imaginary parts of the signal have been reconstructed in Figure 5.10 for the three objects. The obtained results agree with the simulated signal.

In frequency domain, all the physical characteristics of the objects are taken into account. The real and imaginary parts of the signals are used to identify the objects.

In Figure 5.8 we can see the weak contribution of the late time signal in comparison to the contribution of the signal in the frequency domain which takes the early time into consideration (Figure 5.10). The late-time signature for most realistic targets is usually very weak and heavily corrupted by noise.

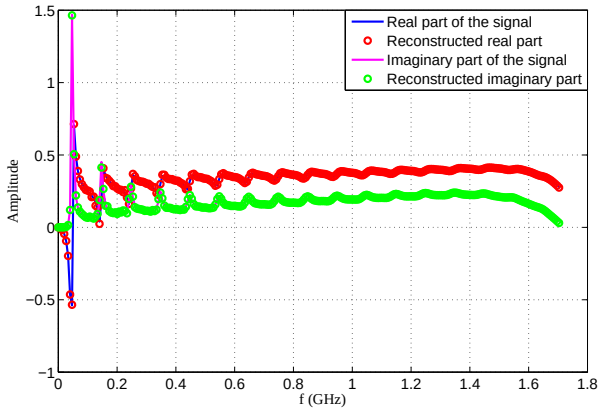

(a) Thin wire (length = 3m)

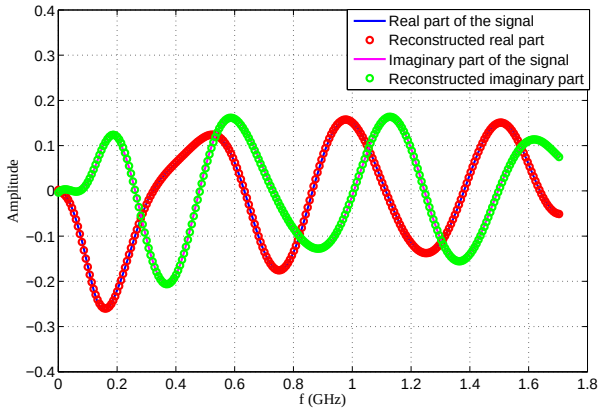

(b) Sphere (radius = 0.3 m)

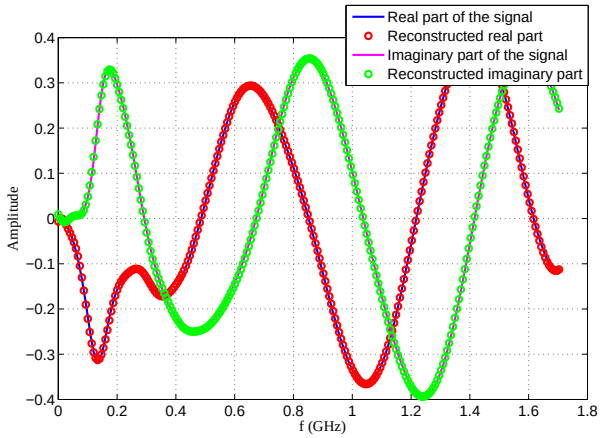

(c) Cylinder (length = 0.6m and radius = 0.2 m)

FIGURE 5.10: Simulated signal compared with reconstructed signal by MPMFD

Table 5.2: Features extracted by MPMFD from a thin wire (l = 3m), a sphere (r = 0.3 m), and a cylinder (l= 0.6 m, r= 0.2 m) (poles$\times$ 10^8)

	Thin wire	**Sphere**	**Cylinder**
P_1	$-5.096 - 43.80j$	$-0.600 - 2.970j$	$-0.642 - 3.443j$
P_2	$-4.678 - 33.57j$	$-0.150 - 2.046j$	$-0.184 - 1.994j$
P_3	$-2.278 - 24.07j$	$-1.013 - 1.108j$	$-0.584 - 1.122j$
P_4	$-1.169 - 19.47j$	$-0.740 + 0.884j$	$0.093 - 0.583j$
P_5	$-0.426 - 12.61j$	$-0.002 + 1.242j$	$0.039 + 0.793j$
P_6	$-10.80 - 7.60j$	0	$0.003 + 1.014j$
P_7	$-4.173 - 6.851j$	0	0
P_8	$-0.229 - 6.294j$	0	0
P_9	$0.021 - 0.002j$	0	0
P_{10}	$-0.292 + 0.534j$	0	0
P_{11}	$-3.656 + 28.76j$	0	0
P_{12}	$-4.743 + 39.70j$	0	0

5.4 Classification results

In this section, we present classification results of extracted features in time and frequency domains. The following classifiers are used: MDC, k-NN, NB and SVM. The accuracy of classification is expressed in terms of percentage of correctly identified objects. DWT and MPMTD are used as feature extraction methods in time domain and MPMFD is used in Frequency domain.

We have used the leave-one-out cross-validation because the database has a small size. By using this method, we split the data set of size m into m partitions of size 1. Each partition is used for testing only once, whereas the remaining partitions are used for training. The estimation of the overall accuracy is calculated as an average of the individual accuracy measures. In our work, we have used 8 examples of different sizes for each one of the 3 canonical targets, so: $m = 3 \times 8 = 24$.

In time domain, the feature extraction methods are applied to the late time part of the backscattered signal from UWB radar. We used the expression (5.3) to find the beginning of the late time. Three canonical objects are used to test the classifiers accuracy: thin wire, sphere and cylinder. To apply the MPMFD, we work with the frequency response, which can be obtained from the temporal response by transforming it to the frequency domain by means of the fast Fourier transformed technique and dividing it by the FFT of the Gaussian incident pulse.

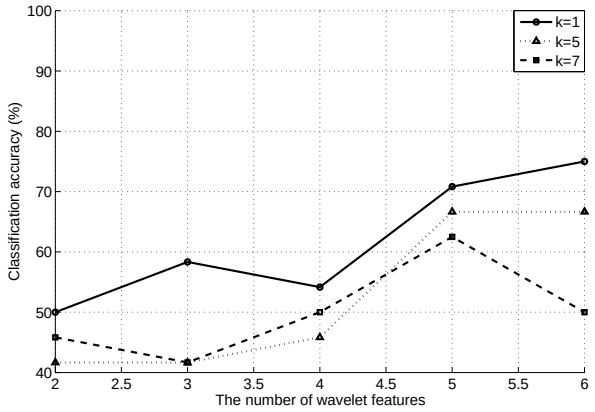

(a) Coif 5 wavelet

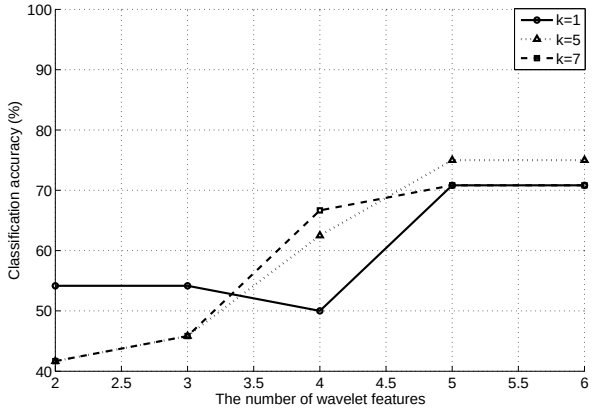

(b) db 4 wavelet

FIGURE 5.11: k-NN classification accuracy of wavelets

The database has been built by using 8 examples of different sizes for each per-

fectly electric conducting target: thin wire (length: l = 1, 1.3, 1.5, 1.7, 2, 2.4, 2.5 and 3 m, and radius: r = 0.0025 m for all the wires), sphere (radius: r = 0.15, 0.2, 0.28, 0.3, 0.35, 0.4, 0.45 and 0.5 m), and cylinder (l = 0.4 and r = 0.17 m, l= 0.4 and r = 0.23 m, l = 0.5 and r = 0.15 m, l = 0.5 and r = 0.25 m, l= 0.6 and r= 0.2 m, l = 0.7 and r= 0.1 m, l= 0.8 and r= 0.19 m, and l= 1 and r = 0.15 m).
Time-FEKO has been used to compute the free-space backscattered fields of the targets. The upper frequency is chosen to be $f_{max} = 1.7\ GHz$, This frequency is chosen by making a compromise between the calculation times and having the radiation of the targets in resonance and optical regions. The number of frequency samples is chosen to be at 256. The backscattered field is given in the time domain without considering the factor e^{-jkR}/R.

Two types of wavelets were used for feature extraction: coif 5 and db 4. Figure 5.11 shows the classification accuracy of the k-NN classifier for coif 5 wavelet (Figure 5.11a) and db4 wavelet (Figure 5.11b) as function of number of wavelet features. The energy terms of the equation (4.11) are the corresponding features and their number varies from two to six. As k should not be neither a multiple of three (the number of objects) nor an even number, we gave the following values to k: 1, 5 and 7. The best accuracy of k-NN classifier with wavelet features is 75 %. This accuracy is found by applying coif 5 wavelet with six wavelet features and $k = 1$, or by applying db 4 wavelet with five or six wavelet features and $k = 5$.

Figure 5.12 shows the classification accuracy of the four classifiers for coif 5 wavelet (Figure 5.12a) and db4 wavelet (Figure 5.12b) as function of number of wavelet features. The best accuracy is found to be 87.5 % and it is obtained with SVM by using coif 5 wavelet with five features, or by using db 4 wavelet with five and six features. The other classifiers: MDC, k-NN and NB have an accuracy between 70 and 80 % with five and six features for coif 5 and db4 wavelets. The best number of wavelet features is five for all the classifiers.

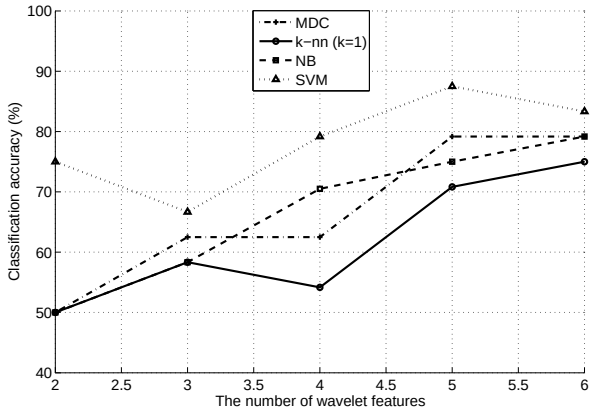

(a) Coif 5 wavelet

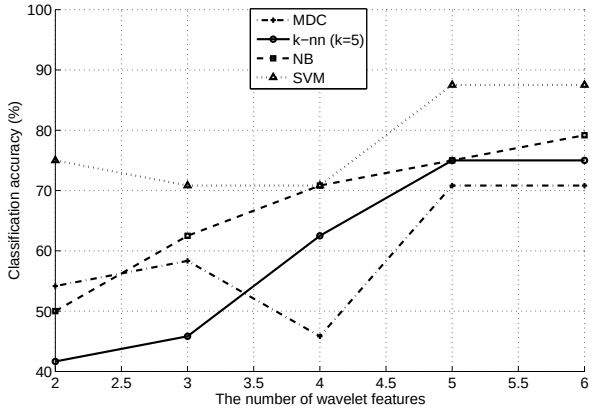

(b) db 4 wavelet

FIGURE 5.12: Classification accuracy of wavelets for MDC, k-NN, NB and SVM

Concerning the extracted features by MPMTD, the real and the positive imaginary parts of the extracted CNRs presented in table 5.1 are used for classification. But, for classification by using the extracted features by MPMFD, all real and imaginary parts of the features are used.

Table 5.3 shows the classification accuracy of the four classifiers. In time domain, MPMTD gives a good result with SVM, but it is less accurate when using the other classifiers. MPMTD gives better results than wavelet by using MDC, k-NN and SVM, but Wavelet is better than MPMTD with NB. The separation between early

Table 5.3: Classification accuracy of each object (%)

Classifiers	**MDC**	**NB**	k**-NN**			**SVM**
			$k=1$	$k=5$	$k=7$	
Wavelet db 4	70.83	79.17	70.83	75	70.83	87.5
MPMTD	83.33	75	83.33	79.17	50	91.67
MPMFD	100	100	100	91.67	87.5	100

and late time is the weakness of all classifiers in time domain, because the automatic separation is not an easy task.

Applying MPMFD provides the best results with the four classifiers. Accuracy of 100 % is reached with MDC, NB, k-NN (k= 1), and SVM. In this case, the separation of the early and late time is not necessary. Moreover, with this method we have reconstructed two parts of the signal: real and imaginary parts, thus making the poles more distinctive without the need to use a large frequency band.

The results indicate that features extracted with MPMFD present a plausible solution to automatic target classification especially for less resonant objects. With this method the separation between the early and late time is not required. A database containing object signatures can be built by using MPMFD. For resonant objects, applying MPMTD to extract CNRs is a good solution; the advantage of CNRs is their aspect independence.

5.5 Classification of complex objects in white Gaussian noise

In real applications, the target to classify may have a complex shape like: tree, animal, etc. Moreover, most of the time the backscattered signal is corrupted by noise which comes from environment and objects surrounding the target. In this section, we propose a powerful method for UWB ATC in white Gaussian noise and different aspect angles between the radar and the target [96]. The method is based

on the use of Matrix Pencil Method in Frequency Domain for feature extraction, and Mahalanobis Distance Classifier for classification.

By applying MPMFD, we extract singular values from the backscattered fields. Singular values are a projection of high dimensional UWB signal onto a low dimensional space, which allows the reduction of the database dimension. The MDC is a simple method for classification in comparison to other methods, hence it is convenient in real time applications.

We use MPMFD to classify complex objects in white Gaussian noise because of the advantages that we showed earlier. However, the features extracted by MPMFD have a random nature because they depend on the angle aspect. Thus, the statistical approach, which is described in this section, is the most appropriate for automatic target classification.

In order to test the accuracy of the proposed method, we have used complex target geometries modeled by perfectly conducting, straight, thin wires. The performance of the method is evaluated by adding Gaussian noise to the backscattered fields.

5.5.1 Classifier Design

Here, we show how we design the classifier based on the Mahalanobis distance. As features, we use the singular values which are extracted from the two components of the backscattered fields E_θ and E_φ. In the calculation of the Mahalanobis distance, the features which are distorted by noise, have in average, a higher influence on the distance measure than the less distorted features as they are further away from the feature mean of the class. Therefore, it is important to take only the less distorted features. By choosing M equal to six in the MPMFD, we have extracted six features from each field component. But for classification we use only the first two significant singular values of each field, so, the number of features N_f used in our work is equal to four.

Assume that we have N_o known objects of different form and N_a angles of backscattered fields from each object. In our simulation examples, we have taken N_o equal to four and N_a equal to eight. Let $x = (x_1, ..., x_{N_f})$ be an N_f-dimensional testing data which has no class label. Our goal is to build a classifier to predict its unknown class label $C = (C_1, ..., C_{N_o})$.

To construct the training data, we have used N_m equal to twenty random measures at 10 dB SNR level for each angle. Therefore, the classifier contains ($N_a \times N_o \times N_m$) = $(8 \times 4 \times 20) = 640$ training vectors: $y_k^{(i,j)}$ ($i = 1, ..., N_o$, $j = 1, ..., N_a$ and $k = 1, ..., N_m$). Each training vector contains 4 samples corresponding to the singular values.

Before calculating the Mahalanobis distance, we first need to determine for each angle of each corresponding object a mean vector of the N_m training vectors, let us say $m_{i,j}$:

$$m_{i,j} = \frac{1}{N_m} \sum_{k=1}^{N_m} y_k^{(i,j)} \tag{5.4}$$

Next, we calculate for each angle of each corresponding object a covariance matrix of the N_m measures, let us say $\Sigma_{i,j}$.

The Mahalanobis distance of the unknown testing data, x, from the known training data that are characterized by their $m_{i,j}$ and $\Sigma_{i,j}$ is:

$$D_{i,j} = \sqrt{(x - m_{i,j})^T (\Sigma_{i,j})^{-1} (x - m_{i,j})} \tag{5.5}$$

where $D_{i,j}$ is the distance of x from the ith object with the jth angle. $D_{i,j}$ will have small values when it is calculated by using training data of the same class like the testing data x.

Finally, we calculate for each object the mean of the Mahalanobis distance as

follows:

$$d_i = \frac{1}{N_a} \sum_{j=1}^{N_a} D_{i,j} \tag{5.6}$$

The decision is made by taking the ith C corresponding to the minimum value of d_i.

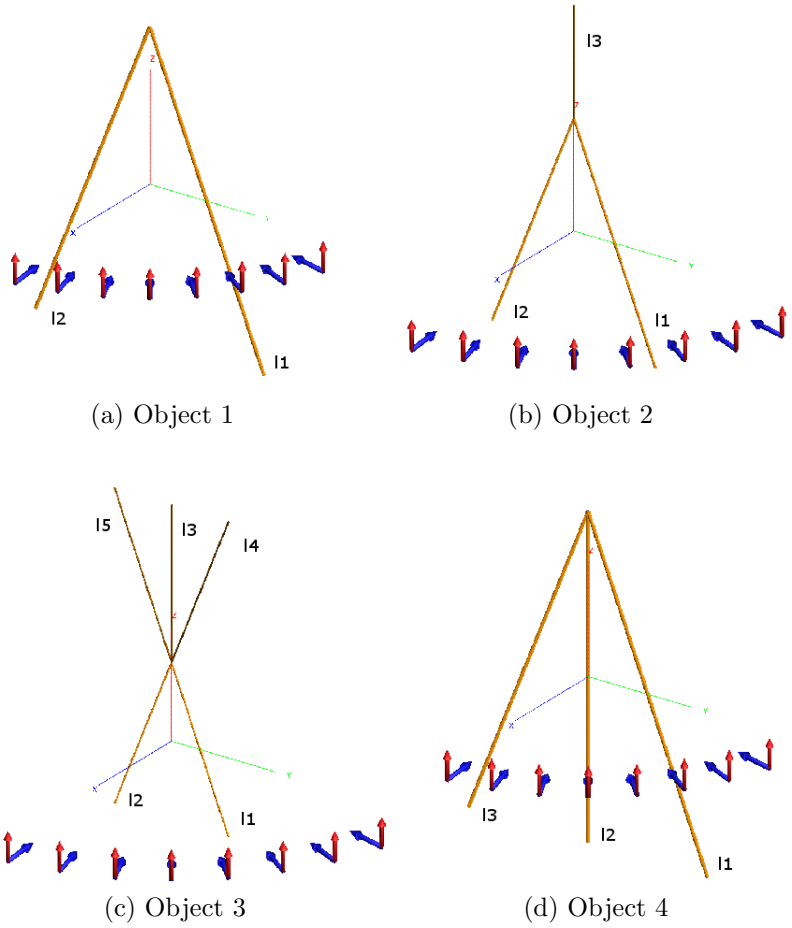

(a) Object 1 (b) Object 2

(c) Object 3 (d) Object 4

FIGURE 5.13: The 4 target geometries

5.5.2 Simulation results

In this subsection, numerical examples are given to illustrate the above automatic target classification method. To compute the free-space backscattered fields of the targets, a plane wave with normal incidence and vertical polarisation of the E-field is

Table 5.4: Dimensions of the four targets

Objects	**Wires (m)**	**Start Point (m)**			**End Point (m)**		
		x	**y**	**z**	**x**	**y**	**z**
1	**l1** = 0.53	0	0	0.25	0	0.2	-0.25
	l2 = 0.53	0	0	0.25	0	-0.2	-0.25
2	**l1** = 0.53	0	0	0.25	0	0.2	-0.25
	l2 = 0.53	0	0	0.25	0	-0.2	-0.25
	l3 = 0.25	0	0	0.25	0	0	0.5
3	**l1** = 0.53	0	0	0.25	0	0.2	-0.25
	l2 = 0.53	0	0	0.25	0	-0.2	-0.25
	l3 = 0.5	0	0	0.25	0	0	0.75
	l4 = 0.53	0	0	0.25	0	0.2	0.75
	l5 = 0.53	0	0	0.25	0	-0.2	0.75
4	**l1** = 0.53	0	0	0.25	0	0.2	-0.25
	l2 = 0.5	0	0	0.25	0	0	-0.25
	l3 = 0.53	0	0	0.25	0	-0.2	-0.25

used as excitation. The far-field backscattered responses are computed in frequency domain over the bandwidth from 3.5 to 4.9 GHz at 256 frequency sample points, from $N_o = 4$ complex target geometries modeled by perfectly conducting, straight, thin wires and for $N_a = 8$ monostatic aspect angles corresponding to: 5, 15, 25, 35, 45, 55, 65 and 75° (Figure 5.13).

The dimensions of the four targets are given in table 5.4. The object 1 is composed of 2 wires, the objects 2 and 4 are composed of 3 wires, and the object 3 is composed of 5 wires.The radius of the wires is 0.0025 m.

The backscattered fields E_θ and E_φ are given without considering the factor $\frac{e^{-jkR}}{R}$.

We assume that additive Gaussian noise is corrupting the real and imaginary components of the backscattered field independently. The SNR values are chosen

Table 5.5: Classification accuracy of each object (%)

SNR (dB)	**-10**	**-5**	**0**	**5**	**10**	**15**	**20**
Object 1	100	100	100	100	100	100	100
Object 2	99.68	100	99.68	99.68	99.37	96.87	99.37
Object 3	100	100	100	100	100	100	100
Object 4	2.5	63.12	89.37	99.84	100	100	100

to have the values of: -10, -5, 0, 5, 10, 15 and 20 dB. The addition of the random Gaussian noise to the ideal noise-free backscattered signals is repeated in 80 independent trials at each SNR level to obtain reliable results for noise analysis. A total of (4 targets) $\times$ (8 angles) $\times$ (7 SNR levels) $\times$ (80 trials) = 17920 noisy signals are generated to test the performance of the classifier.

Figure 5.14 shows an example of the simulated backscattered field E_θ (real and imaginary parts) from the object 1 with an aspect angle of 45° at 10 dB SNR, it is compared to the reconstructed one by MPMFD. The signal is filtered and well reconstructed by the MPMFD.

The figure 5.15 shows an example of the Mahalanobis distance D of a testing objet 1 with an aspect angle of 45° at 10 dB SNR level from the 4 objects of the training data as a function of the 8 aspect angles. The two components of the field are used for the calculation of the Mahalanobis distance. We can see that the minimum distance is from the object 1, and it is minumum for all the aspect angles. Therefore, after the calculation of the mean of the Mahalanobis distance for the eight angles, the testing object will be classified as object 1.

Using the two components of the backscattered fields E_θ and E_φ improves the classification accuracy. In figure 5.16 we can see the improvement of the total classification accuracy when using the two components E_θ and E_φ instead of one component E_θ.

Table 5.5, shows the classification accuracy of the four targets. The two compo-

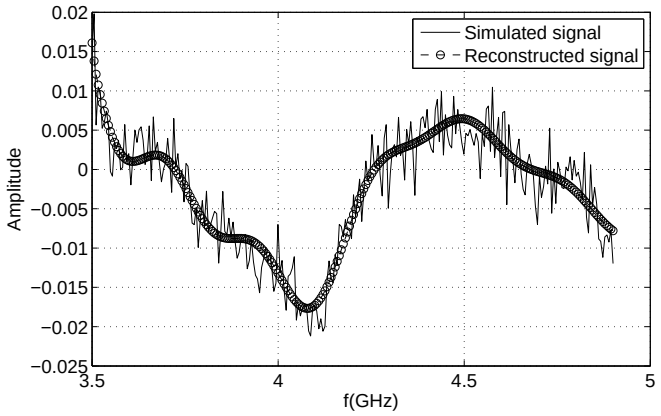

(a) The real part of the signal

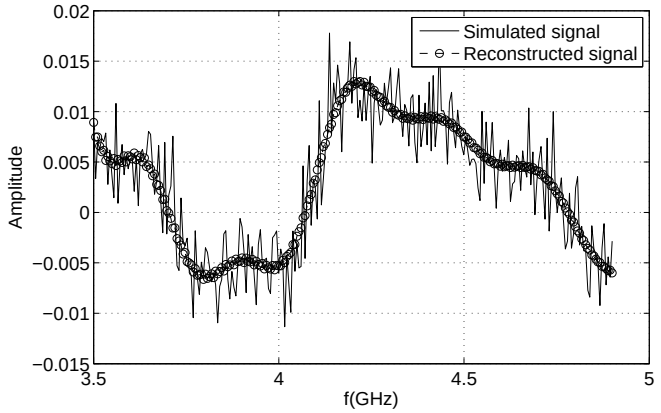

(b) The imaginary part of the signal

FIGURE 5.14: Simulated signal compared with reconstructed signal by MPMFD

nents of the field E_θ and E_φ are used for this classification. The accuracy rate of the classifier is observed to be 100 % for the object 1 and the object 3 at all the SNR levels used in our work.

The object 4 is classified with a high accuracy at 20, 15, 10, and 5 dB. Accuracy rate decreases to 89.37 % at 0 dB SNR, and drops to 2.5 % at the worst case of -10 dB. With high noise level, the object 4 can not be discriminated from the other objects.

The object 2 is well classified for all the SNR levels.

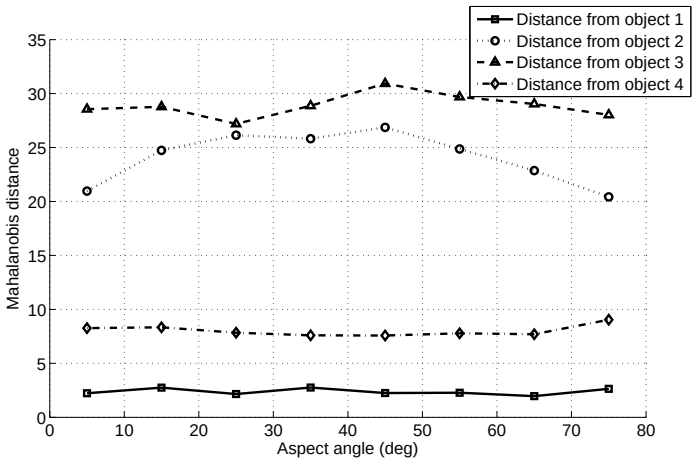

FIGURE 5.15: The Mahalanobis distance of the object 1 with an aspect angle of 45° from the 4 targets

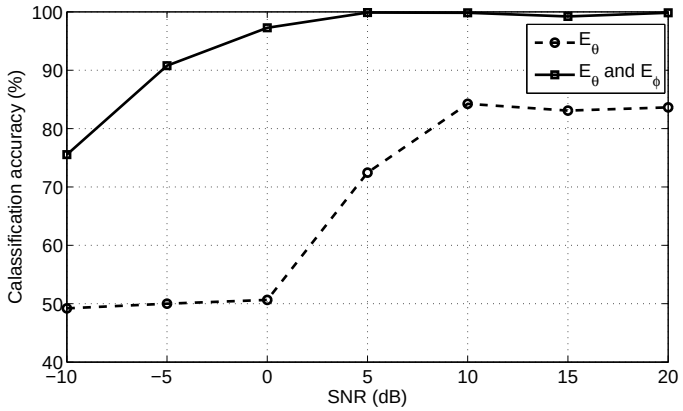

FIGURE 5.16: Comparison between the total classification accuracy when using only E_θ or both E_θ and E_φ

The results indicate that the classifier correctly identifies with very high accuracy the test targets of different aspect angles and with high noise level.

We conclude that the designed classifier which is based on the use of Matrix Pencil Method in Frequency Domain and Mahalanobis distance can be a good solution for automatic target classification.

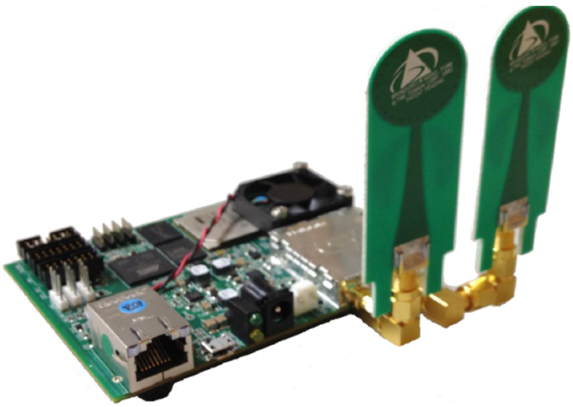

FIGURE 5.17: UWB P400 MRM

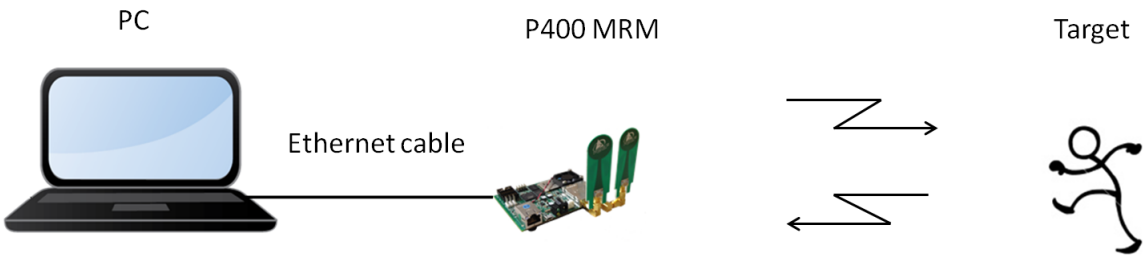

FIGURE 5.18: Radar system

5.6 Experimental results

5.6.1 Measurement setup

The measurements are taken using UWB P400 Monostatic Radar Module (MRM) manufactured by the Timedomain Co. Ltd (Figure 5.17). In the figure 5.18 we show the P400 MRM connected to a PC by using an Ethernet cable.

The P400 MRM has a bandwidth of more than 2 GHz. The RF transmission is from 3.1 GHz to 5.3 GHz, with center at approximately 4 GHz. It achieves an effective RF bandwidth of 1.4 GHz. It has a pulse repetition frequency of 10 MHz and a data step size in time of 61.024 ps. The figure 5.19 shows the transmitted waveform in

time and frequency domain. For our experiments we used omnidirectional antennas, but for real time application it is better to use directional antennas in front of the vehicle to detect and identify targets ahead of the vehicle.

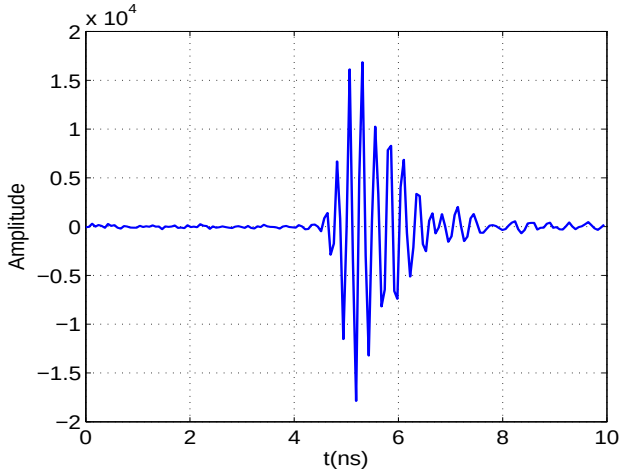

(a) Time domain

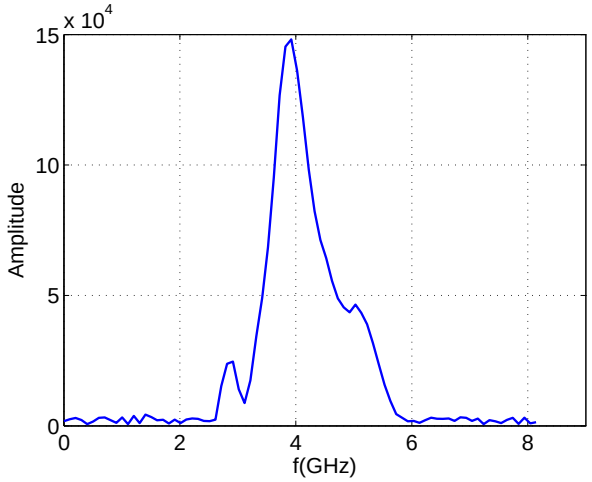

(b) Frequency domain

FIGURE 5.19: Transmitted waveform

The P400 MRM provides raw scans for post processing. It has a small size and a low power operation which allow it to be a good candidate for autonomous vehicles.

5.6.2 Data processing and feature extractions

To test the developed algorithms of automatic target classification, we use three targets: human, lamp and tree. We assume that the targets are stationary, have been detected and the backscattered fields contain only a single target. The targets are around 2 m far from the radar.



FIGURE 5.20: The indoor environment

The experiments are done in an indoor environment which is considered as a hostile environment because of the multipath coming from the walls and objects surrounding the target. Figure 5.20 shows the indoor environment with the lamp as target. Figure 5.21a shows the environment without target as a function of time and distance We can observe that returns from clutter within the first 1 m from the radar have high amplitude. This clutter is due to direct coupling and objects close to the radar.

Figure 5.21b shows the environment with target as a function of time and distance. To obtain the signature of the target only, we first eliminate the direct cou-

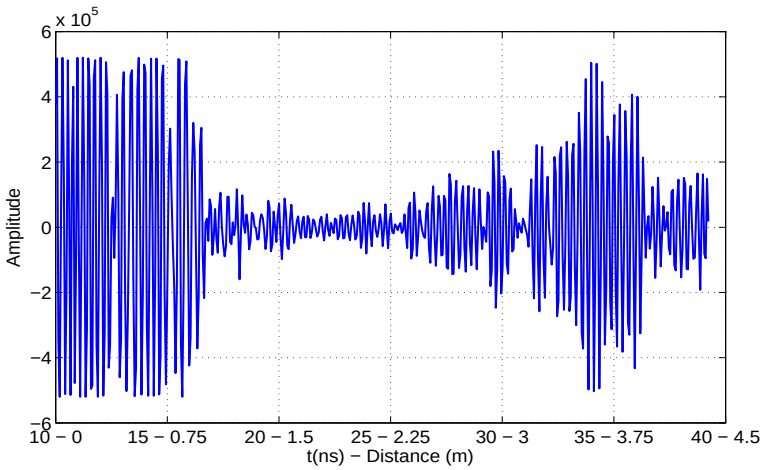

(a) Environment without target

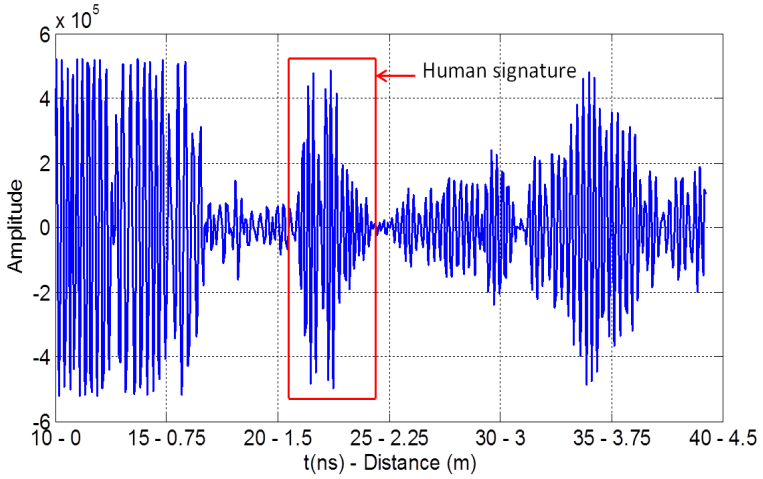

(b) Environment with target

FIGURE 5.21: Raw signal received by the radar

pling and returns from clutter. The clutter includes ground and objects surrounding the target that generate reflections. The measured data are subtracted from a data already stored when there is no target.

Figure 5.22 shows the three signatures of the three targets after removing the environment as function of time.

Once the environment is removed, a window of 4.27 ns is taken around the signatures of the targets. Next, we normalize the signatures in order to eliminate the

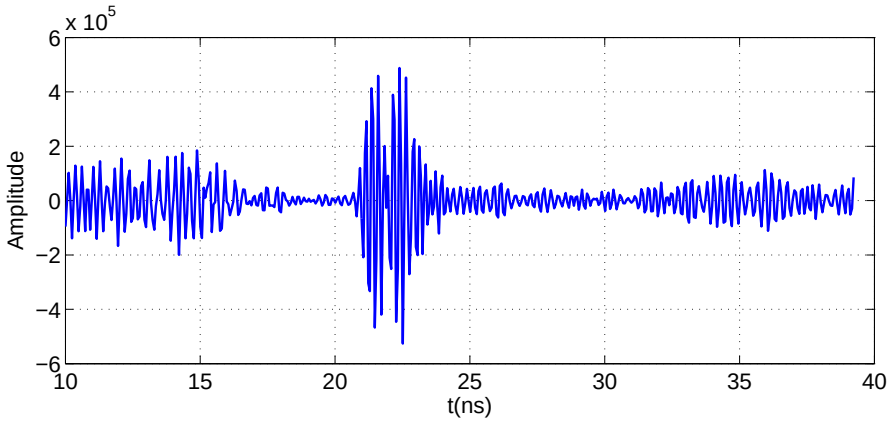

(a) Signature of the human

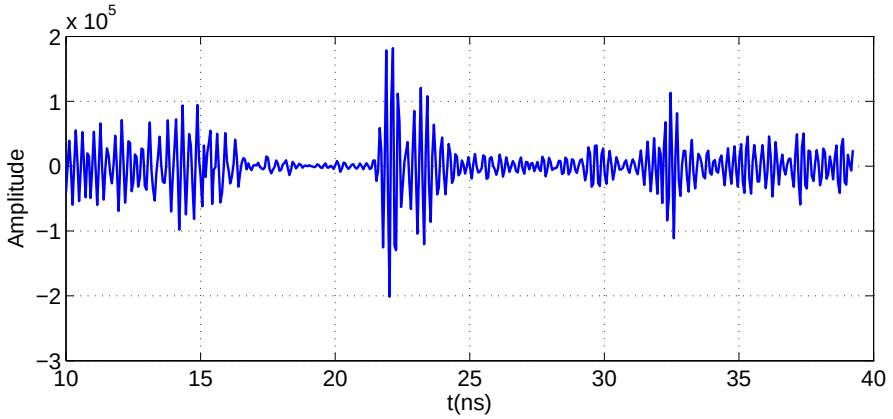

(b) Signature of the lamp

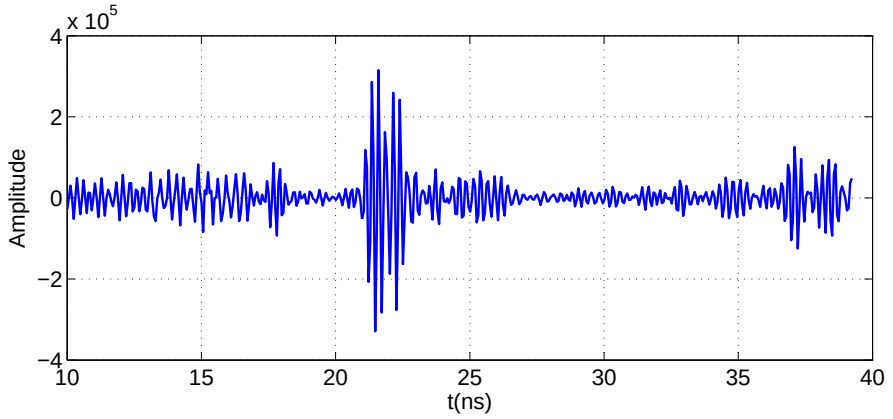

(c) Signature of the tree

FIGURE 5.22: Signatures of the three targets after removing the environment

effects of differing target amplitudes depending on the distance. The signatures are scaled so that all the peaks are equal to one (Figure 5.23).

Before applying MPMFD, we need to calculate the frequency response of the temporal signal. Therefore, after using zero-padding in order to increase the frequency resolution, we apply an FFT to the temporal signal to transform it to frequency domain. The resulted signal is divided by the FFT of the transmitted waveform.

Finally, we apply MPMFD on the frequency responses of the three targets over the bandwidth from 3.5 to 4.9 GHz. Figure 5.24 shows the measured and reconstructed real and imaginary parts of the backscattered signal. With $M = 6$ in MPMFD, the signals are well reconstructed.

5.6.3 Classification results

We use the singular values, which are extracted by MPMFD from the backscattered fields, as features in the entrance of the classifiers. We take measures for 8 monostatic aspect angles corresponding to: 5, 15, 25, 35, 45, 55, 65 and 75°. And from each angle we take 140 measures. Therefore, the data base contains 3 targets $\times$ 8 angles $\times$ 140 measures = 3360 feature vectors.

Figure 5.25 shows a plot of the first three singular values for the angle 0° calculated from 140 measures for each target. There are three distinct clouds of data points in the feature space: one for human, one for lamp and one for tree. The features of lamp and tree are condensed while the features of human are dispersed. However, the three targets can be discriminated. In figure 5.26, we show a plot of the first three singular values for the eight angles calculated from 140 measures for each angle of each target. We can distinguish eight different clouds for the tree corresponding to the eight angles. The features of lamp are condensed because the lamp is symmetrical. The features of human are dispersed because the human is not completely stationary like the two other targets. In addition the human target is

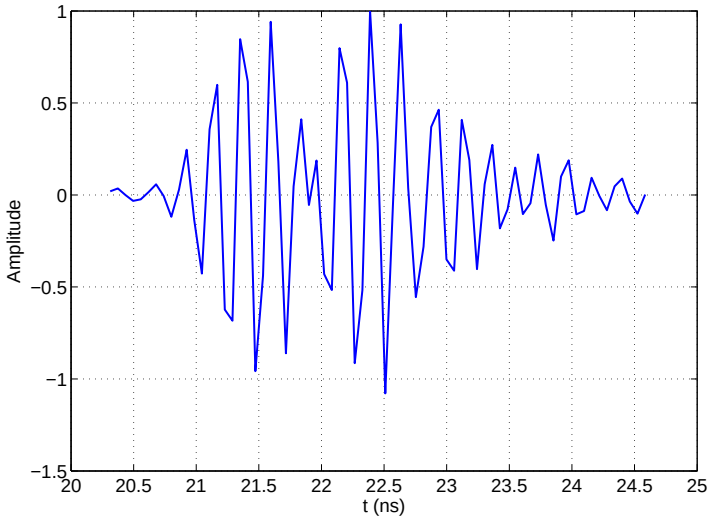

(a) Signature of the human

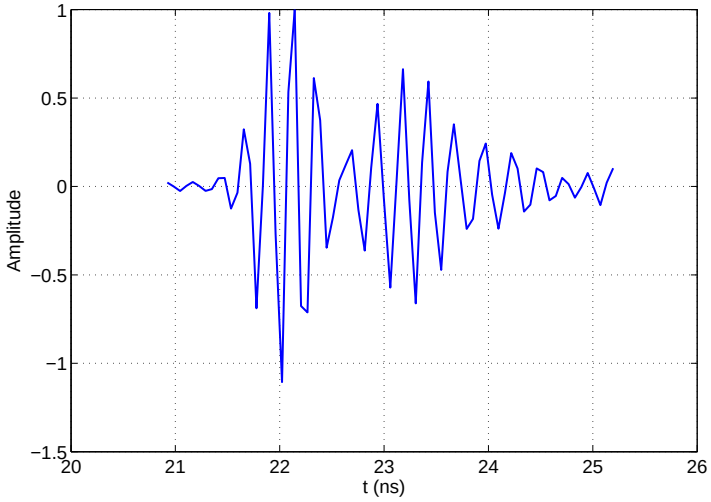

(b) Signature of the lamp

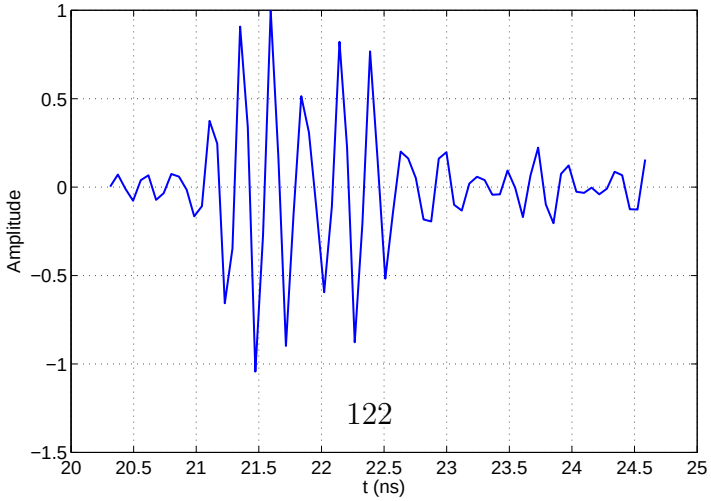

(c) Signature of the tree

FIGURE 5.23: Normalized signatures of the three targets

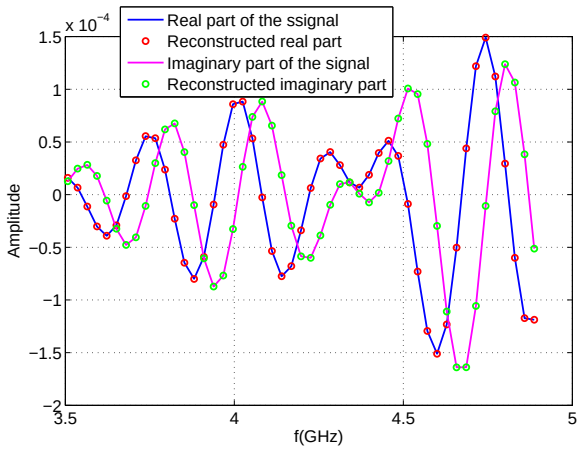

(a) Signature of the human

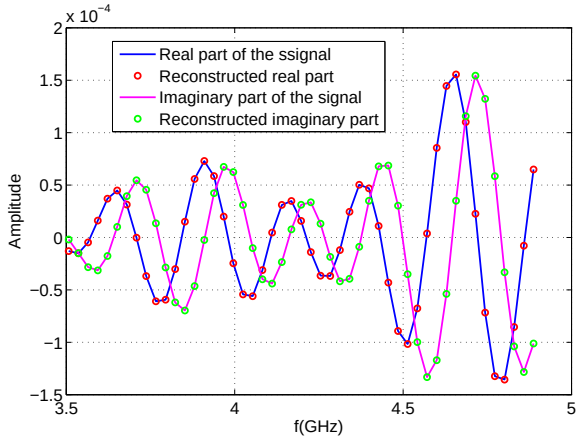

(b) Signature of the lamp

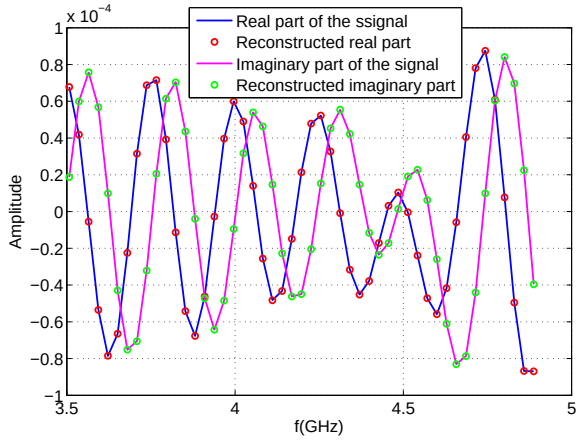

(c) Signature of the tree

FIGURE 5.24: Measured signal compared with reconstructed signal by MPMFD

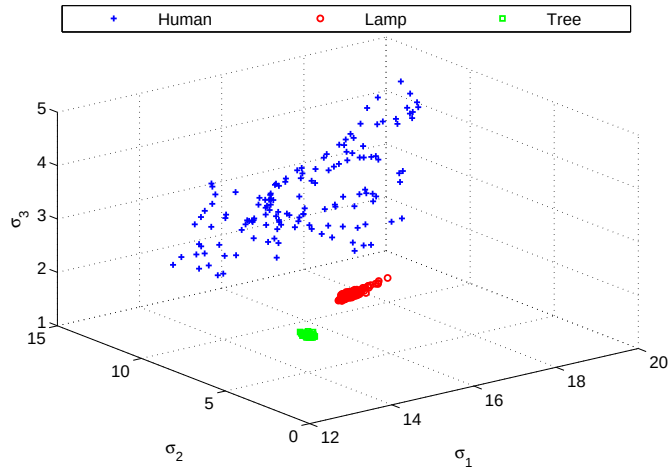

FIGURE 5.25: The first three singular values for one angle

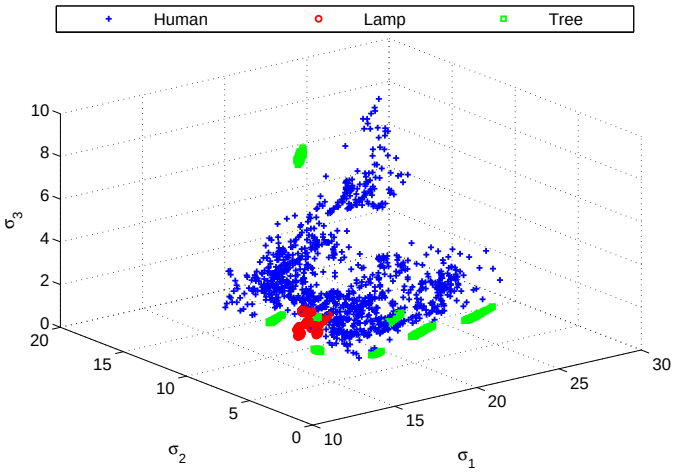

FIGURE 5.26: The first three singular values for all angles

made up of many scattering points that reflect the transmitted signal from different distances with different reflection coefficients as the pulse reaches the target.

To estimate the performance of classifiers a stratified 10-fold cross-validation approach is used. In 10-fold cross-validation the entire dataset is divided into 10 subsets (or folds) with approximately the same class distribution as the original dataset (stratified). Each fold is used once to test the performance of the classifier that is generated from the combined data of the remaining nine folds, leading to 10 independent performance estimates. The following classifiers are used: MDC, k-NN,

Table 5.6: Classification accuracy of each target (%)

Number of σ_i	**2**	**3**	**4**	**5**	**6**
MDC	98.45	99.97	99.88	99.97	99.97
NB	72.47	71.37	79.26	79.26	79.26
k-NN	98.48	99.94	99.94	99.94	99.94
SVM	98.6	100	100	100	100

NB and SVM.

Table 5.6, shows the classification accuracy of the three targets as function of the number of singular values. Except NB, all the other classifiers perform well even with 2 singular values. The best accuracy is reached starting from 3 singular values, it is 99.97 % for MDC, 99.94 % for k-NN ($k = 1$) and 100 % for SVM.

5.7 Conclusion

This chapter presented the software FEKO and the simulation parameters used in this work. The signals are obtained either in frequency domain or in time domain. Then, feature extraction results have been presented. We chose to use MPM as our main method for feature extraction because of its simplicity in comparison to other high resolution methods. In addition, it gave good results and it is less sensitive to noise. The advantage of using MPMFD than MPMTD has been presented also.

Next, comparison of different classification methods has been done. MPMFD gave the best results with all the classification methods that we used in this work. After that, a powerful method for UWB radar automatic target classification in white Gaussian noise and different aspect angles has been proposed. The method is based on the use of MPMFD for feature extraction, and Mahalanobis Distance for classification.

Finally, experimental results have been presented. We applied the developed algorithms of ATC on real targets. Good accuracy of classification has been found

by using: MDC, k-NN and SVM.

6

Conclusions

In this thesis, the possibility of automatically classifying an unknown target by using UWB radar was studied. The identification of the target is realized by making comparison between the deduced target properties and the different target features which are already recorded in a database. The two main steps in ATC are feature extraction and classification. The developed ATC technique has been demonstrated using simulated backscattered data from canonical objects. These shapes may be found as substructures on various vehicles. Also, ATC technique has been demonstrated using simulated backscattered data from complex target geometries modeled by perfectly conducting, straight, thin wires. Finally, it has been demonstrated using real targets: human, lamp and tree.

In chapter 2, our goal was to understand the physical behavior of electromagnetic waves when hitting the target (scattering). Based on this understanding, features must then be mathematically described depending on the given requirements. We found that different models have been proposed for scattering using either resonances or scattering centers. The advantage of CNRs is their aspect independence; hence we gave the analytical expressions of CNRs corresponding to the wire and the sphere.

In chapter 3, we presented the advantages of using UWB radar rather than conventional radars. Most of the advantages of UWB radars are associated with the bandwidth that is achieved. Basically, the wider bandwidth a system has the better it performs. Then we presented the different techniques used in UWB radar. We can use temporal or frequency techniques. Finally, we presented the different steps of ATC.

In chapter 4, we presented the methods that we used for feature extraction. In time domain we used wavelet transform to produce wavelet coefficients and high resolution methods to extract CNRs. In frequency domain, high resolution methods can be applied by using a reduced complexity model. Then we presented the different methods that we used for classification including: MDC, NB, k-NN and SVM. SVM is the most accurate, however with SVM it is difficult to understand the process of classifying. k-NN calculates the distance to all training vectors that are stored in the database, but MDC calculates the distance to only given classes which are represented by their mean and covariance matrix.

In chapter 5, we presented results obtained by simulations and experiments. Concerning high resolution methods; we found that MPM is suitable for the rest of our work for its simplicity and less sensitivity to noise in comparison to other methods. In time domain, we found that finding the beginning of the late time is not an easy task. In addition, there is a small contribution of the late time part of the signal, therefore, if the signal is noisy the late time part will be heavily corrupted by noise.

The simulation results obtained by using canonical targets showed the importance of feature extraction for targets classification. The results indicate that features extracted with MPMFD present a plausible solution to automatic target classification especially for less resonant objects. With this method the separation between the early and late time is not required. A database containing object signatures can be built by using MPMFD. For resonant objects, applying MPMTD to extract CNRs

is a good solution; the advantage of CNRs is their aspect independence.

Then, a robust method for automatic target classification was presented in this work. The accuracy of the proposed method is tested on four complex target geometries with different aspect angles and in high noise level. Results indicate that the designed classifier which is based on the use of MPMFD and MDC can be a good solution for automatic target classification.

Finally, experimental results have been presented. We applied the developed algorithms of ATC on real targets: human, lamp and tree. Good accuracy of classification has been found by using: MDC, k-NN and SVM. However, the features of human are dispersed in comparison to the features of the lamp and the tree.

In this research, the simulated targets have been treated in a free-space environment and all measurements and predictions have separated the target from other targets and media. In the future, taking into account the environment should be explored. Future work should also validate the developed ATC technique on new canonical objects (cube, strip, etc), complex objects (combination of canonical objects), and dielectric objects.

In this work, we used the vertical polarization in emission and we showed that the classification accuracy increases by using features extracted from the two components of the received signal. In the next stage, using the horizontal polarization in emission in addition to the vertical polarization should be explored.

In order to classify humans, extracting time-varying signatures for constructing input data features to a classification algorithm should be explored [97].

It is interesting to combine the developed method of ATC with algorithms of localization and communication and implement them on electronic devices like FPGA or DSP, so it can be used in autonomous vehicles.

Appendix A

Analytical expression of the sphere's residues

To obtain the analytical expression of the residues, we proceed as following:

First, we write:

$$F_n(\zeta) = \frac{(-1)^n(2n+1)}{\hat{H}_n^{(2)'}(\zeta)\hat{H}_n^{(2)}(\zeta)} = \frac{(-1)^n\zeta^{2n+1}e^{2\zeta}(2n+1)}{i^{2n+1}g_n(\zeta)f_n(\zeta)} = \frac{\zeta^{2n+1}e^{2\zeta}(2n+1)}{ig_n(\zeta)f_n(\zeta)} \tag{A.1}$$

$$iF_n(\zeta)\frac{e^{-2\zeta}}{\zeta} = \frac{\zeta^{2n}(2n+1)}{g_n(\zeta)f_n(\zeta)} = \sum_{k=1}^{n+1}\frac{r_{n,k}^g}{\zeta-\zeta_{n,k}^g} + \sum_{k=1}^{n}\frac{r_{n,k}^f}{\zeta-\zeta_{n,k}^f} \tag{A.2}$$

To find residues corresponding to the poles of $f_n(\zeta)$, we put:

$$f_n(\zeta_{n,k}^f) = 0 \quad \forall\ 1 \leq k \leq n \tag{A.3}$$

Thus:

$$r_{n,k}^f = \frac{(2n+1)(\zeta_{n,k}^f)^{2n}}{f_n'(\zeta_{n,k}^f)g_n(\zeta_{n,k}^f)} \tag{A.4}$$

To find residues corresponding to the poles of $g_n(\zeta)$, we put:

$$g_n(\zeta_{n,k}^g) = 0 \quad \forall\ 1 \leq k \leq n+1 \tag{A.5}$$

Thus:

$$r_{n,k}^{g} = \frac{(2n+1)(\zeta_{n,k}^{g})^{2n}}{f_n(\zeta_{n,k}^{g})g_n'(\zeta_{n,k}^{g})} \tag{A.6}$$

Next, we write:

$$f_n(\zeta) = \sum_{\beta=0}^{n} a_\beta \zeta^{n-\beta} \tag{A.7}$$

$$g_n(\zeta) = \sum_{\beta=0}^{n} a_\beta \zeta^{n-\beta}(\zeta+\beta) = \zeta f_n(\zeta) + \sum_{\beta=1}^{n} \beta a_\beta \zeta^{n-\beta} \tag{A.8}$$

where:

$$a_\beta = \frac{(n+\beta)!}{\beta!(n-\beta)!}\frac{1}{2\beta} \tag{A.9}$$

Therefore:

$$f_n^{'}(\zeta) = \sum_{\beta=0}^{n}(n-\beta)a_\beta\zeta^{n-\beta-1} = \sum_{\beta=0}^{n-1}(n-\beta)a_\beta\zeta^{n-\beta-1} = \frac{n}{\zeta}f_n - \sum_{\beta=1}^{n}\beta a_\beta\frac{\zeta^{n-\beta}}{\zeta} \tag{A.10}$$

$$\begin{aligned} g_n^{'}(\zeta) &= \sum_{\beta=0}^{n}(n-\beta)a_\beta(\zeta+\beta)\zeta^{n-\beta-1} + a_\beta\zeta^{n-\beta} \\ &= \sum_{\beta=0}^{n}(n-\beta)a_\beta(\zeta+\beta)\zeta^{n-\beta} + \sum_{\beta=0}^{n}\beta(n-\beta)a_\beta\zeta^{n-\beta-1} + \sum_{\beta=0}^{n}a_\beta\zeta^{n-\beta} \\ &= \sum_{\beta=0}^{n-1}(n-\beta)a_\beta\zeta^{n-\beta} + \sum_{\beta=1}^{n-1}\beta(n-\beta)a_\beta\zeta^{n-\beta-1} + \sum_{\beta=0}^{n}a_\beta\zeta^{n-\beta} \\ &= \zeta f_n^{'}(\zeta) + f_n(\zeta) + \sum_{\beta=1}^{n}\beta(n-\beta)a_\beta\zeta^{n-\beta-1} \end{aligned} \tag{A.11}$$

We put: $S_{n,1}(\zeta) = \sum_{\beta=1}^{n}\beta a_\beta\zeta^{-\beta}$ and $S_{n,2}(\zeta) = \sum_{\beta=1}^{n}\beta^2 a_\beta\zeta^{-\beta}$

From (A.3): $= \zeta_{n,k}^{f}$: $f_n = 0$, thus: $g_n = \sum_{\beta=1}^{n}\beta a_\beta\zeta^{n-\beta}$ and:

$$r_{n,k}^{f} = \frac{-(2n+1)\zeta_{n,k}^{f}}{\left(\sum_{\beta=1}^{n}\beta a_\beta(\zeta_{n,k}^{f})^{-\beta}\right)^2} = \frac{-(2n+1)\zeta_{n,k}^{f}}{\left(S_{n,1}(\zeta_{n,k}^{f})\right)^2} \tag{A.12}$$

From (A.3): $= \zeta_{n,k}^{g}$: $g_n = 0$, thus: $f_n = \frac{-1}{\zeta} \sum_{\beta=1}^{n} \beta a_\beta \zeta^{n-\beta}$ and:

$$
\begin{aligned}
g_n^{'} &= \zeta f_n^{'} + f_n + \frac{n}{\zeta} \sum_{\beta=1}^{n} \beta a_\beta \zeta^{n-\beta} - \frac{1}{\zeta} \sum_{\beta=1}^{n} \beta^2 a_\beta \zeta^{n-\beta} \\
&= n f_n - \sum_{\beta=1}^{n} \beta a_\beta \zeta^{n-\beta} + f_n + \frac{n}{\zeta} \sum_{\beta=1}^{n} \beta a_\beta \zeta^{n-\beta} - \frac{1}{\zeta} \sum_{\beta=1}^{n} \beta^2 a_\beta \zeta^{n-\beta} \\
&= (n+1) f_n + (\frac{n-\zeta}{\zeta}) \sum_{\beta=1}^{n} \beta a_\beta \zeta^{n-\beta} - \frac{1}{\zeta} \sum_{\beta=1}^{n} \beta^2 a_\beta \zeta^{n-\beta} \\
&= (n+1) f_n - (n-\zeta) f_n - \frac{1}{\zeta} \sum_{\beta=1}^{n} \beta^2 a_\beta \zeta^{n-\beta} \\
&= (1+\zeta) f_n - \frac{1}{\zeta} \sum_{\beta=1}^{n} \beta^2 a_\beta \zeta^{n-\beta}
\end{aligned}
\tag{A.13}
$$

Then:

$$
\begin{aligned}
r_{n,k}^{g} &= \frac{(2n+1)(\zeta_{n,k}^{g})^2}{\left[\sum_{\beta=1}^{n} \beta a_\beta (\zeta_{n,k}^{g})^{-\beta}\right] \left[(1+\zeta) \sum_{\beta=1}^{n} \beta a_\beta (\zeta_{n,k}^{g})^{-\beta} + \sum_{\beta=1}^{n} \beta^2 a_\beta (\zeta_{n,k}^{g})^{-\beta}\right]} \\
&= \frac{(2n+1)(\zeta_{n,k}^{g})^2}{S_{n,1}(\zeta_{n,k}^{g}) \left[(1+\zeta) S_{n,1}(\zeta_{n,k}^{g}) + S_{n,2}(\zeta_{n,k}^{g})\right]}
\end{aligned}
\tag{A.14}
$$

Bibliography

[1] N. de Beaucoudrey J. Chauveau and J. Saillard. Characterization of perfectly conducting targets in resonance domain with their quality of resonance. *Progress In Electromagnetics Research*, 74:69–84, 2007.

[2] E. J. Rothwell and K. M. Chen. A hybrid e-pulse/least squares technique for natural resonance extraction. *Proceedings of the IEEE*, 76:296–298, 1988.

[3] R. Kumaresan and D. W. Tufts. Estimating the parameters of exponentially damped sinusoids and pole-zero modeling in noise. *IEEE Transactions on Acoustics, Speech, and Signal Processing*, 30:833–840, 1982.

[4] T. K. Sarkar and O. Pereira. Using the matrix pencil method to estimate the parameters of a sum of complex exponentials. *IEEE Ant. and Prop. Mag*, 37:4855, 1995.

[5] N. V. Z. Shuley. A review of uncooperative target identification using uwb resonance based radar techniques. *ECTI Transactions on Electrical Engineering, Electronics, and Communications*, 4:118–126, 2006.

[6] G. Turhan-Sayan. Real time electromagnetic target classification using a novel feature extraction technique with pca-based fusion. *IEEE Transactions onAntennas and Propagation*, 53:766–776, 2005.

[7] H. Moon W. Lee, T. K. Sarkar and M. Salazar-Palma. Computation of the natural poles of an object in the frequency domain using the cauchy method. *IEEE Antennas andWireless Propagation Letters*, 11:1137–1140, 2012.

[8] J.A. Stratton. *Electromagnetic Theory*. Mc Graw-Hill, London, 1941.

[9] Odile Picon et coll. *Les antennes : Théorie, conception et applications*. Dunod, Paris, 2009.

[10] C. E. Baum. The singularity expansion method. *Transient Electromagnetic Field*, pages 129–179, 1976.

[11] J. B. Keller. Geometrical theory of diffraction. *J. Opt. Soc. Amer*, page 116130, Jan. 1962.

[12] M. Skolnik. *Radar Handbook*. 3rd Edition,The McGraw-Hill Companies, 2008.

[13] C-C Chen. Electromagnetic resonances of immersed dielectric spheres. *IEEE Transaction on Antennas and Propagation*, 46:1047–1083, July 1998.

[14] R. Carriere L. C. Potter, D. M. Chiang and M. J. Gerry. A gtd-based parametric model for radar scattering. *IEEE Trans. Antennas Propagat*, 43:10581067, Oct. 1995.

[15] R. C. Qiu M. McClure and L. Carin. On the superresolution of observables from swept-frequency scattering data. *IEEE Trans. Antenna Propagat*, 45:631–641, 1997.

[16] M. P. Hurst and R. Mittra. Scattering center analysis via prony's method. *IEEE Trans. Antenna Propagat*, 35:986–988, 1987.

[17] G. MIE. Beiträge zur optik trüber medien, speziell kolloidaler metallsungen, annalen der physik. *Vierte Folge, Band 25 (3)*, pages 377–445, 1908.

[18] C.A Balanis. *Advanced Engineering Electromagnetics*, chapter 11, page 650. John Wiley and sons, 1989.

[19] K. M. Chen and D. Westmoreland. Impulse response of a conducting sphere based on singularity expansion method. *Proceedings of the IEEE*, 69:747–750, 1981.

[20] M. Abramowitz and I. Stegun. *Handbook of Mathematical Functions*. NBS Applied Mathematics Series, 1968.

[21] F. M. Tesche and D. V. Giri. On the natural oscillation frequencies of a straight wire. *Interaction Notes, Note 621*, 2011.

[22] M.V. Ianoz F.M. Tesche and T. Karlsson. *EMC Analysis Methods And Computational Models*. John Wiley and Sons, Inc, 1997.

[23] S.W. Lee and B. Leung. The natural resonance frequency of a thin cylinder and its application to emp studies. *Interaction Notes, Note 96*, 1972.

[24] L. A. Weinstein. *The Theory of Diffraction and the Factorization Method*. The Golem Press, Boulder CO, 1969.

[25] A. Hoorfar and D. C. Chang. Analytic determination of the transient response of a thin-wire antenna based upon an sem representation. *IEEE Trans. AP*, 30, 1982.

[26] C. J. Bouwkamp. Hallén's theory for a straight, perfectly conducting wire, used as a transmitting or receiving aerial. *Physica IX*, 7:609–631, 1942.

[27] R. F. Harrington. *Field Computation by Moment Methods.* The Macmillan Co., New York, 1968.

[28] F. M. Tesche. On the analysis of scattering and antenna problems using the singularity expansion technique. *IEEE Transactions on AP*, 21:5362, 1973.

[29] C. E. Baum. *On the Use of Contour Integration for Finding Poles, Zeros, Saddles and other Function Values in the Singularity Expansion Method.* Mathematics Notes, Note 35, Air Force Weapons Laboratory, 1974.

[30] D. V. Giri B. K. Singaraju and C. E. Baum. *Further Developments in the Application of Contour Integration to the Evaluation of the Zeros of Analytic Functions and Relevant Computer Programs.* Mathematics Notes, Note 42, Air Force Weapons Laboratory, 1976.

[31] S. S. Sandler J. M. Myers and T. T. Wu. Electromagnetic resonances in a straight wire. *IEEE Transactions on AP*, 59:53–62, 2011.

[32] T. W. Barrett. History of ultra-wideband radar and communications: pioneers and innovators. *Progress in Electromagnetics Symposium 2000*, pages 1–29, 2000.

[33] H. F. Harmuth. *Transmission of Information by Orthogonal Functions.* 1st Edition, New York: Springer, 1969.

[34] H. F. Harmuth. Range-doppler resolution of electromagnetic walsh waves in radar. *IEEE Transaction on Electromagnetic Compatibility*, 17:106–111, 1975.

[35] H. F. Harmuth. Synthetic aperture radar based on non sinusoidal functions pulse compression, contrast, resolution, and doppler shift. *IEEE Transaction on Electromagnetic Compatibility*, 21:40–49, 1979.

[36] H. F. Harmuth. *Non sinusoidal Waves for Radar and Radio Communication.* New York: Academic, 1981.

[37] H. F. Harmuth. *Antennas and Waveguides for Non sinusoidal Waves.* New York: Academic, 1984.

[38] G. F. Ross and K. W. Robbins. *Baseband Radiation and Reception System.* U.S. Patent 3,739,392, June 1973.

[39] G. F. Ross. *Transmission and Reception System for Generating and Receiving Baseband Duration Pulse Signals for Short Baseband Pulse Communication System.* U.S. Patent 3,728,632, July 1973.

[40] G. F. Ross and K. W. Robbins. *Narrow Range-Gate Baseband Receiver.* U.S. Patent 4,695,752, September 1987.

[41] P. V. Etten. The present technology of impulse radars. *Proceedings of the International Radar Conferences*, pages 353–539, October 1977.

[42] R. N. Morey. *Geophysical Survey System Employing Electromagnetic Impulses*. US Patent 3,806,795, April 1974.

[43] D. L. Moffat and R. J. Puskar. A subsurface electromagnetic pulse radar. *Geophysics*, 41:506–518, 1976.

[44] S. W. Millikan Way. *Instruction Manual: Type S-2 Sampling Head*. ektronix, Inc., P.O. Box 500, Beaverton, Oregon 97005, 1968.

[45] C. E. Cook and M. Bernfeld. *Radar Signals: An Introduction to Theory and Application*. New York: Academic Press, 1967.

[46] C.L. Bennett and G.F. Ross. Time-domain electromagnetics and its application. *Proceedings of the IEEE*, 66:299–318, 1978.

[47] T.W. Barrett. *Impulse (Time-Domain) Radar Technology Assessment Colloquium*. W.J. Schafer Associates, Arlington, VA, 16th-17th March, 1988.

[48] B. Noel. *Ultra-Wideband Radar: Proceedings of the First Los Alamos Symposium*. CRC Press, Boca Raton, FL, 1991.

[49] I.J. Lahaie. Ultra wideband radar. *SPIE Proceedings Series*, 1631, 1992.

[50] L. Carin H.L. Bertoni and L.B. Felsen. *Ultra-Wideband Short-Pulse Electromagnetics*. Plenum Press, 1993.

[51] L. Carin and L.B. Felsen. *Ultra-Wideband Short-Pulse Electromagnetics 2*. New York: Plenum Press, 1995.

[52] L. Carin C.E. Baum and A.P. Stone. *Ultra-Wideband, Short-Pulse Electromagnetics 3*. New York: Plenum Press, 1997.

[53] E. Heyman and B. Mandelbaum. *Ultra-Wideband Short-Pulse Electromagnetics 4*. New York: Plenum Press, 1999.

[54] H.F. Harmuth. *Radiation of Nonsinusoidal Electromagnetic Waves*. Academic, New York, 1990.

[55] J.D. Taylor. *Introduction to Ultra-Wideband Radar Systems*. CRC Press, Boca Raton, FL, 1995.

[56] L.Yu. Astanin and A.A. Kostylev. *Ultra-Wideband Radar Measurements: Analysis and Processing*. Radar. Sonar, Navigation and Avionics Series, IEE, London, UK, 1997.

[57] T.E. McEwan. *Ultra-wideband radar motion sensor.* US Patent 5,361,070, November, 1994.

[58] D. Wong L. Nguyen, K. Kappra and J. Sichina. Mine detection performance in different soil conditions using data from an ultra wideband wide area surveillance radar. *Proceedings of SPIE The International Society for Optical Engineering*, pages 930–941, 1999.

[59] K. Scheff P. Hansen and E. Mokole. *Dual polarized, UWB radar measurements of the sea at 9 GHz, in Ultra-Wideband, Short-Pulse Electromagnetics 4.* Kluwer/Plenum,New York, 1999.

[60] Eric L. Mokole and P. Hansen. *Survey of Ultra-wideband Radar in Ultra-Wideband, Short-Pulse Electromagnetics 7.* Springer-Verlag, 2007.

[61] Sinan Gezici Zafer Sahinoglu and Ismail Guvenc. *Ultra-wideband Positioning Systems: Theoretical limits.* Ranging Algorithms, and Protocols Cambridge University Press, 2008.

[62] J. D. Taylor. *Ultra-Wideband Radar Technology*, chapter 13, page 343378. CRC Press, 2001.

[63] I. Chernyi S. Lukjanov, R. Stepanov and O. Stukach. Use of the ground penetrating radar methods for paleontology on example of the mammoth fauna investigation. *Proceedings of the 37th European Microwave Conference*, page 17471750, 2007.

[64] C. Nguyen J. S. Lee and T. Scullion. A novel, compact, low-cost, impulse ground-penetrating radar for nondestructive evalulation of pavements. *IEEE Transactions on Instrumentation and Measurement*, 53:15021509, 2004.

[65] V. Utsi. Design of a gpr for deep investivations. *4th International Workshop on Advanced Ground Penetrating Radar*, page 222225, 2007.

[66] O. Brandt K. Langley, R. Storvold and J. Kohler. Use of c-band ground penetrating radar to determine backscatter sourceswithin glaciers. *IEEE Transactions on Geoscience and Remote Sensing*, 45:12361246, 2007.

[67] W. Kofman. Radar techniques to study subsurfaces and interiors of the solar system objects. *19th International Conference on Microwave Radar and Wireless Communications*, page 409 412, 2012.

[68] Fa. Wenzhe. Modeling and simulation for ground penetrating radar study of the subsurface structure of the moon. *14th International Conference on Ground Penetrating Radar*, page 922 926, 2012.

[69] Jing Liang and Qilian Liang. Sense-through-foliage target detection using uwb radar sensor networks. *Pattern Recognition Letters*, 31:1412–1421, 2010.

[70] Wolfgang Menzel Markus Andres, Peter Feil. 3d-scattering center detection of automotive targets using 77 ghz uwb radar sensors. *Antennas and Propagation (EUCAP), 6th European Conference*, pages 3690–3693, 2012.

[71] I. Balasingham R. Chavez-Santiago and J. Bergsland. Ultrawideband technology in medicine: A survey. *Journal of Electrical and Computer Engineering*, 2012:9, 2012.

[72] M. Glavin R. C. Conceiao, M. O'Halloran and E. Jones. Support vector machines for the classification of early-stage breast cancer based on radar target signatures. *Progress In Electromagnetics Research B*, 23:311–327, 2010.

[73] Ernest E. Okon Ben Allen, Mischa Dohler, Wasim Q. Malik, Anthony K. Brown, and David J. Edwards. *ULTRA-WIDEBAND ANTENNAS AND PROPAGATION FOR COMMUNICATIONS, RADAR AND IMAGING*, chapter 1, page 13. John Wiley and sons, Ltd, 2007.

[74] Md. Asdaque Hussain Sana Ullah, Murad Ali and Kyung Sup Kwak. Applications of uwb technology. *The 5th annual International New Exploratory Technologies Conference*, pages 225–232, 2008.

[75] C. Loyeza M. Heddebauta, F. Elbahhara and coll. Millimeter-wave communicating-radars for enhanced vehicle-to-vehicle communications. *Transportation Research Part C: Emerging Technologies*, 18:440–456, 2009.

[76] K. Ohno H. Takahara and M. Itami. A study on uwb radar assisted by inter-vehicle communication for safety applications. *IEEE International Conference on Vehicular Electronics and Safety*, pages 99–104, 2009.

[77] S.E. Hamran. *Radar Technology*, chapter 1, page 118. In-Teh, 2009.

[78] J. D. Taylor. *Ultra-Wideband Radar Technology*, chapter 3, page 8183. CRC Press, 2001.

[79] D.P. Nyquist E.J. Rothwell, K.M. Chen and J.E. Ross. A radar target discrimination scheme using the discrete wavelet transform for reduced data storage. *IEEE Antennas and Propagation*, 42:1033–1037, 1994.

[80] C.A.D. Gualdron V.V. Garcia and G.O. Plata. Obtaining patterns for classification of power quality disturbances using biorthogonal wavelets, rms value and support vector machines. *International Conference on Electrical Power Quality and Utilisation*, pages 1–6, 2007.

[81] P. S. Addison. *The Illustrated Wavelet Transform Handbook*. Naiper University, Edinburgh, U.K: Institute of Physics, 2002.

[82] G. M. Riche de Prony. Essai expérimental et analytique: sur les lois de la dilatabilité de fluides élastiques et sur celles de la force expansive de la vapeur de l'eau et de la vapeur de l'alcool différentes températures. *Journal de l'école polytechnique*, 22:2476, 1795.

[83] R. O. Schmidt. *A signal subspace approach to multiple emitter location and spectral estimation*. PhD thesis, Stanford University, 1981.

[84] A. Paulraj R. Roy and T. Kailath. Esprita subspace rotation approach to estimation of parameters of cisoids in noise. *IEEE Trans. Acoust., Speech, Signal Processing*, 34:13401342, 1986.

[85] Y. HUA and T. K. SARKAR. On the total least squares linear prediction method for frequency estimation. *IEEE Transactions on Acoustics, Speech and Signal Processing*, 38(12):2186–2189, 1990.

[86] Y. HUA and T. K. SARKAR. On svd for estimating generalized eigenvalues of singular matrix pencil in noise. *IEEE Transactions on Signal Processing*, 39(4):892–900, 1991.

[87] V. Kumar X. Wu and coll. Top 10 algorithms in data mining. *Knowledge and Information Systems*, 14:137, 2007.

[88] R. Kohavi. A study of cross-validation and bootstrap for accuracy estimation and model selection. *The Fourteenth International Joint Conference on Artificial Intelligence (IJCAI)San Francisco, CA: Morgan Kaufman*, pages 1137–1145, 1995.

[89] D. Jouan-Rimbaud R. De Maesschalck and D. L. Massart. The mahalanobis distance. *Chemometrics and Intelligent Laboratory Systems*, 50:1–18, 2000.

[90] I. Guyon B. Boser and V. Vapnik. A training algorithm for optimal margin classifiers. *Fifth Annual Workshop on Computational Learning Theory*, pages 144–152, 1992.

[91] V. Kecman. *Learning and Soft Computing*. MIT Press, Cambridge, 2001.

[92] L. Hamel. *Knowledge Discovery with Support Vector Machines*, chapter 11, page 185189. JohnWiley and Sons, Inc, 2009.

[93] *FEKO Comprehensive Electromagnetic Solutions: User's Manual*. 2010.

[94] Z. Ding J. E. Mooney and L. S. Riggs. Robust target identification in whitegaussian noise for ultra wide-band radar systems. *IEEE Transactions on Antennas and Propagation*, 46:18171823, 1998.

[95] M. Khodjet-Kesba K. El Khamlichi Drissi, S. Lee and coll. Comparison of matrix pencil extracted features in time domain and in frequency domain for radar target classification. *International Journal of Antennas and Propagation*, 2014, Article ID 930581, 9 pages, 2014.

[96] M. Khodjet-Kesba K. El Khamlichi Drissi, S. Lee and coll. Robust uwb radar target classification in white gaussian noise based on matrix pencil method in frequency domain and mahalanobis distance. *International radar conference*, 2014, Lille, France.

[97] N. Lee J.D. Bryan, J. Kwon and Y. Kim. Application of ultra-wide band radar for classification of human activities. *IET Radar, Sonar and Navigation*, 6:172–179, 2011.